Drop impact splashing and air entrapment

Dissertation by

Marie-Jean Thoraval

In Partial Fulfillment of the Requirements

For the Degree of

Doctor of Philosophy

High-Speed Fluids Imaging Laboratory

Mechanical Engineering Program

Physical Science and Engineering Division

King Abdullah University of Science and Technology

Thuwal, Makkah Province, Kingdom of Saudi Arabia

Defence date: 17th March 2013

The dissertation of **Marie-Jean Thoraval** is approved by the examination committee:

Ravi Samtaney		
Committee Chair	Signature	Date
Suk Ho Chung		
Committee Member	Signature	Date
Aslan Kasimov		
Committee Member	Signature	Date
David Quéré		
External Committee Member	Signature	Date
Sigurdur T. Thoroddsen		
Dissertation Supervisor	Signature	Date

King Abdullah University of Science and Technology

2013

Abstract

Drop impact splashing and air entrapment

Marie-Jean Thoraval

Drop impact is a canonical problem in fluid mechanics, with numerous applications in industrial as well as natural phenomena. The extremely simple initial configuration of the experiment can produce a very large variety of fast and complex dynamics. Scientific progress was made in parallel with major improvements in imaging and computational technologies. Most recently, high-speed imaging video cameras have opened the exploration of new phenomena occurring at the micro-second scale, and parallel computing allowed realistic direct numerical simulations of drop impacts. We combine these tools to bring a new understanding of two fundamental aspects of drop impacts: splashing and air entrapment.

The early dynamics of a drop impacting on a liquid pool at high velocity produces an ejecta sheet, emerging horizontally in the neck between the drop and the pool. We show how the interaction of this thin liquid sheet with the air, the drop or the pool, can produce micro-droplets and bubble rings. Then we detail how the breakup of the air film stretched between the drop and the pool for lower impact velocities can produce a myriad of micro-bubbles.

Keywords: drop impact; splashing; ejecta sheet; slingshot mechanism; bubble ring; air toroid; liquid toroid; Gerris; VOF; vortex street; vortex shedding; air entrapment; Mesler entrainment

Acknowledgements

First of all, I would like to thank my advisor Siggi Thoroddsen for his guidance and continuous support. I also thank the other committee members of this dissertation: Ravi Samtaney, Aslan Kasimov, Suk Ho Chung and David Quéré. The wonderful classes taught by David Quéré and Christophe Clanet at Ecole Polytechnique (Palaiseau, France) have played a key role in introducing me to my advisor and to the wonders of drop splashing.

This thesis could not have reached the same quality without our collaborators on high speed imaging and numerical simulations. Takeharu Goji Etoh and Kohsei Takehara have shared with us their latest developed cameras, and their experience during two visits in Kinki University (Osaka, Japan). I have also benefited from the three months spent in Institut Jean le Rond d'Alembert (Paris, France), learning about numerical simulations of drop impacts, under the guidance of Stéphane Zaleski and Christophe Josserand. I am also grateful to Stéphane Popinet for sharing the Gerris code he developed, and his dedicated support. The mailing list was very helpful to continue using the code from KAUST.

I am thankful to the other members of the High-Speed Fluids Imaging Laboratory: Ivan Vakarelski, Jeremy Marston, Erqiang Li and Jiaming Zhang. They have always been very helpful and a source of inspiration driving my research in this exciting environment of a starting university in Saudi Arabia.

Many people in KAUST have also contributed to this work. This include the Research Computing team, especially Benoit Marchand, Alain Clo, Rashid Abrar and Mohammed Naseemuddin. I would like to thank Helmut Pottmann for advice

on curvature calculations, Suk Ho Chung and Tamer El Sayed for allowing me to use their computational resources.

I have also benefited from the help of Fenghua Zhang in some preliminary experiments in Kinki University. I have learnt also from useful discussions with Andrea Prosperetti, Gilou Agbaglah, and members of the laboratories where I stayed.

On a more personal level, I would like to express my gratitude to my wife 刘丝丽 and my family for their support and encouragements to pursue my passion.

Table of Contents

List of Figures

List of Tables

Chapter 1

Introduction

1.1 Background

Drop impact is a very simple experimental geometry. However, the complexity of its outcomes has fascinated researchers for more than a century. As we will see in this dissertation, even the simplest experiment of a water drop impacting on a pool of water can still reveal new and unexpected dynamics. The parameter space to study is immense, and offers a simple framework to study new phenomena in fluid dynamics.

Depending on the impact velocity, and the properties of the liquid used, the drop can spread, float, coalesce, bounce, or splash (Rein, 1993). They can also make noise (Prosperetti and Oguz, 1993), entrap bubbles (Liow and Cole, 2007), and create vortex rings (Thomson and Newall, 1885, Peck and Sigurdson, 1994) that can carry micro-bubbles into the fluid (Carroll and Mesler, 1981, Esmailizadeh and Mesler, 1986).

In addition to the fundamental interest of studying these phenomena, they also have important applications in very diverse domains. In most applications we are interested in whether the impact will splash droplets or entrap bubbles, both producing a large range of sizes and involving different mechanisms. Recent reviews include those of Yarin (2006) and Thoroddsen et al. (2008). This complexity makes it a very challenging problem to model and reproduce numerically,

see Chapter A and Tryggvason et al. (2011).

Drop impacts have important industrial applications in combustion, where fuel droplets splashing on the walls are beneficial to the production of smaller droplets, thus enhancing the combustion efficiency (Moreira et al., 2010). In inkjet printing however, splashing needs to be avoided to improve the precision. Printing technologies have also developed to print electronic circuits, solar cells, or biological materials (Martin et al., 2008, Jung and Hutchings, 2012, Chatzikomis et al., 2012). Air entrapment is also detrimental in this case, as in spray coatings, using molten metal (Aziz and Chandra, 2000) or liquid paints. Spray coatings are for example used in the pharmaceutical industry (Bolleddula et al., 2010), and for granulation (Marston et al., 2010). Sprays are also used to cool hot surfaces in nuclear reactors (Sawan and Carbon, 1975), electronics industry (Kim, 2007), and aeronautics (Michalak et al., 2010).

On a larger scale, rain is important for marine science, as it influences the gas transfer into the oceans (Wanninkhof et al., 2009). The smallest splashed droplets can evaporate, leaving microscopic aerosols that can act as nucleation sites during cloud formation, affecting climate. When the rain droplets impact on the ground, they participate in soil erosion. The splashed droplets can also participate in the seeds or pore dispersal, and spreading of diseases and pesticides (Fitt et al., 1989). They are also important in criminal forensic to study blood splash patterns Hulse-Smith et al. (2005), Knock and Davison (2007).

Interestingly, droplet splashing happening over a few hundred microseconds can affect the growth of stalagmites in caves over thousands of years. Understanding their formation is therefore useful in palaeoclimatology.

The interaction of the impacting drop with a granular material has important application to produce liquid marbles (Emady et al., 2011, Marston et al., 2012b). Similar splashing dynamics are also observed with granular flows (Thoroddsen and Shen, 2001, Marston et al., 2012a), and constitute a meteor impact model used in

earth and planetary science.

The correct reproduction of splashing dynamics is a challenge also in geometric modelling and animation movies (Losasso et al., 2004, Eden et al., 2007, Thornton, 2006, Garg et al., 2007, Wojtan et al., 2010, Wojtan, 2010, Thürey et al., 2010, Yu et al., 2012). Their capture has attracted several artists who specialize their work in drop splashing. Splashing is one of the most common images in the beverage advertising.

1.2 Literature review

The scientific study of splashing began with the work of Worthington (1876, 1877, 1882, 1895) who first used strobed visual observations and sketches, before he incorporated the use of the nascent technology of photography and published the seminal book *A study of splashes* (Worthington, 1908). Many studies have followed in the subsequent century, incorporating the latest imaging technology of each time period. Some of the most relevant studies will now be reviewed, focusing on a single drop impact event.

Most earlier studies focused on the overall edge breakup of the corona, after it rises out of the pool, forming what is often called the Edgerton crown Edgerton and Killian (1939), Kayafas et al. (1987). Numerous studies are dedicated to determining the splashing threshold, especially for impacts onto solid surfaces. Particularly noteworthy studies are those of Stow and Hadfield (1981), Mundo et al. (1995), Cossali et al. (1997), which proposed the importance of the *splashing parameter* $K = We\sqrt{Re}$, where these non-dimensional numbers are defined by the impact velocity of the drop U, the drop diameter D,

$$Re = \frac{UD}{\nu}, \qquad We = \frac{\rho D U^2}{\sigma}$$

where ν is the liquid kinematic viscosity, ρ is the liquid density and σ is the surface

tension.

Rioboo et al. (2001) have further characterized the different splashing scenarios and proposed the terminology of *corona splash* where the crown breaks up on its edge into droplets, vs. the *prompt splash* which arises at the very early contact of the drop with the solid substrate.

Most instructive imaging of the early contact have been carried out for impacts onto glass surfaces, where the dynamics can be observed through the substrate (Thoroddsen and Sakakibara, 1998).

An important discovery was recently made by Xu et al. (2005) where they showed that onset of splashing can be delayed by reducing the air pressure. It has not been determined what causes this, but recent studies suggest that it is related to the cushioning under the drop by the air layer (Thoroddsen and Sakakibara, 1998, Thoroddsen et al., 2003, Smith et al., 2003, Mehdi-Nejad et al., 2003, Van Dam and Le Clerc, 2004, Thoroddsen et al., 2005, Mani et al., 2010, Hicks and Purvis, 2010, 2011, 2012, Driscoll and Nagel, 2011, Duchemin and Josserand, 2011, 2012, Palacios et al., 2012, de Ruiter et al., 2012, Mandre and Brenner, 2012, Kolinski et al., 2012, van der Veen et al., 2012, Liu et al., 2013). This introduces a new non-dimensional parameter, i.e. the density ratio of the air to that of the liquid.

Another fundamental discovery was made in the last decade: the *ejecta sheet* (Weiss and Yarin, 1999, Thoroddsen, 2002, Josserand and Zaleski, 2003). Figure 1.1 shows a striking manifestation of this phenomenon. This fine jet emerges from the neck that connects the drop to the pool for high impact velocities. The phenomenon escaped notice until recent advances in high-speed imaging (Thoroddsen et al., 2008). The ejecta sheet is the most significant factor for the splashing of micro-droplets. Interestingly, their first observation in numerical simulations of Weiss and Yarin (1999) already suggested that it should produce "a torus shaped liquid volume" and "a torus-shaped bubble" as described in their

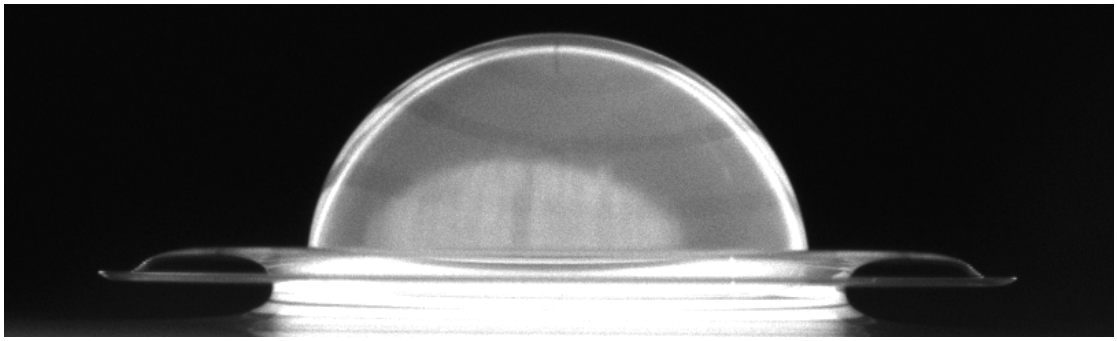

Figure 1.1: Ejecta sheet during drop impact onto a pool.

abstract:

> "For times that are small compared to the characteristic time of impact [...], it is found that a disk-like jet forms at the neck between the drop and the pre-existing liquid film, if the impact Weber number is high enough. This jet can pinch off a torus-shaped liquid volume at its tip or reconnect with the pre-existing liquid film, thus entraining a torus-shaped bubble."

Similar observations were reported by Davidson (2002):

> "Instead of growing progressively, the jet in Fig. 5 waxes and wanes with the jet sometimes disappearing completely."

However, these studies did not include viscous effects in their boundary integral calculations, and could not capture the topology changes that would have led to this kind of splashing and bubble entrapment. Moreover, their simulations are irrotational, and no vorticity could enter the liquid.

Experimentally, new details keep emerging with improvements in high-speed video technology. Most recently stunning images have been presented by Zhang et al. (2012), where they have used X-rays to see through the ejecta to reveal inner air cavities and ejecta sheets travelling up the drop surface.

Bubble rings and bubbles located around the central bubble entrapment were previously observed experimentally for a drop impacting on a solid surface (Chan-

dra and Avedisian, 1991, Thoroddsen et al., 2005, Ootsuka et al., 2005, Dhiman and Chandra, 2008, Dhiman, 2009, Dhiman and Chandra, 2010, Thoroddsen et al., 2010, Palacios et al., 2012) or a liquid pool (Thoroddsen et al., 2003, Liow and Cole, 2007). In numerical simulations, is also appeared naturally in axisymmetric simulations of Mehdi-Nejad et al. (2003) for a solid surface, and Oguz and Prosperetti (1989), Weiss and Yarin (1999), Davidson (2002), Josserand et al. (2010) for a liquid pool.

However, the early experimental techniques did not have sufficient time resolution to allow verification of the formation of a torus-shaped bubble before breaking into bubble rings. Furthermore, there is still no clear experimental evidence that the mechanism described by Oguz and Prosperetti (1989) can pinch-off toroidal bubble, called Oguz-Prosperetti bubble rings. They suggested that their mechanism could explain the bubble entrapments observed by Blanchard and Woodcock (1957), Carroll and Mesler (1981), Esmailizadeh and Mesler (1986), instead of the Rayleigh-Taylor instability suggested by Sigler and Mesler (1990).

1.3 Thesis outline

The atomization of liquid volumes often involves the creation of liquid sheets, which subsequently break up into filaments and droplets (Villermaux and Clanet, 2002). Similar breakup dynamics can be observed in the bubble entrapment process (Carroll and Mesler, 1981, Lezzi and Prosperetti, 1991, Dorbolo et al., 2005). Herein, we will focus on the dynamics and breakup of the ejecta sheet for high impact velocities, and the air sheet stretched between the drop and the pool at lower impact velocities.

Different instabilities have been described in the literature that could explain the early splashing, such as the Richtmyer-Meshkov instability (Gueyffier and Zaleski, 1998, Krechetnikov and Homsy, 2009), the Rayleigh-Plateau capillary insta-

bility (Zhang et al., 2010), combinations of them (Krechetnikov, 2010, Agbaglah et al., 2013), or waves in the sheet (Dombrowski and Fraser, 1954, Taylor, 1959a,b, Dombrowski and Johns, 1963, Villermaux and Clanet, 2002). The possible origins of droplets is discussed in Tryggvason et al. (2011).

Herein, we combine the latest high-speed imaging capabilities, with the state-of-the-art numerical methods for multiphase flows, using the large computational resources available, to identify new mechanisms leading to splashing and air entrapment.

In Chapter 2 we study experimentally the dynamics of the ejecta sheet, and identify a new mechanism of splashing produced when the ejecta sheet breaks on contact with the pool.

In Chapter 3, we focus our study on the dynamics of the base of the ejecta sheet, with extremely high mesh refinement in numerical simulations, demonstrating that its early interaction with the drop and the pool can splash micro-droplets and entrap bubble rings.

Chapter 4 confirms experimentally the predictions made by the numerical simulations in the previous chapter, such as bubble rings entrapments and vorticity shedding, and also shows the complexity of the three-dimensional instabilities that follow.

Finally, we show experimentally in Chapter 5 how myriads of micro-bubbles are produced by the break-up of the extremely thin air film stretched between the drop and the pool at the lowest impact velocities.

Each chapter is based on a separate paper, specified in the abstract.

Chapter 2

Droplet splashing by a slingshot mechanism

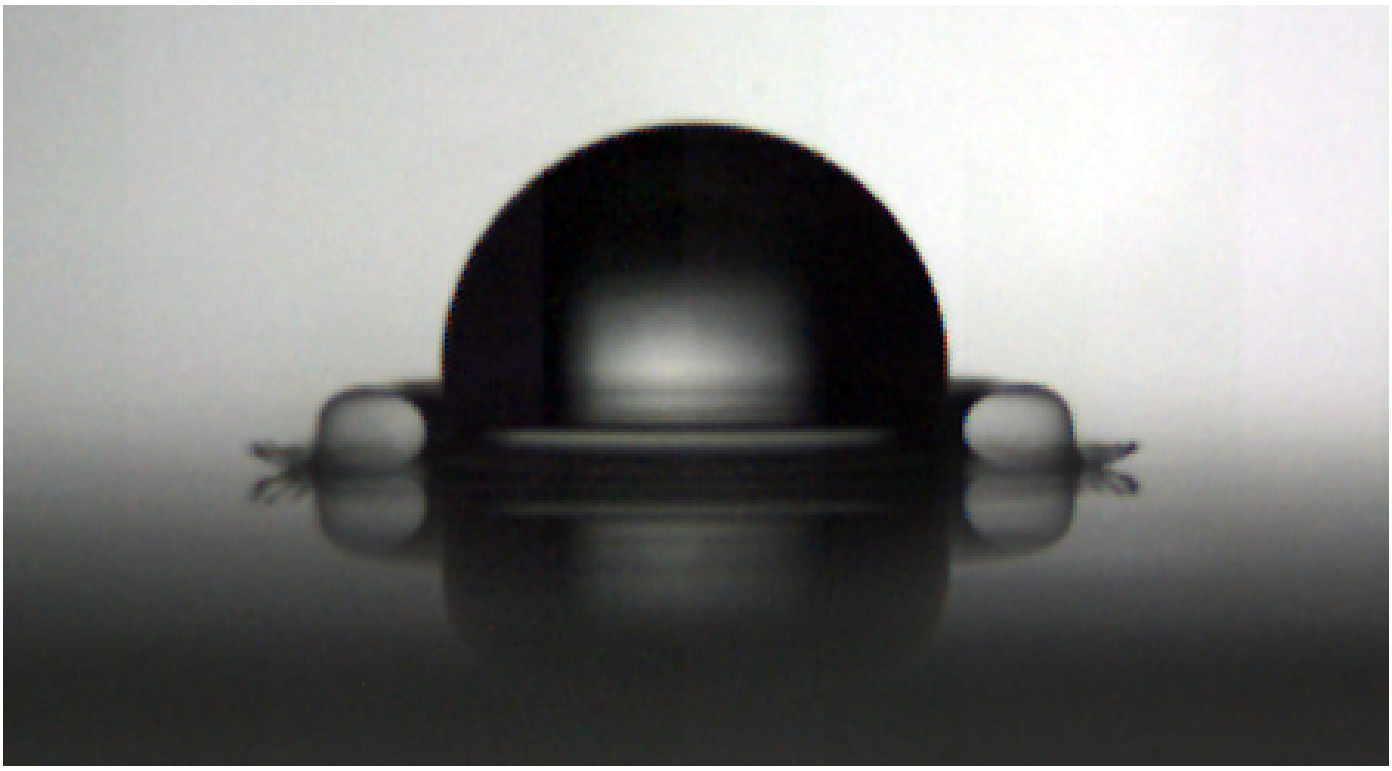

Figure 2.1: Emergence and bending of the ejecta sheet for a viscous liquid drop impacting on a deep pool of the same liquid at a velocity U = 4.5 m/s (μ =20 cP, Re = 1330 and We = 1830). See supplemental video.

Abstract

When a drop impacts onto a liquid pool, it ejects a thin horizontal sheet of liquid, which emerges from the neck region connecting the two liquid masses. The leading section of this ejecta bends down to meet the pool liquid. When the sheet touches the pool, at an 'elbow', it ruptures and sends off micro-droplets by a slingshot mechanism, driven by surface tension. High-speed imaging of the splashing droplets, suggests the liquid sheet is of sub-micron thickness, as thin as 300 nm. Experiments in partial vacuum show that air resistance plays the primary role in bending the sheet. We identify a parameter regime where this slingshot occurs and also present a simple model for the sheet evolution, capable of reproducing the overall shape.

This chapter is based on Thoroddsen et al. (2011).

2.1 Introduction

The splashing of a drop impacting onto a liquid layer is of great importance in a number of industrial applications, like combustion, spray painting, cleaning and cooling, as well as natural processes such as air-entrainment, aerosol formation through atomization and erosion by rain (Yarin, 2006). Recent improvements in high-speed video imaging have started to allow characterization of the finer details of these processes (Thoroddsen et al., 2008). This has revealed numerous intricate new fluid phenomena, not previously observed or understood. One of these is the emergence of a fine jet of fluid following the initial contact of the impacting drop with the pool liquid (Weiss and Yarin, 1999, Thoroddsen, 2002, Josserand and Zaleski, 2003, Howison et al., 2005). Despite their small size these fine structures can have dramatic effects on the overall flow and the formation of spray through the breakup of the liquid edge.

2.2 Experimental setup

We use gravity-driven water/glycerin drops, from 0 to 90% glycerin, giving a viscosity range up to μ =109 cP. The drops are released from a range of nozzle diameters, generating drops with diameters D from 3.2 to 6.0 mm. The liquid pool is always deeper than $2D$, so that the bottom of the pool does not affect the early dynamics studied herein. The impact velocity U when the drop hits the pool is varied by changing the release heights up to 4.3 m. The Reynolds, Weber and Ohnesorge numbers of the impact are defined as

$$Re = \frac{\rho D U}{\mu}; \quad We = \frac{\rho D U^2}{\sigma}; \quad Oh = \frac{\mu}{\sqrt{\rho\,\sigma\,D}} = \frac{\sqrt{We}}{Re}$$

where μ and ρ are the dynamic viscosity and density of the liquid and σ is the surface tension. Gravity plays no role on these very short time-scales (< 2 ms).

The Re and We are often rearranged to form the splashing parameter (Stow and Hadfield, 1981, Mundo et al., 1995), encompassing inertia, surface tension and viscous effects,

$$K = We\sqrt{Re} = \sqrt{\frac{\rho^3 D^3 U^5}{\sigma^2 \mu}}.$$

This parameter arises naturally, from the following mechanistic considerations, by forming a local We_ℓ based on the relevant local length scale being the ejecta sheet thickness $\delta \sim \sqrt{\nu t} \sim \sqrt{\nu D/U}$ and using the ejecta velocity which scales as $u_j \sim U\sqrt{Re}$ based on Thoroddsen (2002) and Josserand and Zaleski (2003). By substitution this produces $We_\ell = \rho\delta u_j^2/\sigma = K$.

To capture the details of the rapid ejecta motions, we pursue a two-pronged approach, using both an ultra-high-speed video camera for sufficient temporal resolution and a dual-frame PIV camera in combination with Nd-Yag pulsed laser-sheet, for higher spatial resolution (Thoroddsen, 2002). The video camera (Etoh et al., 2003) is capable of 1,000,000 fps, while each clip has 102 frames of 260 × 312 pixels. The time-counter in the online video is in μs.

2.3 Experimental results

Figure 2.2 shows details of the ejecta sheet and the slingshot mechanism, which splashes secondary micro-droplets. The sheet emerges from the neck region between the drop and the pool, following the first contact. Then the sheet bends characteristically downwards and touches the pool (panel 4) at an *elbow* where the sheet ruptures (5). The thicker leading tip of the sheet provides a counter-balance to slingshoot the ruptured end through pulling by the surface tension, by momentum conservation. This mechanism shoots microdroplets horizontally at high speed (7-10).

In Fig. 2.3 we show the region of the parameter space where the ejecta sheets are formed and categorize their evolution. When the ejecta sheet does not break

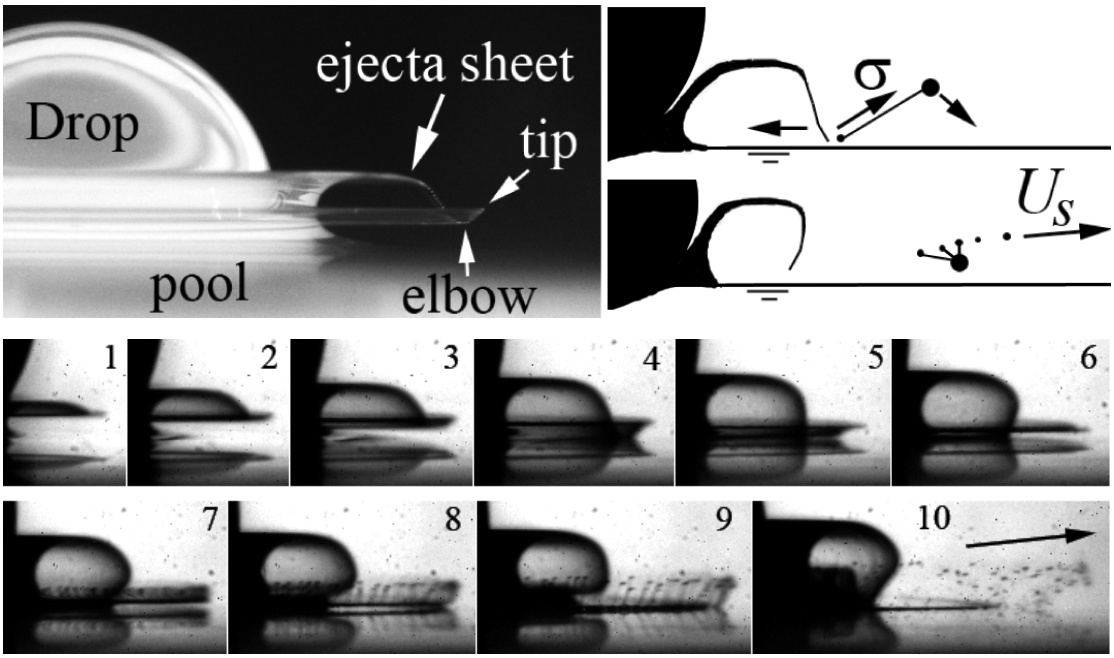

Figure 2.2: (Top) Typical ejecta sheet and sketch showing the slingshot mechanism. (Bottom sequence) Ejecta sheet emerges, bends downwards, ruptures as it touches the pool and then sling-shoots droplets horizontally. Frames are 50, 70, 80, 90, 100, 110, 120, 130, 140 & 170 μs after impact. See supplemental video.

in fine droplets at ejection (at low Oh), its evolution is clearly determined by the K parameter. For $K < 2 \times 10^4$ the sheet does not bend toward the pool. For K between 2×10^4 and 5.5×10^4 it bends but does not reach the pool surface, whereas for $K > 5.5 \times 10^4$ it touches the pool surface. In this case, for $Oh < 2 \times 10^{-2}$ the tip of the sheet breaks before reaching the pool (▲), while for larger Oh (▽), the slingshot mechanism is observed, see Fig. 2.2. Deegan et al. (2008) have similarly shown that K-scaling works for the crown breakup.

In the slingshot regime, the ejecta bends down sooner for higher values of K and hits the pool closer to the impact center. When the sheet elbow touches the pool surface, we measure the height of the trapped toroidal tent of air, H in the inset of Fig. 2.4 and in Fig. 2.7. This height scales very well with K over a range of 3 different fluid viscosities and 2 drop diameters.

Figure 2.5 shows the characteristic velocity of the droplets U_s which are slingshot horizontally. Their speed increases linearly with larger K when Oh is kept

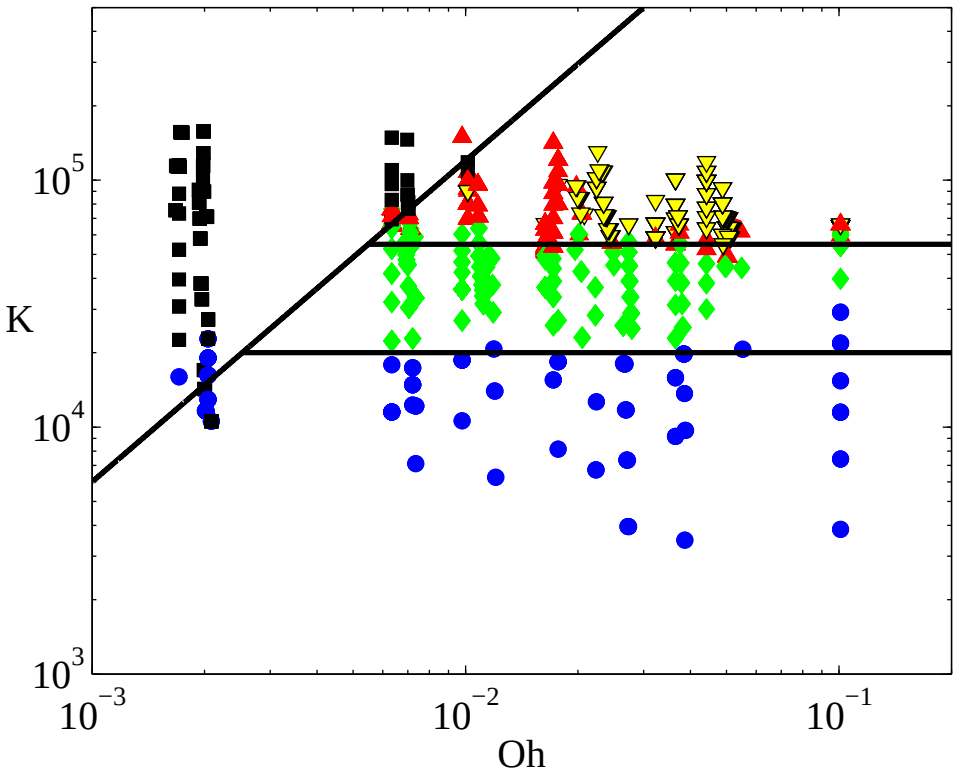

Figure 2.3: Characterization of the ejecta sheet dynamics:
(■) Irregular broken sheets and spray.
(●) Ejecta sheets do not bend towards pool.
(♦) Sheets bend downwards, but do not reach the pool.
For both triangles, the sheet bends downward and reaches the pool:
(▲) Sheet breaks before impacting the pool and no slingshot.
(▽) Slingshot of fine droplets.

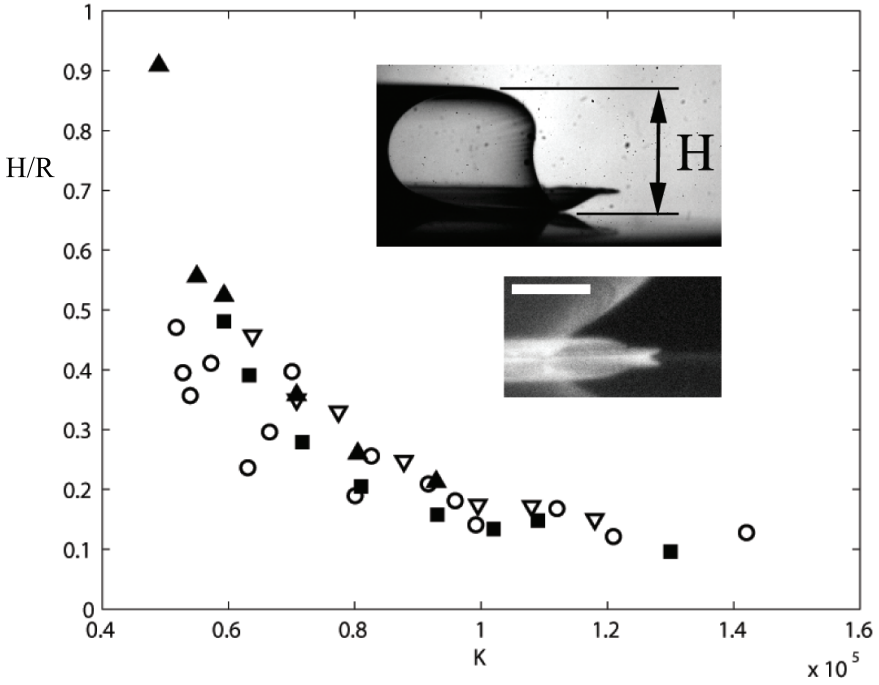

Figure 2.4: Height of the ejecta sheet H when the elbow touches the pool, normalized by the drop radius R, vs K.

(○) Oh = 0.017, μ = 10 cP, D = 4.4 mm
(■) Oh = 0.023, μ = 14 cP, D = 4.4 mm
(▽) Oh = 0.044, μ = 30 cP, D = 5.7 mm
(▲) Oh = 0.049, μ = 30 cP, D = 4.4 mm

Lower inset: The ejecta sheet for large value of K, where it touches the pool ~ 50 μs after impact, when the drop has penetrated only 7% of R into the pool. Bar is 0.5 mm.

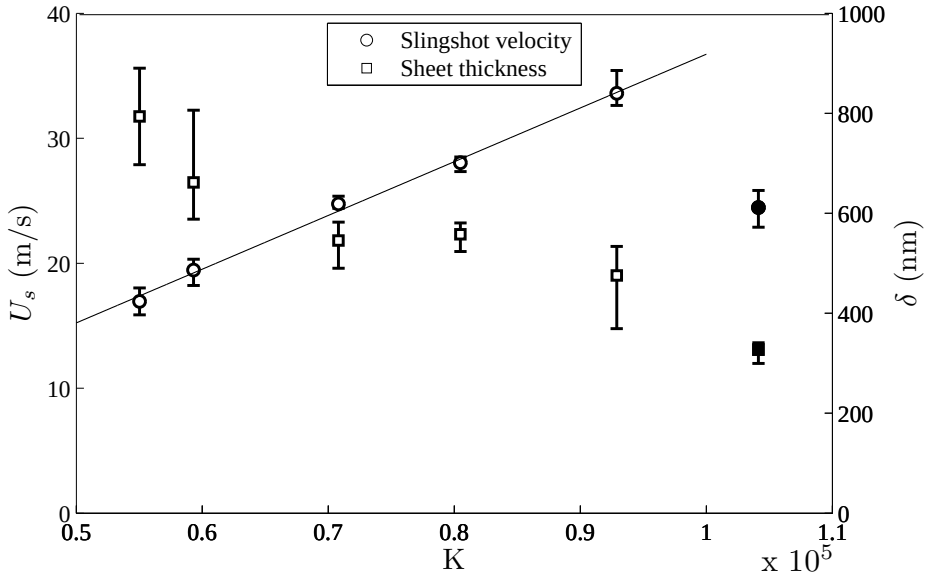

Figure 2.5: Slingshot velocity U_s of droplets and the corresponding film thickness δ based on the relative Taylor-Culick law. For μ = 75 cP and Oh = 0.049 (open symbols). Filled symbols show results for the largest impact velocity U = 7.8 m/s and μ =109 cP (Oh = 0.18). Each data point is an average of 3 experimental measurements (2 for the first point on the left). The extremal values are represented by the error bars.

constant (Oh = 0.049, moving vertically in Fig. 2.3). The well-known Taylor-Culick law gives the translational velocity of a free liquid edge as $U_{TC} = \sqrt{2\sigma/(\rho\delta)}$, where δ is the thickness of the liquid sheet. However, the Taylor-Culick law refers to the velocity of the edge relative to the internal velocity in the sheet. While we expect the sheet to start from rest as it ruptures, the slingshot further accelerates the edge as it approaches the tip, which is moving forward at U_{tip}. Therefore, we use U_{tip} as an estimate of the sheet velocity and U_s for the absolute retraction velocity of the film. We can thereby estimate $U_{TC} = U_s - U_{tip}$ and thus the sheet thickness at the location where it ruptures, i.e. $\delta = 2\sigma/\rho(U_s - U_{tip})^2$ (Fig. 2.5). This suggests that the sheet still remains intact while the film is as thin as 300 nm and only ruptures when it touches the pool. Figure 2.6 shows higher-resolution dual-frame images of the breakup of the sheet, where the film breaks up into tendrils, with thicker heads, which subsequently break up into a spray of micro-droplets.

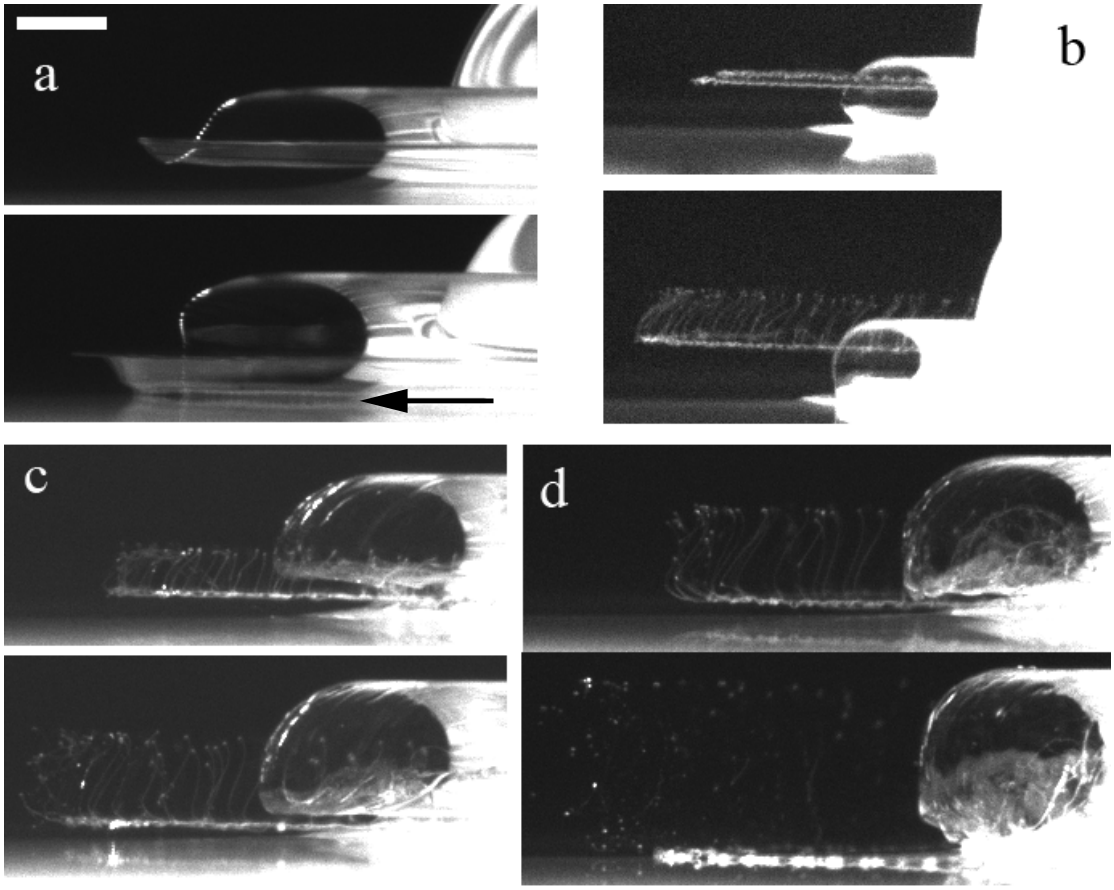

Figure 2.6: Dualframe PIV camera images of ejecta sheet breakup in tendrils and slingshot droplets, $Re \simeq 3500$. Times between image pairs (dt) are (a) 50; (b) 35; (c) 50 and (d) 100 μs. The arrow in lower panel of (a) points out the rupture of the film as it touches the pool. Bar is 1 mm.

Estimates of δ based on the tendril diameters also give submicron film thicknesses.

The bending of the sheet towards the pool is produced both by the kinematics of ejection, as is shown in the below model, but more importantly by air resistance. This was demonstrated by experiments in partial vacuum. Figure 2.7 compares two impacts, where only the air pressure P_g is changed, by a factor of 5, showing that at reduced air pressure the sheet does not bend downwards, but rather rises away from the pool. Another indication of the effect of the air, is that as the elbow approaches the pool surface, it is strongly accelerated downwards, due to the enclosure of the rising torus of air, which in combination with incompressibility demands that air be pulled under the elbow. This generates Bernoulli suction

pressure as the film closes to entrap the air torus (Thoroddsen et al., 2008, Deegan et al., 2008), with a similar mechanism as the bubble separation described in Gordillo et al. (2005) and Gekle et al. (2010). Figure 2.8 tracks the motion of the *elbow* next to the tip of the ejecta, over a range of air pressures, highlighting the central role of the air resistance.

2.4 Theoretical modeling

The initial ejecta shown herein are characterized by highly curved shapes. Similarly curved forms can be produced by pure kinematics. This is perhaps most clearly demonstrated by a simple geometric model of a sheet ejected by a solid sphere of radius R_{sp} impacting onto a flat free surface with velocity V_{sp}, see inset of Fig. 2.9(a). In this model the ejection velocity V_e is assumed to be directed tangentially to the sphere at its intersection with the original liquid surface, with a speed proportional to the normal velocity of the sphere at this contact line, i.e. $V_e = CV_{sp}cos(\theta)$, where C is the proportionality constant. Experimental (Thoroddsen, 2002) and theoretical results (Josserand and Zaleski, 2003) show that $C = C'Re^{1/2}$, with $C' \simeq 0.14$. If the initial contact occurs at time $t = 0$ and the surface remains flat, then the location of the contact point moves outwards along the flat surface as $x_c(t) = \sqrt{V_{sp}t(2R_{sp} - V_{sp}t)}$. The radial velocity of the contact point

$$V_c(t) = \frac{dx_c}{dt} = \frac{V_{sp}(R_{sp} - V_{sp}t)}{\sqrt{V_{sp}t(2R_{sp} - V_{sp}t)}} \propto \frac{1}{\sqrt{t}}$$

is initially infinite, dictated by the sphere geometry. The jetting velocity, in the model, is however finite: CV_{Sp}. More realistic model, suggests that the sheet only emerges when this velocity exceeds the outwards motion of the contact point. This occurs when $V_e = V_c$, i.e. at $t_e \simeq R_{sp}/2C^2V_{sp}$. This point is marked by a bead on the curve, giving the initial angle of ejection. By pure kinematics we let each fluid element move in a straight line after being ejected. The shape of the ejected

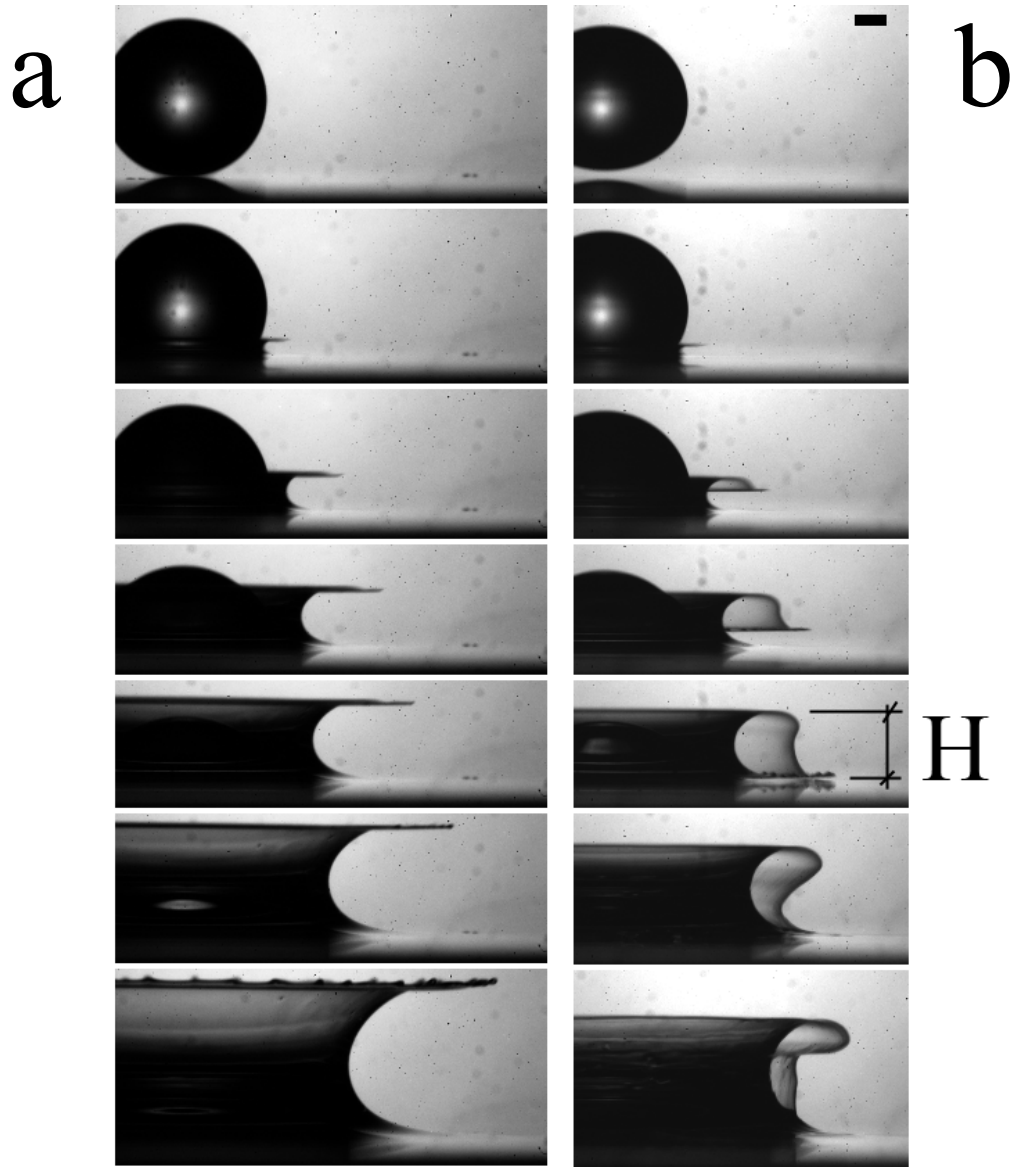

Figure 2.7: Effect of air pressure on the ejecta shapes. Impact of a 73% glycerin/water drop (D = 5 mm) onto a liquid layer, for different air pressures, for $Re \simeq 820$ and $We = 2700$. (a) P_g = 0.21 bar and (b) P_g = 1.0 bar. Times shown are $\simeq$ 0, 150, 300, 450, 600, 850, 1250 μs. The scale bar is 1 mm.

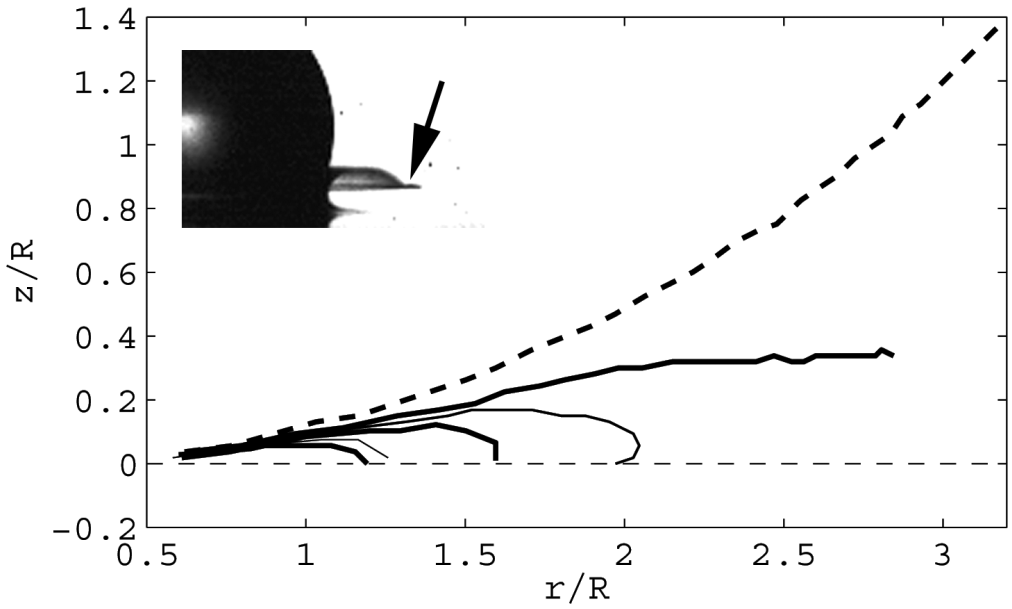

Figure 2.8: Effect of air pressure on the trajectory of the edge of the ejecta sheet. We follow the elbow just behind the tip, as this point touches the pool first. The curves correspond to air pressures of (from bottom to top curve) P_g = 1.0, 0.74, 0.47, 0.34, 0.28, 0.14 (broken line) bar. Data is for 58% glycerin/water mixture at Re = 2450 and We = 2700. The distances are normalized by the drop radius.

sheet can now be observed at time τ akin to the way one describes a *streakline* in unsteady flow, with t as the parameter to identify each fluid element. The location of fluid element ejected at t and observed at time τ is

$$x(t,\tau) = x_c(t) + V_e cos(\theta)\,(\tau - t) \tag{2.1}$$

$$y(t,\tau) = V_e sin(\theta)\,(\tau - t) \tag{2.2}$$

where θ is a function of t and $t < \tau$. Next we substitute for V_e and without loss of generality we normalize the space coordinates by R_{sp}, the velocity by V_{sp} and time by R_{sp}/V_{sp}. These equations thereby become:

$$x(t,\tau) = \sqrt{t(2-t)} + C(1-t)^2(\tau - t) \tag{2.3}$$

$$y(t,\tau) = C(1-t)\sqrt{t(2-t)}(\tau - t) \tag{2.4}$$

This produces a variety of space-curves, which help explain why the sheet appears to bend towards the pool. Figure 2.9 shows kinematic shapes for a few values of τ and a fixed C. Related results have be obtained by Peregrine (1981) for circular jet impacting a shallow liquid layer. However, the experiments in partial vacuum show that the air resistance is instrumental in promoting *catastrophic* bending, when considering the air resistance for motions perpendicular to the sheet. This is shown in Fig. 2.9(b) where we add air resistance to the component of the motion which is normal to the sheet U_n, based on high Re form-drag $\propto U_n^2$, giving normal deceleration $\propto \rho_{air} U_n^2/(\rho\delta)$. Using the same initial ejecta conditions, when we integrate the motions including this drag, we see the axisymmetric sheet deform into shapes more similar to the experiments.

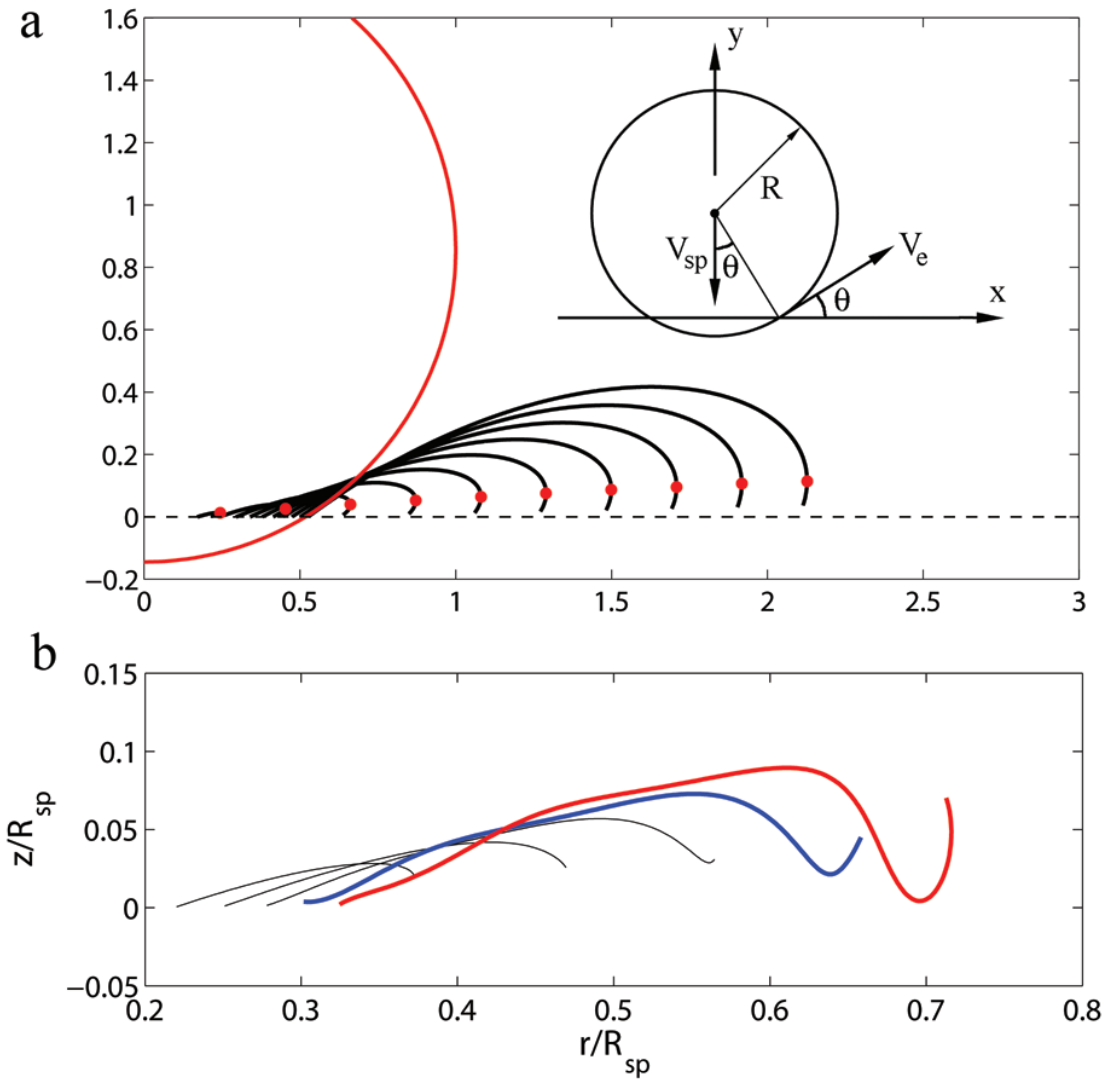

Figure 2.9: (a) Kinematic model of the sheet evolution for C = 14, plotted for $\Delta\tau$ = 0.015. (b) Evolution of the curved liquid sheet, subjected to air resistance, but ignoring viscous stress and surface tension, for R_{sp} = 2.5 mm, V_{sp} = 4 m/s and δ = 30 μm. The drag coefficient is fixed at C_d = 2. The tip is kept slightly thicker to mimic the observed bead produced by surface tension. Shapes shown until 200 μs.

Conclusion

In this letter we investigate a new mechanism of micro-droplet splashing through rupturing of ejecta sheets, which differs from earlier mechanisms (Rioboo et al., 2001, Yarin, 2006, Roisman et al., 2006, Villermaux, 2007, Lhuissier and Villermaux, 2009) and produces much smaller droplets than the typical crown breakup. The influence of the air pressure arises here through changes in the gas density and not by the compressibility of the air, as proposed by Xu et al. (2005) for droplet splashing on a solid surface. This is clear as the value of the Mach number for the ejecta sheet is $Ma \sim 0.1$ and the fact that compressibility effects scale as Ma^2. The gas pressure does not affect the emergence of the ejecta sheet which is determined by the early dynamic pressure inside the liquid, but greatly effects the bending of the sheet. It remains to be determined how the gas density $\rho_g \propto P_g^{-1}$ can be incorporated into the non-dimensional description of the phenomenon. Keep in mind that the gas dynamic viscosity is insensitive to the air pressure. Numerous other intriguing but robust ejecta shapes have been observed (e.g. Fig. 8 in Thoroddsen et al. (2008)) which require further study to shed new light on the dynamics of rapidly stretched submicron sheets of liquid.

Chapter 3

von Kármán vortex street within an impacting drop

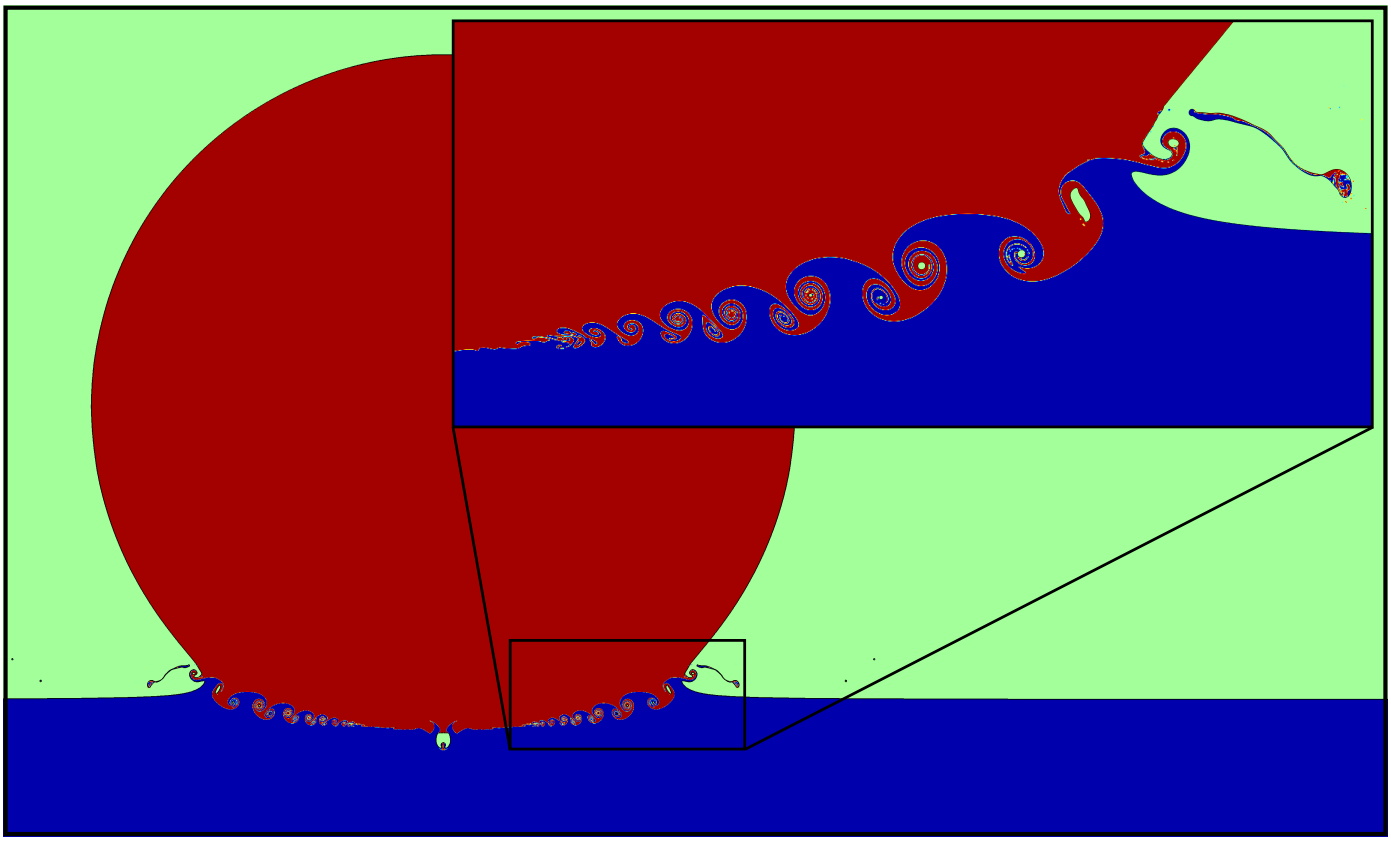

Figure 3.1: Vortex street developing during the early contact between the drop and the pool, for $K = 7.44 \times 10^4$ and $Re = 3552$, at $t^* = 0.084$.

Abstract

The splashing of a drop impacting onto a liquid pool produces a range of different sized microdroplets. At high impact velocities, the most significant source of these droplets is a thin liquid jet emerging at the start of the impact from the neck that connects the drop to the pool. We use ultrahigh-speed video imaging in combination with high-resolution numerical simulations to show how this ejecta gives way to *irregular splashing*. At higher Reynolds numbers, its base becomes unstable, shedding vortex rings into the liquid from the free surface in an axisymmetric von Kármán vortex street, thus breaking the ejecta sheet as it forms.

This chapter is based on Thoraval et al. (2012b).

3.1 Introduction

Liquid drop splashing is part of our daily lives, from the morning shower to natural rain (Rein, 1993, Yarin, 2006). While it has been studied for more than one hundred years (Worthington, 1882), it is only recently that advances in high-speed imaging techniques (Etoh et al., 2003, Thoroddsen et al., 2008) have revealed its early dynamics (Thoroddsen et al., 2011, Zhang et al., 2012). Splashing refers herein to the breakup of a drop into smaller droplets during impact. Understanding the underlying mechanism that produces the smallest droplets is important, for example, for the number of microscopic aerosols which remain when those satellite droplets evaporate. Such aerosols affect human health and can act as nucleation sites during cloud formation.

For high-speed drop impact on a liquid pool, the *ejecta sheet* is the first stage leading to splashing. It was first observed in the inviscid numerical simulations of Weiss and Yarin (1999) and in the experiments of Thoroddsen (2002). When the drop impacts at higher velocity, the speed of these ejecta sheets increases and they become thinner. The radial stretching of the sheets reduces their thickness even further, and they can remain intact even at thicknesses well under a micron (Thoroddsen et al., 2011). When they eventually rupture, they can produce a myriad of very fine spray droplets. However, this mechanism does not continue for ever; at a critical Reynolds number, the smooth ejecta gives way to a more random splashing, which counter-intuitively may produce fewer small droplets.

3.2 Experimental exploration

To understand the mechanisms leading from continuous ejecta sheets to *irregular splashing*, a systematic study of the early dynamics was conducted with ultrahigh-speed video imaging, over a range of impact velocities U, liquid viscosities μ and droplet diameters D. The liquid viscosity was varied in our experiments

by using glycerin/water mixtures of various mass fractions: 0, 40, 50, 60, 65, 70, 75, and 80% of glycerin. The impact velocity was changed by releasing the drops from between 0.16-2.16 m height. By varying the circular steel nozzle size, we used four different drop diameters: 3.2, 4.6, 5.1, and 5.7 mm. Further imaging details of the experiments can be found in Thoroddsen et al. (2011).

Figure 3.2 shows a classification of the results in terms of Reynolds number $Re = \rho DU/\mu$, where ρ is the liquid density, and splashing parameter K, which relates to the Weber number $We = \rho DU^2/\sigma$, where σ is the surface tension, as $K = We\sqrt{Re}$. We are interested here in the higher K regime, where splashing occurs (Stow and Hadfield, 1981, Mundo et al., 1995, Cossali et al., 1997).

The classification in Fig. 3.2 focuses on the ejecta shapes. In the lower range of Re (more viscous liquids), a smooth ejecta sheet emerges between the drop and the pool (●). However, in the highest range of Re, isolated droplets emerge from the neck, followed by a disturbed liquid surface, and no coherent ejecta can be identified; i.e., *irregular splashing* occurs (■). In the intermediate regime ($Re \approx 2000 - 6000$), the ejecta sheets show a large variety of repeatable shapes. We have grouped them into 3 classes. At lower K (lower impact velocities, ♦), surface tension prevents the formation of an ejecta sheet. However, we observe some protrusions travelling up along the side of the drop, without ejection of droplets outwards (Zhang et al., 2012). At higher K (▲), the ejecta sheet is more developed; however, it stays attached to the drop, stretching the ejecting sheet between the expanding tip of ejecta and the drop entering the pool. This regime is called *quartering*. This stretching can lead to the explosive rupturing of the sheet, which generates fast droplets of a large range of sizes through slingshot (Thoroddsen et al., 2011), by surface tension pulling on a free liquid sheet. In the upper range of K (▽) we observe an intriguing phenomenon where the freestanding sheet interacts strongly with the downward-moving drop surface. This is shown in the sequence of Fig. 3.3(a), referred to as the *bumping* of the ejecta. The ejecta

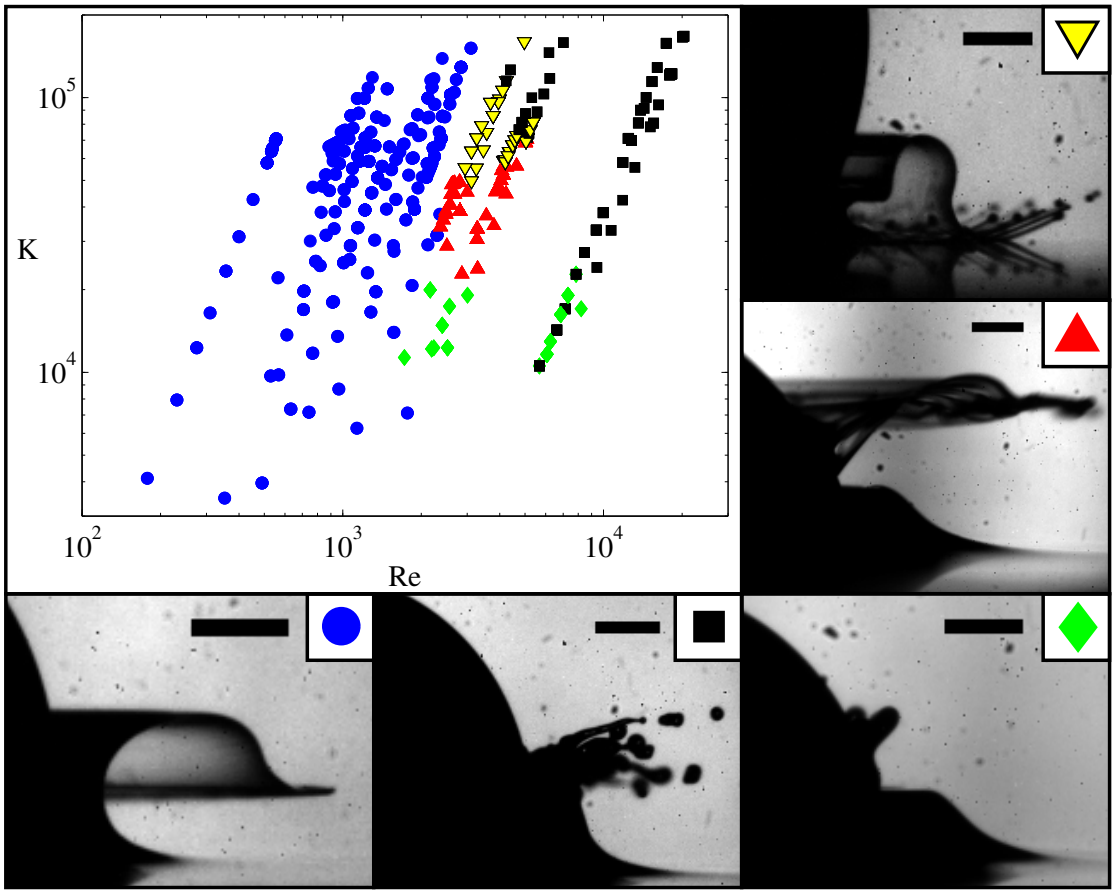

Figure 3.2: Characterization of the ejecta regimes.
(●) Smooth ejecta sheet (t = 145 μs, Re = 1410, $K = 5.62 \times 10^4$).
(■) Irregular splashing (t = 360 μs, Re = 1250, $K = 7.11 \times 10^4$).
(▽) Bumping (t = 180 μs, Re = 3550, $K = 7.44 \times 10^4$).
(▲) Quartering (t = 630 μs, Re = 2810, $K = 3.86 \times 10^4$).
(♦) Protrusions rising up along the side of the drop (t = 630 μs, Re = 2410, $K = 1.48 \times 10^4$).
The scale bars are all 500 μm long.

is strongly bent by the drop, and then folds at its apex. Overall snapshot of a bumping ejecta was included in Thoroddsen et al. (2008) [their Fig. 8(c)].

Those experimental results clearly show the effect of the Reynolds number on the transition toward *irregular splashing*. Moreover, the results show new dynamics of the ejecta sheet interacting with the drop. This suggests that those interactions could underlie the irregular splashing.

3.3 Numerical simulations

3.3.1 Numerical method

To test this idea, we have chosen to reproduce the impact by numerical simulations. It is only recently that numerical simulations managed to identify the ejecta sheet (Weiss and Yarin, 1999, Josserand and Zaleski, 2003, Coppola et al., 2011), because of the extreme range of scales involved and the challenges of interfacial flow simulations (Tryggvason et al., 2011). The intricate shapes observed herein were beyond reach in previous studies.

We use the freely available code Gerris (Popinet, 2009, Agbaglah et al., 2011, Popinet, 2011) for its high parallelization and dynamic adaptive grid refinement, which allow us for the first time to reach enough precision to fully resolve the dynamics of the ejecta. This code uses the *Volume-Of-Fluid* method to solve the incompressible Navier-Stokes equations. Furthermore, we start the simulation before impact, thus capturing the air-cushioning effect (Xu et al., 2005, Driscoll and Nagel, 2011, Duchemin and Josserand, 2011, Mandre and Brenner, 2012, Kolinski et al., 2012, van der Veen et al., 2012).

The same parameters as in the experiments were used for the numerical simulations. The air has a density of 1.21 kg/m^3, and a viscosity of 1.81×10^{-2} cP. Surface tension was kept constant, at 67.4 mN/m, neglecting the small variations with water/glycerin mixture fraction. Gravity was also taken into account with

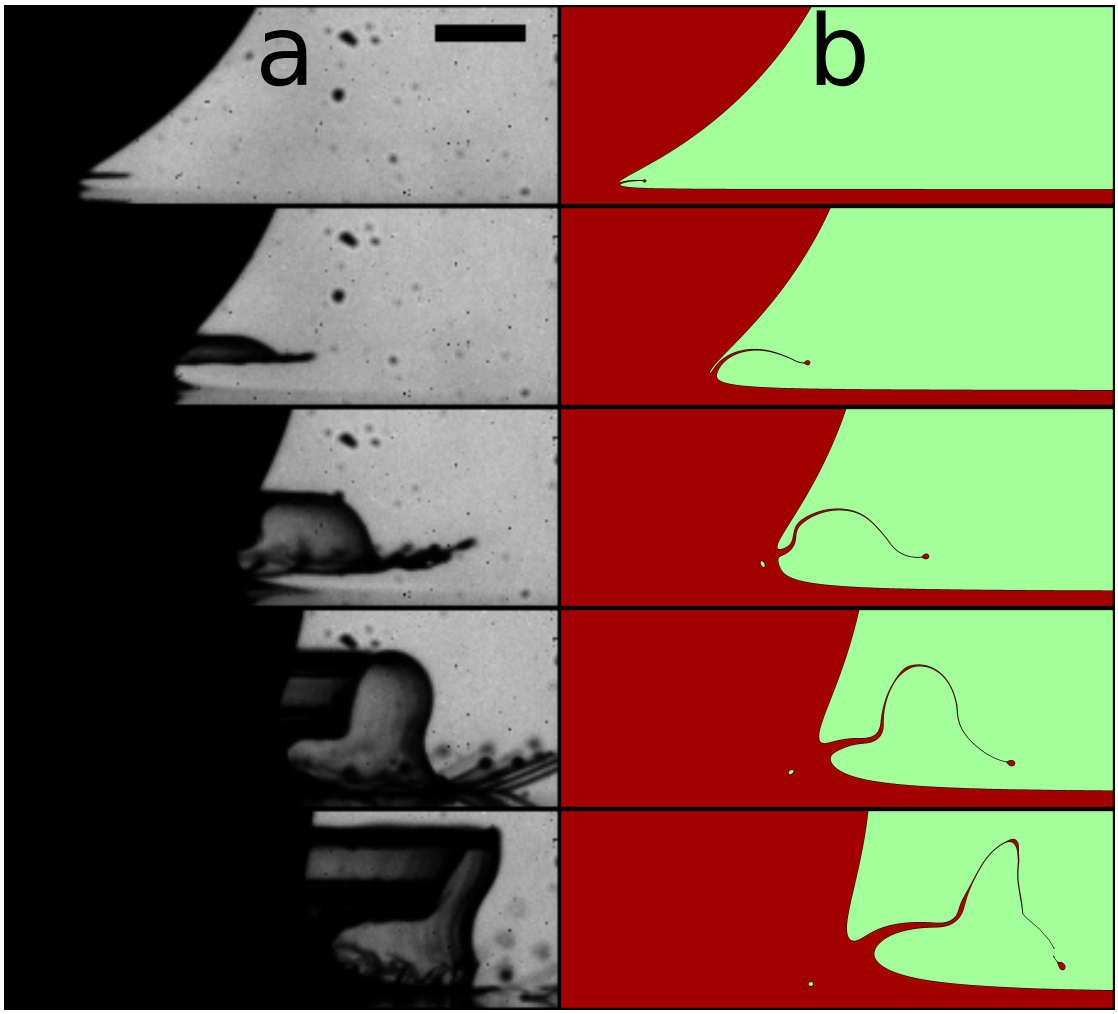

Figure 3.3: Comparison between experiment and axisymmetric numerical simulation for a bumping case. $U = 4.04\ m/s$, $D = 4.6\ mm$, $Re = 3.55{\times}10^3$, $K = 7.44{\times}10^4$. From top to bottom, observations at time 30, 80, 130, 180, and 230 μs after contact. (a) Experimental observation. The static dark points correspond to dust on the camera sensor. The video was taken at 200 000 frames per second. (b) Numerical simulation of the drop impact for exactly the same times after impact, same scale and same field of view as in the experiment presented in (a). In the last image, the leading part of the ejecta sheet becomes smaller than the grid size by stretching between the apex and the tip and thus breaks into nonphysical droplets. The axisymmetric simulations cannot include the three-dimensional effects, such as the breakup of the tip observed in (a). The scale bar is 500 μm long. Supplemental videos show the two evolutions.

$g = 9.81\ m/s^2$, and the drop diameter was kept constant $D = 4.6\ mm$. The Re and K parameters were varied by changing the liquid viscosity, and impact velocity, in a similar way as in the experiments. More details on the numerical simulations are given in Appendix A.

3.3.2 Comparison with experiments

Axisymmetric simulations faithfully reproduced all of the experimentally observed features, as we demonstrate in Fig. 3.3 for the bumping case. The shape of the drop in the simulation is perfectly spherical, ruling out the hypothesis that small deviations from spherical drop shapes in the experiments could be responsible for the drop interaction with the ejecta sheet.

Numerical simulations even suggest that the bumping event (when the drop impacts on the ejecta sheet) is responsible for the entrapment of a bubble ring between the ejecta sheet and the drop, as shown for example in the third line of Fig. 3.3.

3.4 Transitions to irregular splashing

To study the transition to irregular splashing we increase Re, while keeping K constant, from a smooth ejecta sheet [Fig. 3.2(●)] to irregular splashing (■). This was done for two different K values, corresponding to the bumping (▽) and quartering (▲) regimes.

We define the base of the ejecta sheet as the points of maximum curvature, and the angle θ it makes with the horizontal [Fig. 3.4(a)]. The curvature of the tracer isolines was estimated by fitting a Bézier curve of order 3 through 5 points. For smaller curvature cases, the number of points was increased to 11, improving the estimate of the position of maximum curvature. This allowed the following measurements of Fig. 3.4 to be extracted automatically by an octave script.

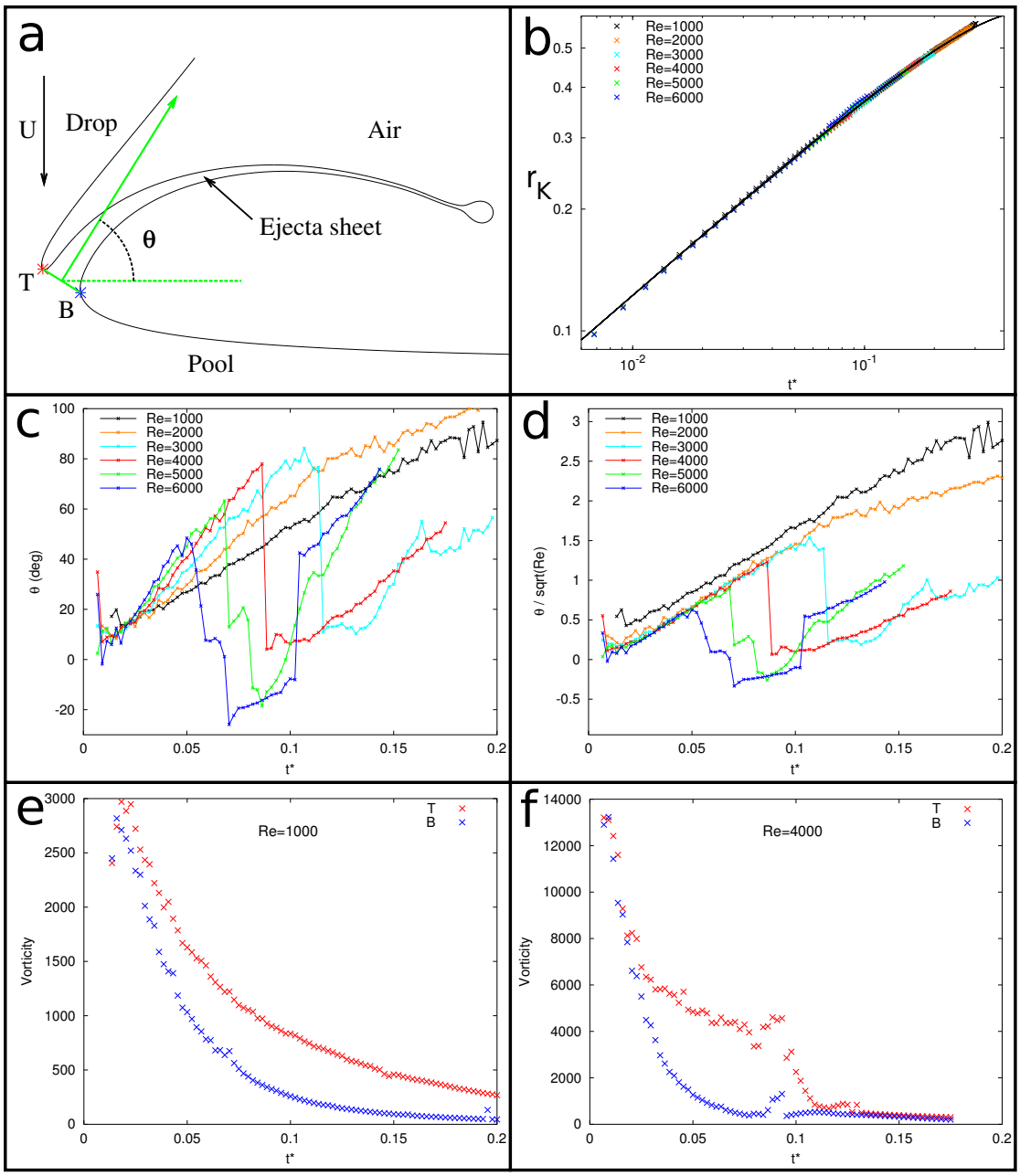

Figure 3.4: Evolution of the base of the ejecta sheet with Re at $K = 7.44 \times 10^4$. Quantities are nondimensionalized by the drop diameter D, the drop impact velocity U and the drop entry time $\tau = D/U$. (a) Definition sketch. The base of the ejecta sheet is defined as the segment between the two points of maximum curvature of the interface (T on the drop side and B on the side of the pool). The angle of the ejecta sheet θ is the angle between the horizontal and the normal to the base. (b) Evolution of the ejecta base radial position r_K, defined as the distance from the axis of symmetry to the middle of TB in (a), vs the nondimensional time $t^* = t/\tau$, for Re from 1000 to 6000. The solid curve is $1.23 r_J$, where $r_J = \sqrt{t^*(1-t^*)}$ is the radius where an undisturbed drop would meet the pool. (c) Evolution of θ (in degrees) for Re from 1000 to 6000. The sharp drops correspond to bumping events, as the position of T suddenly moves up along the drop side. (d) Same curves as (c), where the angle is scaled by $\sqrt{Re}$. (e,f) Evolution of the maximum positive vorticity (red) and maximum absolute negative vorticity (blue) in the liquid near the ejecta base for $Re = 1000$ (e) and $Re = 4000$ (f). The positive maximum is located near T, and the negative maximum near B.

The position of the base of the ejecta r_K [Fig. 3.4(b)] follows very closely the geometric relation predicted by Josserand and Zaleski (2003) $r_K = Cr_J$, independent of Re, where r_J is the radius where an unperturbed drop would meet the original pool surface. A simple geometric model (Thoroddsen et al., 2011) suggested that θ increases as $\theta \sim \sqrt{t^*}$, where t^* is the time nondimensionalized by $\tau = D/U$, whereas the simulations show that θ grows linearly before bumping [Fig. 3.4(c)]. However, the ejecta rises faster for higher Re. The collapse of the curves in Fig. 3.4(d) shows that θ grows at a rate proportional to $\sqrt{Re}$. The angle of the ejection-velocity vector at the middle of the base also follows a similar trend, and increases proportionally to $\sqrt{Re}$.

At lower Re, θ increases slowly enough for the ejecta to escape the drop. However, from $Re \gtrsim 3000$, the ejecta sheet rises too fast, thus impacting the drop surface. The resulting bumping sharply decreases θ. This interaction of the drop and the ejecta sheet observed experimentally occurs earlier at higher Reynolds numbers, eventually breaking the ejecta sheet. This is consistent with the interpretation that this interaction is responsible for the irregular splashing observed at higher Re.

Therefore, the bumping and the early irregular splashing arise from the dynamics in the neck region rather than the subsequent deformation of the ejecta sheet itself. Thus, bumping is the illustration of a new type of instability leading to early irregular splashing.

3.4.1 Vorticity production

Vorticity also plays an important role in the dynamics of the ejecta sheet [Figs. 3.4(e) and 3.4(f)]. For a stationary two-dimensional free surface, vorticity is generated at the free surface proportionally to the interface curvature κ and the tangential flow velocity q: $\omega = 2\kappa q$ (see for instance Batchelor (2000, § 5.14), and Peck and Sigurdson (1994), Cresswell and Morton (1995) for low We drop

impacts). This vorticity is then diffused into a thin boundary layer, which can separate to enter the liquid.

Numerical simulations indeed show concentrated vorticity near points T and B at the base of the ejecta as the flow moves faster around the highly curved base to enter the ejecta (Fig. 3.5). At the early stage of the ejecta formation, both sides of the base produce a similar strength of vorticity [Fig. 3.7(a)]. This initial vorticity scales as $\sqrt{Re}$ as observed previously by Josserand and Zaleski (2003). However, the difference in vorticity (absolute values) between the two sides increases initially linearly with time, before decreasing again. Moreover, this difference is higher for larger Re [Fig. 3.4(f)].

3.4.2 Vorticity shedding into the liquid

By looking closely at the neck region during the impact, we can identify fundamental changes in the vorticity structure as Re is increased (Fig. 3.5). Note that in Fig. 3.5(a) most of the liquid in the sheet originates from the pool, in agreement with dye visualizations of Thoroddsen (2002). For the lower range of Re [Figs. 3.5(a) and 3.5(d)], the vorticity stays concentrated near the free surface at the neck of the ejecta sheet. As there is stronger vorticity generated at the top of the ejecta base, a vorticity layer of one sign separates the drop and the pool liquids but it remains stable. K affects the shape of the outer part of the ejecta sheet, as we observe by comparing Figs. 3.5(a) and 3.5(d), consistently with experimental observations of Thoroddsen et al. (2011). For intermediate Re, the interface remains stable in its early evolution. In the bumping case (b), the rising ejecta sheet contacts the downward-moving drop surface. This creates a shear instability, generating a toroidal vortex structure around the entrapped bubble. In the quartering case (e), the ejecta sheet leaves the neck region to climb up the drop, pulled by higher surface tension. This also creates a shear instability between the climbing liquid from the pool and the drop liquid moving down, forming a row

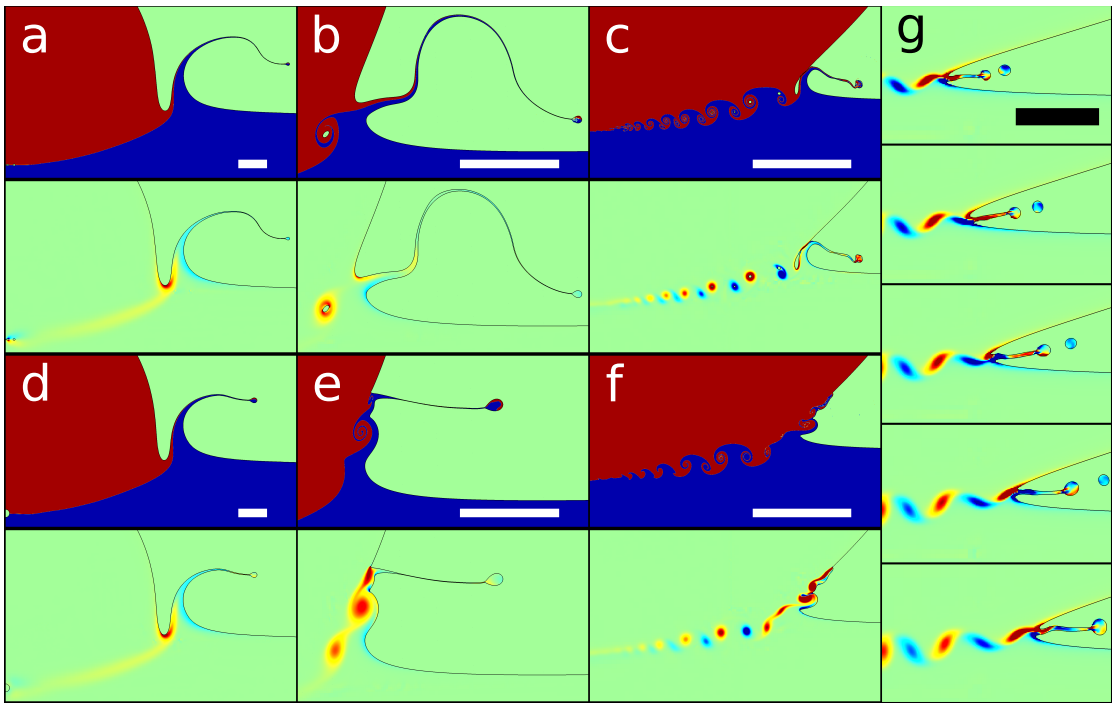

Figure 3.5: Vorticity structures during drop impact near the transition regime between a smooth ejecta sheet and irregular splashing. In the top images we differentiate the liquids originating from the drop (red) and from the pool (blue), from the air (green), as can be done in experiments by seeding one or the other with fluorescent dye (Thoroddsen, 2002). The bottom images show the corresponding vorticity in the liquid. (a-c) Bumping transition, with $K = 7.44 \times 10^4$, for increasing Reynolds numbers: $Re = 1000$, 3552, and 14 500, respectively. (d-f) Quartering transition, with $K = 3 \times 10^4$, for $Re = 1000$, 3552, and 10 000, respectively. To allow direct comparison, the images of the first row (a-c) correspond to the same nondimensional time ($t^* = 0.343$, 0.150, and 0.066, respectively) as the ones in the second row (d-f), with the same field of view. (c) and (f) correspond to a water drop of $D = 4.6$ mm impacting at 2.84 m/s and 1.98 m/s respectively. In both cases, a vortex street develops. However, bubbles rings are entrapped only at higher splashing parameter (f). (g) Details of the early vortex shedding in the same case as (c), from $t^* = 1.02 \times 10^{-2}$, and then a constant $\Delta t^* = 4.5 \times 10^{-4}$. The period of this shedding shown here is approximately 3 μs, over a radial distance of 50 μm. The scale bars are $0.1D$ long for (a-f), and $0.01D$ long for (g).

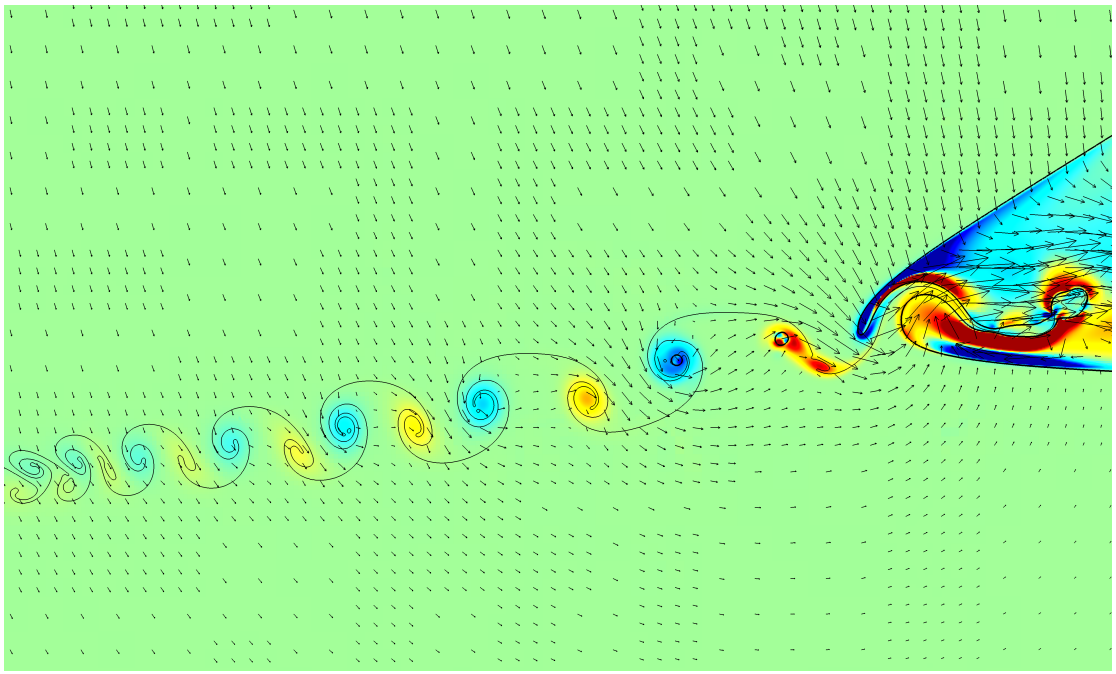

Figure 3.6: Vortex street in the same conditions as Fig. 3.5(c). The colours represent the strength of the vorticity in the liquid and the air. The vectors show the velocity field. The thick line is the interface air/liquid, while the thinner line is the interface between the liquid from the drop and the liquid from the pool.

of vortex rings of the same sign. These vortices near the free surface leave their signature (Yu and Tryggvason, 1990) by creating waves below the rising sheet, a feature also observed experimentally (Fig. 3.2) (Zhang et al., 2012). However, all such vortical effects are absent from inviscid theory and simulations (Weiss and Yarin, 1999, Howison et al., 2005).

3.5 Oscillations of the ejecta sheet at higher Re

3.5.1 Vortex street

At even higher Re [Figs. 3.5(c), 3.5(f) and 3.6], vorticity is shed behind the base of the ejecta sheet, in a way reminiscent of the von Kármán vortex street, here forming alternating-sign vortex rings. For the first 7 shedding cycles, the local Reynolds number based on the radial speed and width of the neck takes value around 70 and the Strouhal number $St = fD/U$ is around 0.11 ± 0.05, in

good agreement with related Kármán streets behind a cylinder.

During the early shedding [Fig. 3.5(g)], surface tension effects are higher because of the sharper surface geometry. As the angle of the neck increases, the amplitude of the oscillations increases. The ejecta can then climb on the drop at lower K (f) or impact alternatively on the drop and the pool (c) in a similar way to the bumping, entrapping a row of bubble rings (Weiss and Yarin, 1999, Davidson, 2002). Four bubble rings can be clearly identified in Fig. 3.5(c), with a fifth one being created. Only well-resolved bubbles and droplets (larger area than 30 cells) are kept in the numerics, suggesting that smaller bubbles could be entrapped earlier.

3.5.2 Onset of Vortex Shedding

An intriguing question remains, i.e., what causes the oscillations of the ejecta base? The analogy with the vortex shedding of a cylinder suggests that vorticity can be responsible for the oscillations of the base (Williamson and Govardhan, 2004) and would be present even without them. However, those oscillations will amplify the vorticity difference between the two sides of the base through surface curvature, reinforcing the oscillations and the separation of individual vortices. Therefore, we observe an unstable mode that involves both the jet and the vortex street.

At a lower Reynolds number than the one shown in Fig. 3.5(c), small oscillations can be identified in the early evolution of the ejecta sheet [Fig. 3.7(a)]. They are visible also in the early times of Figs. 3.4(c) and 3.4(d), with less details. However, they stop rapidly, and do not lead to the breakup of the ejecta sheet [Figs. 3.7(b) and 3.7(d)].

We conclude that vorticity layers can be shed, but as soon as these layers start to break up into isolated vortices the base of the ejecta starts to oscillate. However, the transition onset to shedding is gradual, and the first oscillations at the base

are not sufficiently strong to break up the jet, but rather make it wiggle, leaving slight bends in its shape [see Fig. 3.7(b)].

The analogy for vortex shedding behind solid cylinders, is the formation of symmetric separation bubble, which subsequently at some critical *Re* starts oscillating sideways starting the vortex shedding. The strong sideways forces due to this shedding can then feed back to the solid structure, through aeroelastic effects, making high-rise buildings sway from side to side.

Conclusions

From systematic experimental observations, reproduced with axisymmetric simulations, we have detailed a new mechanism explaining the irregular splashing of a water drop. Previously studied mechanisms have described the droplet separation from the rim of the ejecta (Gueyffier and Zaleski, 1998, Weiss and Yarin, 1999, Zhang et al., 2010), or the wave-driven instability of a liquid sheet driven by the surrounding air (Dombrowski and Johns, 1963, Villermaux and Clanet, 2002). Our mechanism, however, explains the breakup of the ejecta sheet by a fundamentally different mechanism, based on the destabilization of its base, through vortex shedding from the free surface.

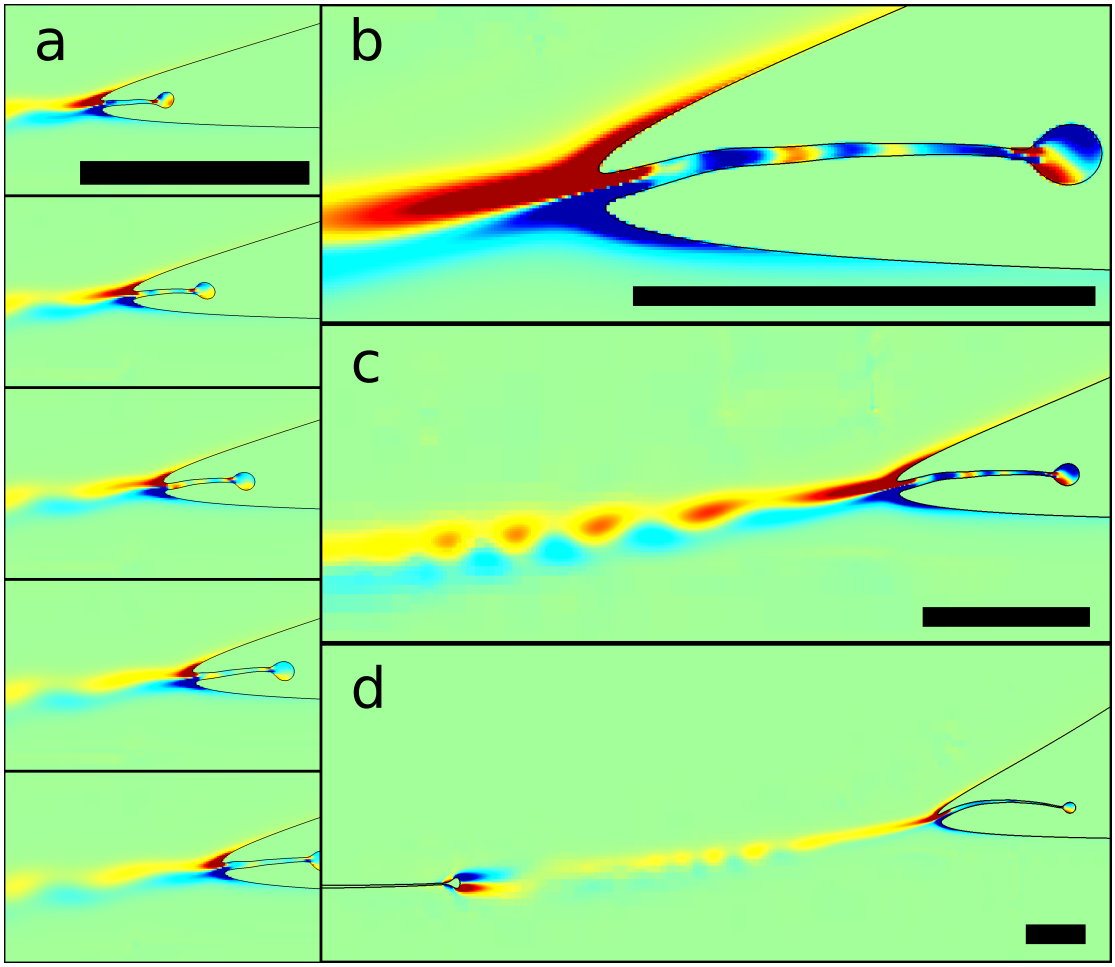

Figure 3.7: Vorticity structures under the drop for $K = 7.44 \times 10^4$ and $Re = 6000$, i.e., slightly below the critical Reynolds number for irregular splashing. (a) Time sequence showing the small oscillations of the base of the ejecta sheet, at the same location as Fig. 3.5(g), starting at $t^* = 1.02 \times 10^{-2}$, and then with constant $\Delta t^* = 4.5 \times 10^{-4}$. The color scale is also kept identical to Fig. 3.5(g) to show the weaker levels of vorticity. (b) At a later time ($t^* = 1.82 \times 10^{-2}$), small oscillations are visible on the ejecta sheet, at the same locations as some vorticity shed from the base. (c) Larger view of (b), showing the first vorticity oscillations shed behind. The base of the ejecta sheet does not oscillate after this time. (d) Later evolution at $t^* = 2.95 \times 10^{-2}$. The first vortices shed are diffusing, and the ejecta sheet does not oscillate anymore. The thin line on the left corresponds to the air disk trapped below the drop, later contracting into a bubble [see also Fig. 3.5(d)]. The scale bars are all $0.02D$ long.

Chapter 4

Drop impact entrapment of bubble rings

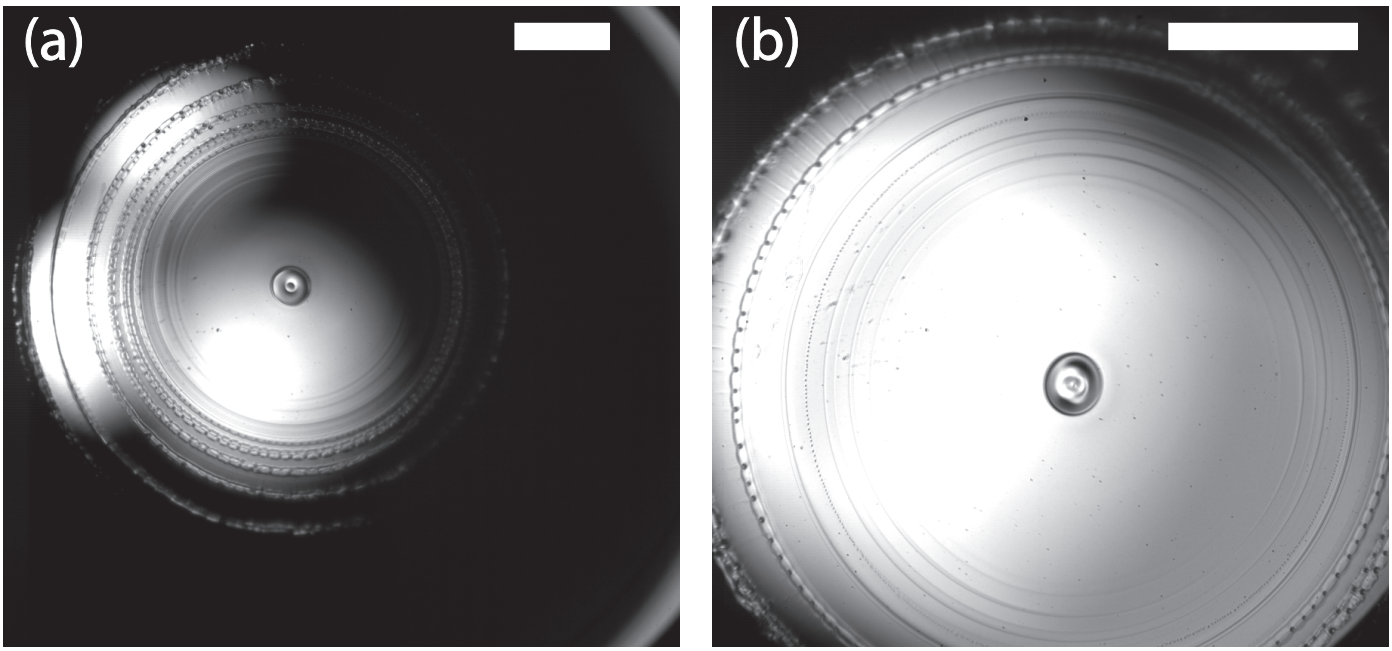

Figure 4.1: Bubble rings entrapped between a water drop and a thin film of ethanol within 100 μs after the first contact (Re = 11 600, α = 0.86, $\delta \simeq 40$ μm). (a) Overview of bubble rings and vortices observed below the drop. The side of the drop can be observed on the top and bottom right corners. The later dynamics shows that the third dark ring from the center contains a bubble ring, that cannot be identified here. (b) Magnification twice larger, showing the details of the first vortices and bubble rings. The bubbles in the smallest bubble ring are about 3 μm in diameter. Scale bars are 500 μm long.

Abstract

We use ultra-high-speed video imaging to look at the initial contact of a drop impacting onto a liquid layer. We observe experimentally the vortex street and the bubble-ring entrapments predicted numerically, for high impact velocities, by Thoraval et al. (2012b). These dynamics occur mostly within 50 μs after the first contact, requiring imaging at 1 million frames/sec. For a water drop impacting onto a thin layer of water, the entrapment of isolated bubbles starts through azimuthal instability, which forms at low impact velocities, in the neck connecting the drop and pool. For Re above about 12 000, up to 10 partial bubble-rings have been observed at the base of the ejecta, starting when the contact is ~ 20% of the drop size. More regular bubble rings are observed for a pool of ethanol or methanol. The video imaging shows rotation around some of these air cylinders, which can temporarily delay their breakup into micro-bubbles. The different refractive index in the pool liquid reveals the destabilization of the vortices and the formation of streamwise vortices and intricate vortex tangles. Fine-scale axisymmetry is thereby destroyed. We show also that the shape of the drop has a strong influence on these dynamics.

This chapter is based on Thoraval et al. (2013a).

4.1 Introduction

The impact of a drop onto a pool surface has been studied for over a century, but revolutionary improvements in high-speed video technology (Etoh et al., 2003) have recently opened up this canonical geometry to renewed scrutiny. This applies especially to the earliest contact between the drop and the pool, where intricate details have emerged and play a crucial role during air entrapment and splashing (Yarin, 2006, Thoroddsen et al., 2008).

The impact of a drop always entraps a bubble under the centre of the drop, as a disk of air is produced by the lubrication pressure and rapidly contracts into a bubble at the centre (Thoroddsen et al., 2003, Liow and Cole, 2007, Korobkin et al., 2008, Mani et al., 2010, Hicks and Purvis, 2010, Driscoll and Nagel, 2011, Kolinski et al., 2012, van der Veen et al., 2012). Following this central air disk entrapment on a liquid pool, the outer contact forms a neck, which emits an ejecta sheet for sufficiently large Reynolds numbers (Thoroddsen, 2002, Weiss and Yarin, 1999, Davidson, 2002, Josserand and Zaleski, 2003, Howison et al., 2005). These ejecta are the source of the finest spray droplets (Thoroddsen et al., 2011, Zhang et al., 2012), which is of relevance to numerous processes, such as combustion and aerosol formation.

However, at even larger impact energy, these smooth ejecta give way to random splashing of small droplets, see Thoroddsen (2002). Numerical simulations by Thoraval et al. (2012b) have shown that the base of the ejecta can become unstable, bending up and down as the free surface sheds alternate sign vortex rings into the liquid, and often entrapping bubble rings. These bubble rings alternate between the top and bottom sides of the ejecta. This air entrapment has important applications for inkjet printing and gas transfer at the liquid-air interface (Wanninkhof et al., 2009, Czerski et al., 2011), as it can generate hundreds of micro-bubbles. This regime is the focus of the current investigation.

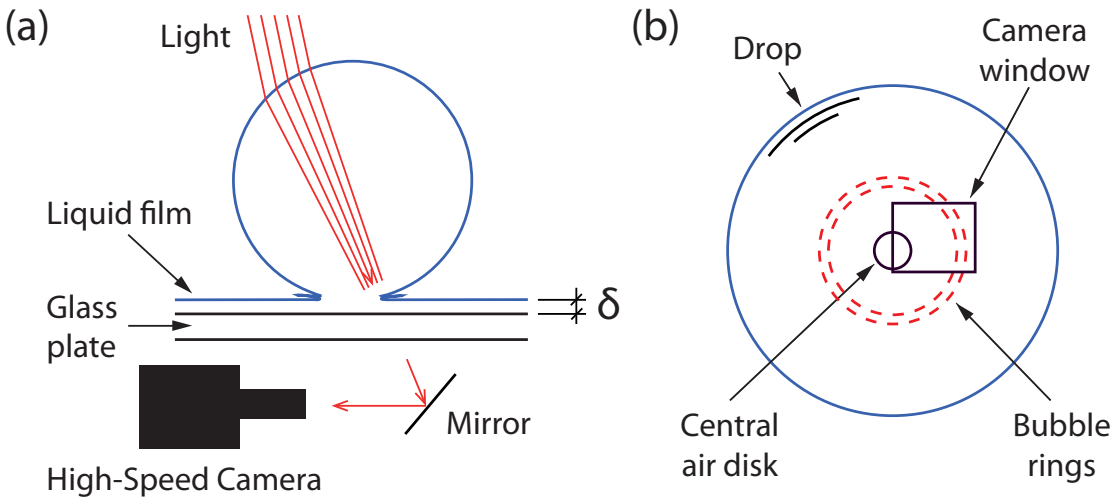

Figure 4.2: (a) Imaging setup. We use backlight imaging of the drop impact from below, through a glass plate. The drop acts as a lens focusing the illumination to a limited area on the observation window. Several lights were used in some cases to obtain a larger illuminated area. (b) Camera viewing area shown in bottom view, corresponding to the area in Fig. 4.12(c).

Very recent experiments by Castrejón-Pita et al. (2012) have used side-view and laser-induced fluorescence to verify the presence of the von Kármán street for conditions similar to those in Thoraval et al. (2012b). Herein we show the first experimental observations of the formation and breakup of the bubble tori.

The main axisymmetric features of the vortex street and bubble rings entrapments are observed experimentally. However, three-dimensional effects rapidly break the axisymmetry. Herein, we show that even at rather modest impact velocities, azimuthal instabilities can appear in the neck between the drop and the pool. Imaging using two different liquids also reveals the shedding of streamwise vortices and their intricate dynamics, similar to three-dimensional instabilities of the cylinder wake (Williamson, 1996), or the shear layer (Lasheras and Choi, 1988). These intricate structures have perhaps escaped earlier experimental notice as they develop in a sub-millimetre region and evolve in less than 50 μs.

4.2 Experimental Setup and Numerics

4.2.1 High-Speed Video Imaging

In this work we image drop impacts onto shallow pools through a bottom glass plate (Fig. 4.2). Limited imaging (only in Fig. 4.19(a,b)) was done from the side above the pool surface. We use identical water drops in the entire study, while changing the composition of the pool liquid. The pool liquids tested are water, ethanol and methanol which are all highly miscible with the water drop. The liquid properties are given in Table 4.1. The difference in refractive index between the water drop and the ethanol or methanol pools allows us to image the flow structures as they distort the interface between the two liquids.

The use of shallow pools, or thin films, is dictated by the need to change the pool liquid following every impact as well as by the optical setup, where the limited focal distance of the long-distance microscope rules out bottom views through deep pools. The liquid was contained by a 10 cm diameter ring glued onto the glass plate. The pool depth δ was varied from about 25 μm to 1 mm. It was estimated by controlling the volume of liquid with a syringe and assuming a uniform spreading inside the container. To minimize the effect of evaporation, the impact experiment was done within 10 seconds after spreading the liquid.

Here we use a long-distance microscope for magnifications up to about 15 for maximum pixel resolution of ~ 4.1 μm/px, when using the Shimadzu Hypervision CCD video camera (Etoh et al., 2003), at frame rates up to 1 million fps. Some of the imaging was also done at a lower frame rate with a Photron SA5 CMOS camera, with a magnification up to 10 and maximum pixel resolution ~ 2 μm/px. Using thin bottom layers restricts the vertical motion of the interface between the drop and the pool liquid during the impact, thereby making well-focused imaging easier with the limited focal depth. For further optical/triggering details see Thoroddsen et al. (2012b).

The drop is pinched from a 3 mm nozzle, to produce an effective drop diameter of $D = (D_v D_h^2)^{1/3} = 4.67$ mm, where D_v and D_h are the instantaneous vertical and horizontal diameters. We characterize the impact conditions by the Reynolds number Re, the Weber number We and the splashing parameter K, defined as:

$$Re = \frac{\rho D V}{\mu}, \qquad We = \frac{\rho D V^2}{\sigma}, \qquad K = We\sqrt{Re},$$

where ρ, μ and σ are respectively the density, dynamic viscosity and surface tension of the drop liquid, and V the drop impact velocity.

The drop velocity V was characterized in a separate set of experiments. It was then modelled by the velocity of a sphere experiencing constant drag (Pumphrey et al., 1989, Elmore et al., 1989, Pumphrey and Elmore, 1990, Saylor and Grizzard, 2004):

$$V = V_T \sqrt{1 - \exp\left(-\frac{2g\,(h - D - h_0)}{V_T^2}\right)}, \tag{4.1}$$

where gravity is $g = 9.81$ m/s^2, with the fitting parameters $V_T = 9.11$ m/s and $h_0 = 2.1$ mm. V_T corresponds to the terminal velocity of the drop, and h_0 to the effective pinch-off length of the drop when it separates from the nozzle. Here h is the measured distance from the nozzle tip to the undisturbed pool surface, whereas the adjusted height is defined as $H = h - D - h_0$.

Figure 4.3(a) shows that the measured values of V are less than 0.8% away from the formula, for our impact heights 2.5 cm $< H <$ 55 cm. This estimate of V_T is slightly higher than the experimental observations of Gunn and Kinzer (1949), which could be due to the drop oscillations before reaching a final oblate shape. Indeed, the oblate shape would give a larger horizontal radius, and therefore a larger drag. We can calculate the falling time of the drop from the falling height as:

$$t = \frac{V_T}{g} \operatorname{argcosh}\left[\exp\left(\frac{gH}{V_T^2}\right)\right]$$

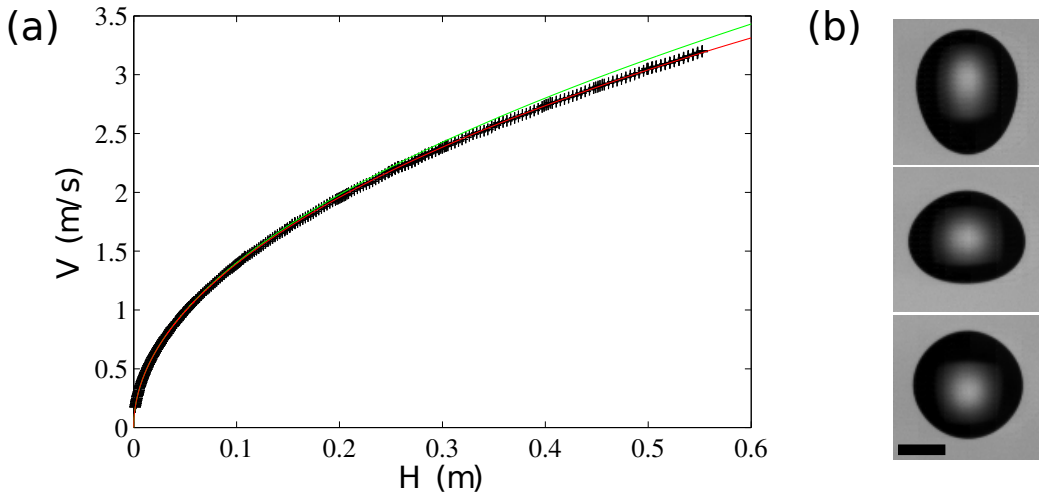

Figure 4.3: (a) Drop velocity V vs. falling height H. The green line corresponds to $\sqrt{2gH}$, while the red line is our fitting equation. For a better accuracy, each measurement only covered a falling height of approximately 6 cm, with an overlap between each height. This explains the larger number of points in the overlap regions. A total of 42 different observations were needed, with a minimum of 3 for each height. (b) Typical drop shapes in air: prolate ($\alpha > 1$, $H = 31.2\ cm$, $Re = 11\,300$), oblate ($\alpha < 1$, $H = 41.8\ cm$, $Re = 12\,900$) and close to spherical ($\alpha \simeq 1$, $H = 44.5\ cm$, $Re = 13\,300$). The scale bar is 2 mm long.

Liquid	ρ [g/cm^3]	μ [cP]	ν [cSt]	σ [dyne/cm]	n
Distilled water	0.996	1.004	1.008	72.1	1.333
Ethanol	0.789	1.19	1.51	23.2	1.363
Methanol	0.793	0.593	0.748	22.5	1.339

Table 4.1: Properties of the different liquids used in the pool. Here ρ is the liquid density; μ is the dynamics viscosity; ν is the kinematic viscosity, n the refractive index at $\lambda = 532$ nm, and σ the surface tension. The drop is always water.

As D is larger than the capillary length for water, $l_c = \sqrt{\sigma/(\rho g)} = 2.7$ mm, the water drop shows large oscillations that can affect the details of the impact dynamics (see Fig. 4.3(b)). The axisymmetric vertical oscillations of the drop can be estimated by the dominant mode (Rayleigh (1879), Lamb (1945, § 275)), giving a radius:

$$R(t,\theta) = R_0\left[1 + a\cos(\omega t + \phi)\, P_2(\cos\theta)\right], \tag{4.2}$$

where $P_2(x) = (3x^2 - 1)/2$ is the Legendre polynomial of degree 2, and θ is the polar angle in the spherical coordinate system. The aspect ratio between the vertical and horizontal diameters of the drop can thus be written:

$$\alpha = \frac{D_v}{D_h} = \frac{1 + a\cos(\omega t + \phi)}{1 - \frac{a}{2}\cos(\omega t + \phi)} \tag{4.3}$$

We determine a, ω and ϕ as fitting parameters: $a = 0.162$, $f = \omega/(2\pi) = 33.2$ Hz and $\phi = -132°$. The oscillation frequency is only 2% lower than the inviscid theoretical value $f_D = (4/\pi)\sqrt{\sigma/(\rho D^3)} = 33.9$ Hz. The typical time of bubble-ring entrapment, 50 μs, is only 0.17% of the oscillation period. Therefore the drop shape can be considered frozen during the entrapment.

This fitting is then used to get the aspect ratio from the falling height in the experiments. We have neglected viscous damping of the dominant mode in this estimate of drop oscillations. The characteristic time of this damping can be estimated as $\tau = D^2/(20\nu) = 1.08$ s (Lamb, 1945, § 355). In the overall falling time studied here ($\simeq 0.35$ s), viscous effects can be estimated to reduce the amplitude of the dominant mode by 27%. It is therefore too short to damp the oscillations significantly, as is observed in Fig. 4.4.

4.2.2 Numerical method

We use the open-source software Gerris (`http://gfs.sf.net`; Popinet (2003, 2009), Agbaglah et al. (2011)), using the *Volume-Of-Fluid* method, to perform

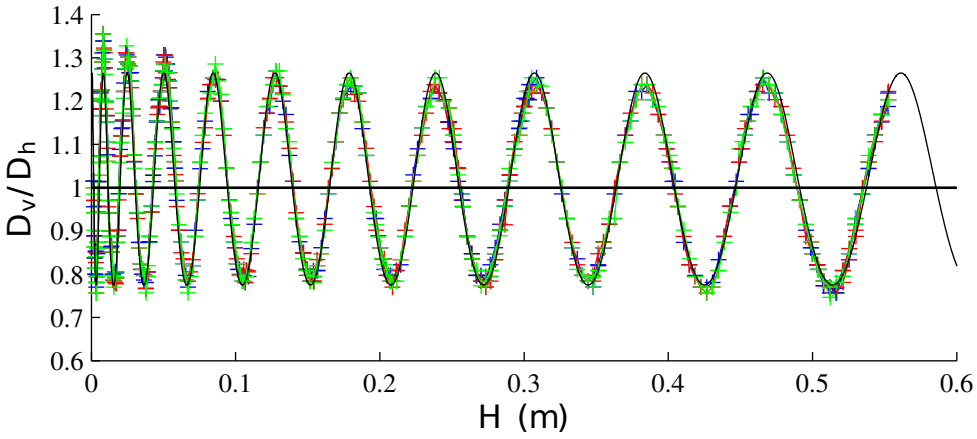

Figure 4.4: Drop aspect ratio $\alpha = D_v/D_h$ vs. H. The black oscillating line corresponds to the fitted equation (4.3).

axisymmetric simulations of the drop impacts. The liquid from the drop and the pool are identified with different markers (drop: red, pool: blue, air: light green). The adaptive mesh is refined dynamically based on the distance to the interface, vorticity magnitude and geometric conditions. The interface is refined uniformly at the maximum level in the simulations. The bubbles and droplets with area less than 10 cells are removed during the computation, as their dynamics cannot be captured accurately. The effects of this removal on mass conservation has been neglected. It represents an effective cut-off diameter of $D_{cut} = 3.57$ cells.

The simulations are started with the drop $0.1\,R$ above the pool, where $R = D/2$ is the drop radius. Non-dimensional time is defined as $t^* = t/\tau$, where $\tau = D/V$. The origin of time is taken when the undisturbed sphere would first contact the pool. The drop is kept at a constant effective diameter $D = 4.6$ mm. Air has a viscosity of $\mu_a = 1.81 \times 10^{-2}$ cP and density $\rho_a = 1.21$ kg/m^3. The liquid is water for both the drop and the pool, with viscosity $\mu = 1$ cP, density $\rho = 1000$ kg/m^3 and surface tension $\sigma = 72$ mN/m. Gravity is included as $g = 9.81$ m/s^2. We do not take into account the different properties of the bottom liquid in the simulation, and therefore do not include any Marangoni or variable-density effects between the two liquids. More details about the adaptive grid refinement can be found in

Popinet (2003) and Thoraval et al. (2012b).

4.3 Results and discussion

In what follows, we start by imaging water drops impacting onto water pools. For Reynolds number up to about 12 000, no bubble rings are entrapped, but unexpectedly we see an azimuthal undulation in the neck region, which breaks the axisymmetry. However, above this Reynolds number, a sequence of partial bubble rings are entrapped in the neck, which subsequently break into numerous micro-bubbles. These micro-bubbles display random sideways motions, suggesting underlying vortical structures.

Then we use water drops impacting on ethanol or methanol pools, which produces more regular bubble rings, and the difference in the index of refraction reveals intricate vortical tangles with both streamwise and azimuthal components.

We characterize the radial location where the first bubble rings are entrapped, as well as their radial spacing. We also show that the pool depth and drop shape at impact can alter the details, but not the qualitative dynamics of the bubble rings entrapment.

Finally, we observe experimentally the dynamics of the entrapment mechanism that was described in the numerical simulations of Thoraval et al. (2012b), as well as the three-dimensional effects that could not be captured by their axisymmetric simulations. Detailed images are presented, showing the rotation around the bubble rings, the splashing following ring entrapment, as well as the instabilities and entanglement of the vortices.

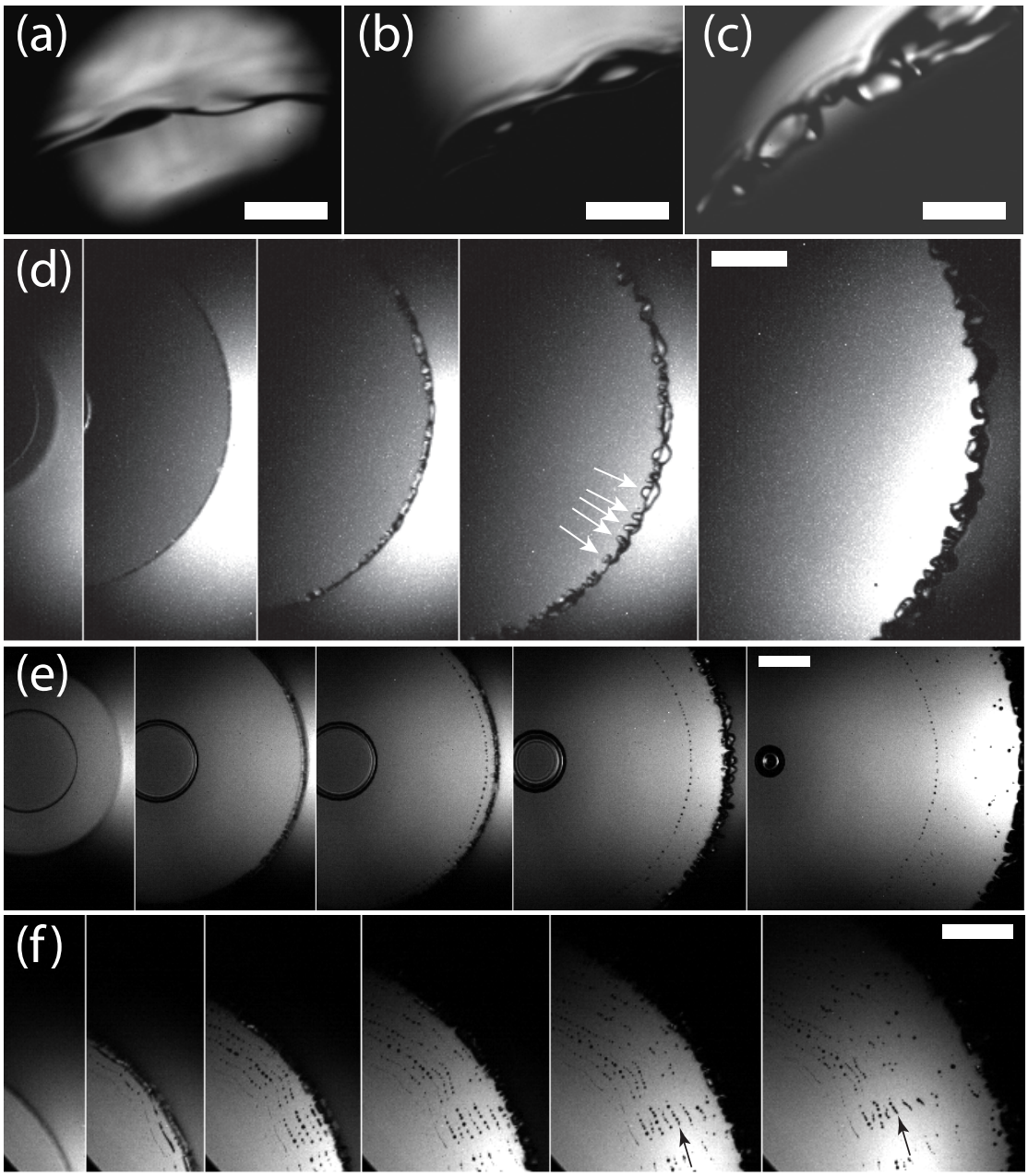

Figure 4.5: Early contact of a water drop impacting a δ = 250 μm deep layer of water, observed from below, as described in Fig. 4.2. (a-c) Neck between the drop and the pool. No bubble entrapment is observed at low impact velocities. An azimuthal instability develops on the ejecta, with a wavelength decreasing with increasing Re. (a) Re = 3 610, We = 39, K = 2 360, α = 0.94, (b) Re = 4 400, We = 58, K = 3 860, α = 1.17, (c) Re = 5 470, We = 90, K = 6 640, α = 0.86. (d) For an intermediate impact velocity, individual micro-bubbles can be entrapped. Frames are shown at 1, 13, 18, 25 & 46 μs after the first contact. Re = 11 400, We = 394, K = 42 100, α = 1.05. (e) For slightly higher impact velocity, the drop entraps one bubble ring and isolated bubbles, shown at t = 3, 11, 13, 21 & 40 μs. Re = 13 300, We = 535, K = 61 800, α = 0.98. (f) Multiple bubble rings. Frames are shown at about 5, 9, 13, 17, 21 and 32 μs after first contact. Re = 12 900, We = 506, K = 57 600, α = 0.80. The scale bars are all 200 μm long. See also supplemental videos.

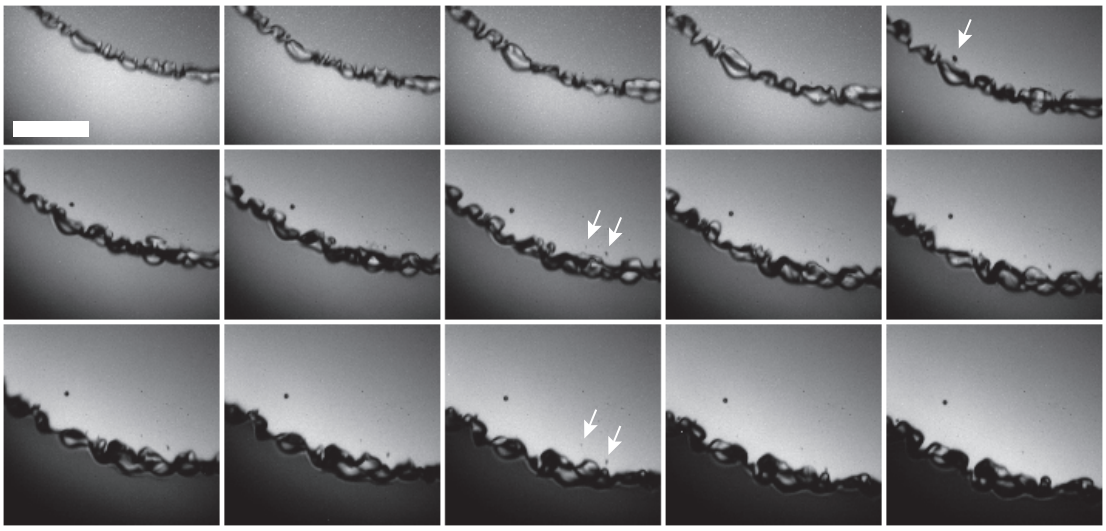

Figure 4.6: Details of individual micro-bubbles entrapments in the same conditions as in Fig. 4.5(d). Frames are shown 2 μs apart. The top row shows the dynamics leading to the entrapment of a $\simeq 10$ μm diameter bubble. On the second row, two smaller bubbles of diameter $\simeq 4$ and 6 μm are separating from the right part of the edge. While the first one stays behind the edge, and can be seen in the last frame, the second one is re-absorbed into the neck in the last row. The scale bar is 200 μm long. See supplemental video.

4.3.1 Isolated bubbles and multiple bubble rings for a water pool

We start by looking at the impact of the water drop onto a water layer. Figure 4.5 shows the early evolution of the outer neck contact of the drop with the pool. The contracting inner air disk is visible on the left side of the images in panels (d) and (e). Note that we are only looking at the early contact when the neck has not reached the size of the drop, as shown in the sketch in Fig. 4.2(b). The radius of the neck in the last panel of Fig. 4.5(d) has only reached 37% of the drop radius.

Figure 4.5 shows that even for low impact velocities the neck region between the drop and the pool does not remain smooth and axisymmetric, but develops azimuthal undulations. For the lowest impact velocities these undulations have long wavelengths and do not entrap bubbles, see Fig. 4.5(a-c). However, with

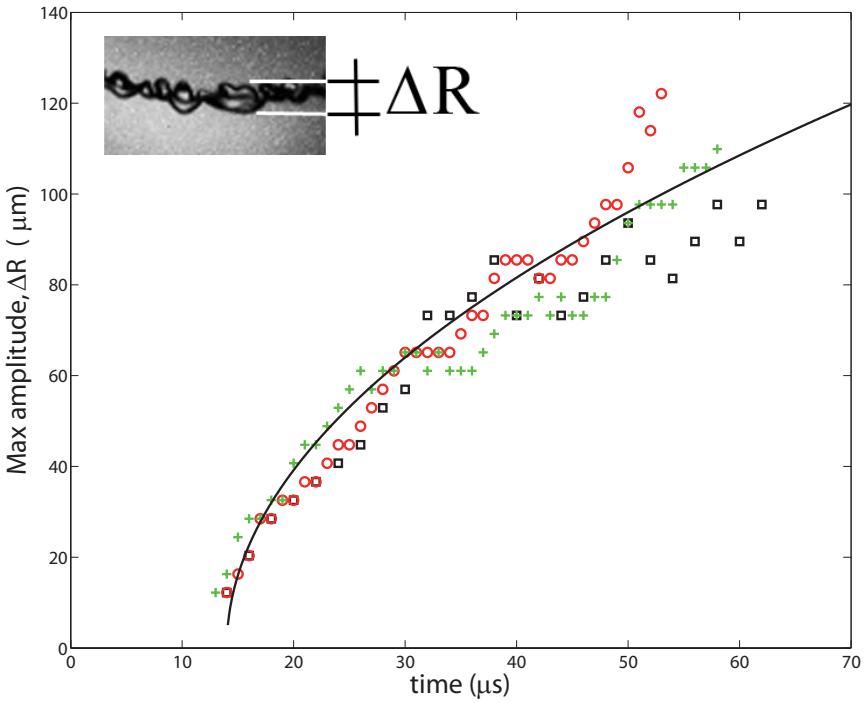

Figure 4.7: Maximum amplitude of the undulations of the front in the neck region, for water drop onto water pool. Data from three realizations, for the same conditions as Figs. 4.5(d) and 4.6. The solid line shows formula 4.4, with $C = 14$. The inset shows how the amplitude is measured.

increased impact velocity V the wavelength reduces and their amplitude grows more rapidly. In Fig. 4.5(d) these undulations appear first in the second panel and grow in amplitude during the radial motion, but individual bumps saturate and are often being pulled back by surface tension. The shapes are irregular, but we can glean a characteristic wavelength from the third panel in Fig. 4.5(d), giving $\lambda \sim 53$ μm, corresponding to 73 undulations around the periphery. These undulations appear when the ejecta emerges, pulling local sheets of air under the ejecta on both or alternating sides of it. These local sheets can be pulled along with the ejecta base, with only occasional bubbles entrained, when these small azimuthal air discs make contact across the thin air layer, as is shown in a longer sequence of frames in Fig. 4.6. Individual bubble entrapments can also occur in the troughs between the undulations.

In Fig. 4.7 we show the growth of the maximum undulation amplitude, mea-

sured between the troughs and peaks, see inset in the figure. The growth rate slows down with radial distance. For reference we fit a viscous-type length-scale,

$$L_\nu = C\sqrt{\nu(t-t_o)} \tag{4.4}$$

where $C = 14$ and t_o is the time of first observed undulations on the front. This suggests that the azimuthal wavelength is significantly longer than the thickness of the nascent ejecta, which should be of the order $\sqrt{\nu t}$, see Josserand and Zaleski (2003). Based on this undulation lengthscale ΔR, along with the neck velocity and water properties, the local $Re_{\Delta R} \sim 700$ and $We_{\Delta R} \sim 100$, suggesting inertia, viscous forces and surface tension all play a role in the dynamics.

Figure 4.6 shows that the characteristic azimuthal wavelength of the undulations also grows during the radial motion of the front, but this is more difficult to quantify.

It is curious that some air entrapment in breaking gravity waves has superficially similar appearance (Kiger and Duncan (2012), their Fig. 11), but is clearly driven by a different mechanism and is three orders of magnitude larger in size.

For slightly higher impact velocity, the entrapment of rather irregular bubble arcs begins. Figure 4.5(f) shows up to 10 such partial rings. The average radial spacing of the adjacent bubble rings is $\simeq 26$ μm. The air cylinders then break up into a row of bubbles through surface-tension driven Rayleigh instability. Bubbles are often shifted sideways in the azimuthal direction during the radial spreading (arrows in Fig. 4.5(f) and supplementary videos). For a stationary hollow cylinder of diameter d_b in an inviscid liquid, the most unstable wavelength is $\lambda_m = \pi d_b/0.484$. The characteristic time scale of the exponential growth $\sim exp(t/\tau_\sigma)$ of the breakup is given by $\tau_\sigma = 1.22\sqrt{\rho r_b^3/\sigma}$ (Chandrasekhar, 1981). The radii of the bubble arcs r_b for a water layer, in Fig. 4.5(f), are ~ 3 μm and they break up in about ~ 3 μs, which is $4\tau_\sigma$.

Thereby, the first bubble-rings entrapment for water occurs around $Re \simeq 12\,000$ and $K \simeq 50\,000$. These values are consistent with the numerical results of Thoraval et al. (2012b), where no bubble ring entrapment is observed for $Re = 10\,000$ and $K = 30\,000$, and a row of bubble rings is observed for $Re = 14\,500$ and $K = 74\,400$. In the former case, the ejecta sheet is thicker, because of the stronger surface tension effects on the ejecta sheet owing to the lower value of the splashing parameter K. It is re-absorbed on the drop or the pool during the oscillations, and no bubble ring entrapment is predicted. However, in the latter case, at higher K, the ejecta sheet is thinner, and its oscillations entrap a row of bubble rings at the core of vortex rings when it impacts onto and connects with the drop or the pool.

However, the comparison of Fig. 4.5(e) and (f) shows that more bubble rings can be observed at a slightly lower Re and K. This suggests that the Re number of the impact is not enough to characterize the bubble-rings entrapment. We will show in §4.3.4 the critical effect of the drop shape. Moreover, the azimuthal instabilities also affect the air entrapment, and individual bubble entrapments have been observed at slightly lower Re in Figs. 4.5(d) & 4.6.

Note that in the work of Castrejón-Pita et al. (2012), the vortex street is observed for conditions similar to Fig. 4(f) of Thoraval et al. (2012b), where no bubble-ring entrapment was predicted. Considering the large diameter of the drop they are using, it is not clear if the bubbles they observe are part of a bubble ring or isolated bubbles. They are also looking at a larger view and longer time evolution, that could be out of the field of view used in the current investigation (see perspective in Fig. 4.2). However, their alternating vortices are a new observation, clearly different from the isolated vortex rings produced by much lower impact velocities, see Peck and Sigurdson (1994).

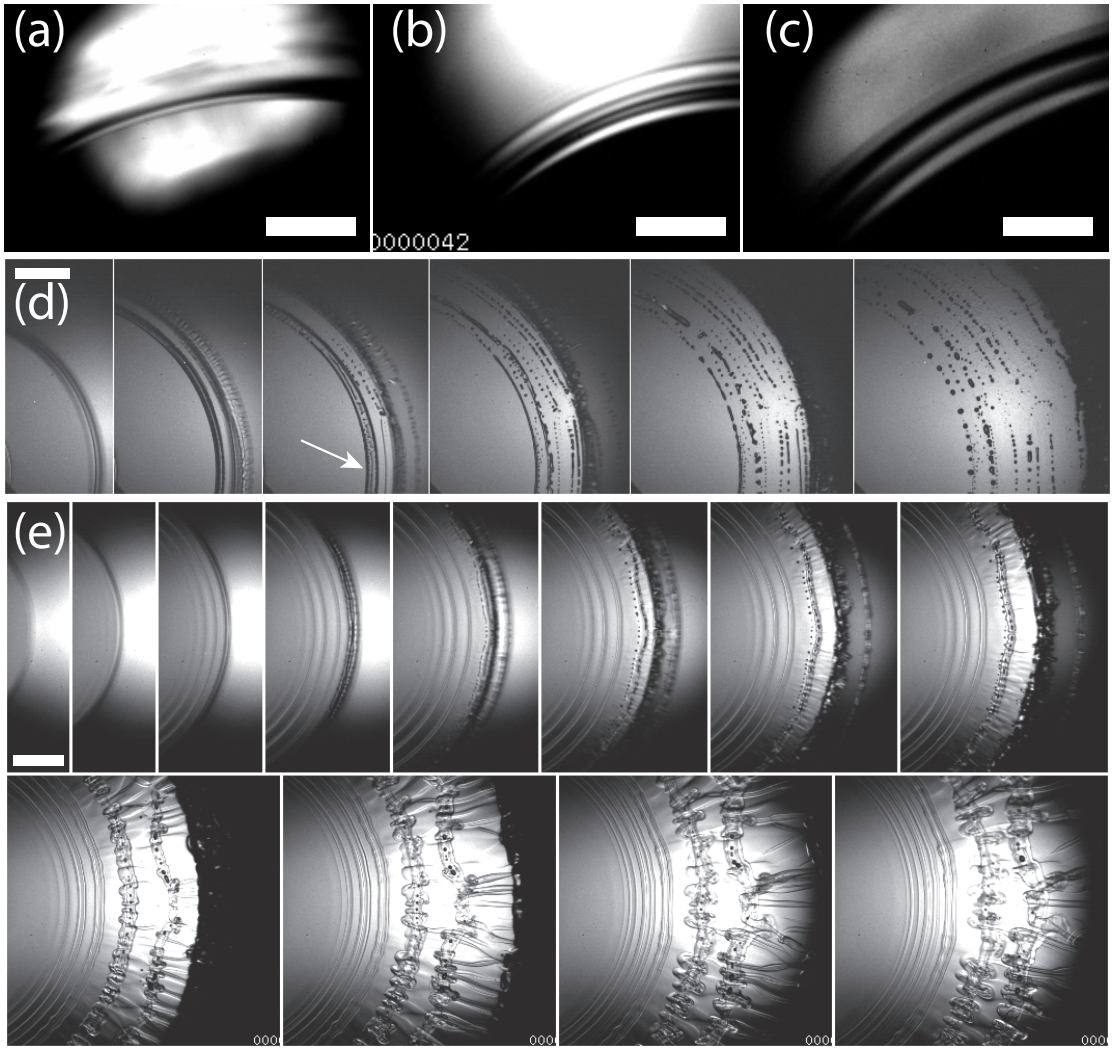

Figure 4.8: Early contact of a water drop impacting a pool of a miscible liquid (ethanol or methanol), observed from below, as described in Fig. 4.2. (a-c) Neck between the drop and the pool. No bubble entrapment is observed at low impact velocities on a thin film of ethanol ($\delta \simeq 250$ μm). Contrary to the water film, no azimuthal instability develops on the ejecta. (a) Re = 3 610, $\alpha = 0.94$, (b) Re = 4 400, $\alpha = 1.17$, (c) Re = 5 470, $\alpha = 0.86$. (d) Bubble rings for a water drop impacting onto a methanol layer (Re = 12 900, α = 0.80, δ = 50 μm). Frames are shown at 5, 9, 11, 15, 20 & 33 μs after first contact. (e) First oscillations of the ejecta sheet, followed by entrapment of bubble rings, for a film of ethanol (Re = 13 300, α = 0.98, δ = 250 μm). Azimuthal instabilities appear in the ejecta sheet, before its rim detaches in a liquid toroid. The first 8 frames are shown 4 μs apart, and then 20 μs. The scale bars are all 200 μm long. See supplemental videos.

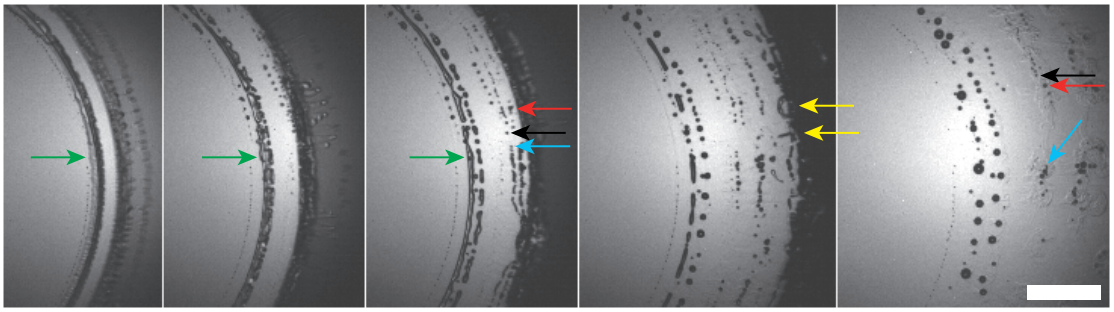

Figure 4.9: Early contact of a water drop impacting a pool of methanol, observed from below, as described in Fig. 4.2. Bubble entrapment dynamics for impact on a methanol film (Re = 12 900, α = 0.80, δ = 50 μm). The first frames shows the entrapment of a superposition of air sheets, later breaking in patches and then in micro-bubbles (green arrows). Three bubbles are identified in the third and last frames by red, black and blue arrows, showing their strong sideways motion. Bubble arcs with legs in the radial direction are identified by the yellow arrows. Frames are shown 3, 6, 15 and 60 μs after the first one. The scale bar is 200 μm long. See supplemental video.

4.3.2 Bubble rings for miscible liquids

The bubble ring entrapment becomes more regular for the impacts onto ethanol and methanol pools (Fig. 4.8 and 4.9), perhaps due to the lower surface tension of these liquids (Table 4.1). Contrary to the impacts onto water films, no azimuthal instability develops on the neck of the ejecta, which remains perfectly smooth in Fig. 4.8(a-c). At higher impact velocities bubble rings are entrapped. Figure 4.8(d) shows at least 10 bubble-rings. Many of them are entrapped axisymmetrically over the entire image view, which can span around 90^o angular sector.

In some instances thin ribbons of air are entrapped and subsequently break up into sub-rings and thereafter bubble rings, as highlighted by an arrow in Fig. 4.8(d). The frames in Fig. 4.9 detail this sequence of air entrapments. One air patch is identified by the green arrow in the second frame, superposed with another air sheet behind it. In the third frame, the air patch breaks into a bubble (identified by the green arrow), and a small air cylinder at a larger radial location, while the air sheet behind contracts into a cylinder. The vertical superposition of the air entrapments is clearly shown by the fact that the air bubble is observed

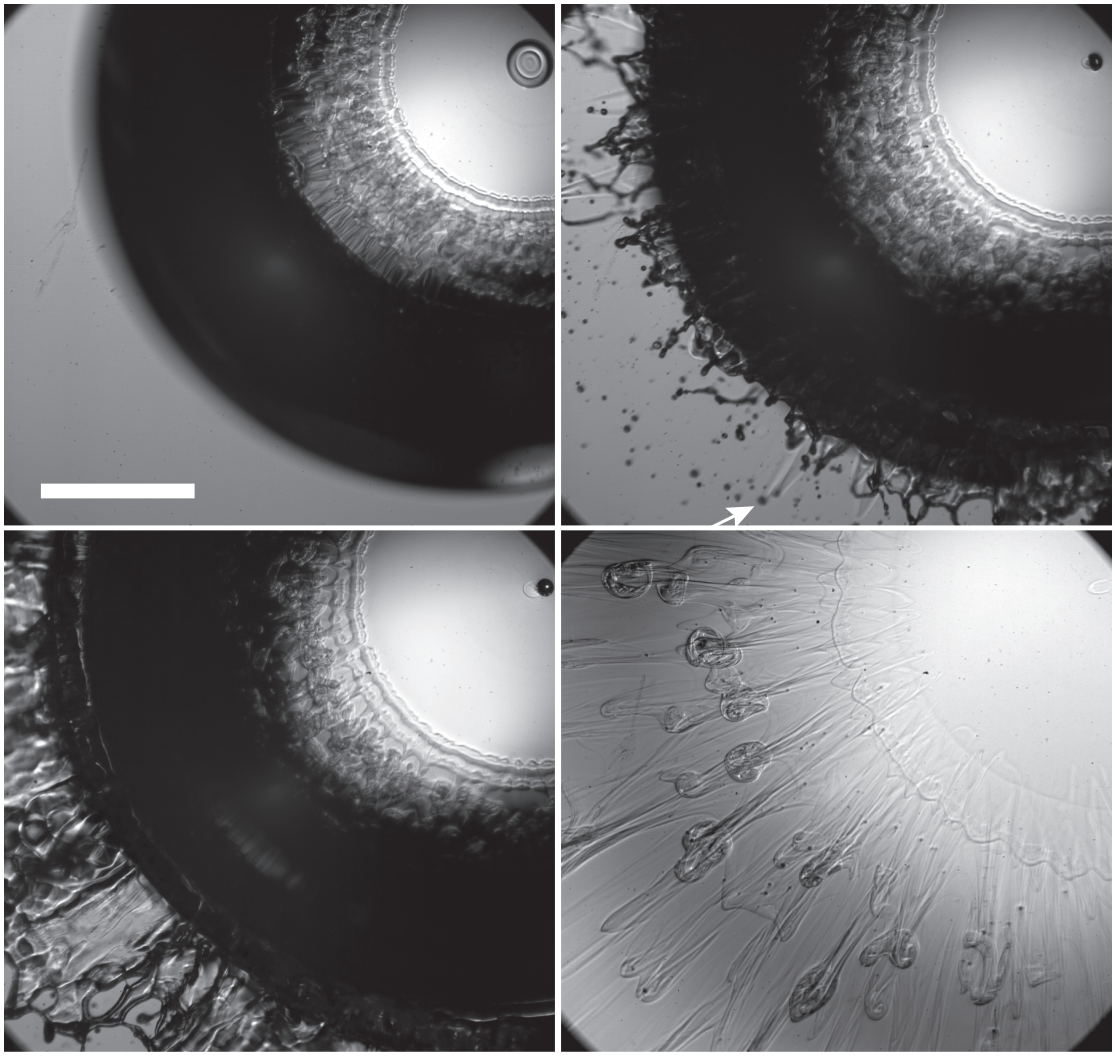

Figure 4.10: Larger view of a water drop impacting onto ethanol, at times $t \sim 50$, 150, 250 & 1150 μs after first contact ($Re = 14\,500$, $\alpha = 0.94$, $\delta \simeq 125$ μm). Frames taken from videos using Photron SA-5 at 10,000 fps, with a 1 μs exposure time. The arrow at the bottom of the second frame points at two splashed droplets planing on the surface, as shown by the capillary wedges left behind them. The central bubble has drifted out of the image in the last frame. The scale bar is 1 mm.

at the same radial location as the air cylinder. This supports the mechanism that air can be entrapped both above and below the ejecta sheet, as was shown in the numerical simulations of Thoraval et al. (2012b).

In a similar way as for water pools, Fig. 4.9 also demonstrates strong sideway motion of bubbles. Three bubbles are identified in the third frame by red, black and blue arrows. Their corresponding location is marked by the same colored arrows in the last frame. Comparison between the black and red arrows shows that this sideways motion can be of different strength for adjacent rings. This bubble motion in the azimuthal direction results in their clustering at isolated locations.

Figure 4.10 shows a wider view of an impact taken at a lower frame rate of 10,000 fps but larger pixel area of 896×848 px, using the Photron SA-5 CMOS camera. Each frame is frozen with a 1 μs exposure. The 100 μs interframe time only shows us snapshots of the phenomenon, putting the earlier figures in perspective, with most of the earlier sequences occurring before the first image. In the second frame multitude of splashed droplets appear from underneath the shadow of the drop, with some droplets planing on the pool surface, leaving behind narrow capillary wedges. The first panel shows a smooth central region, followed by a convoluted interface, suggesting the stirring by the three-dimensional vortical structures (see §4.3.7). Similar stirring can be inferred from the side shadowgraph imaging in Castrejón-Pita et al. (2012) (their Fig. 4). The final panel in Fig. 4.10 shows numerous isolated bubbles which have been redistributed by the vortical motions. The bubbles are mostly concentrated within the mushroom-like remnants of the vortical structures.

4.3.3 First onset, number and spacing of bubble rings

The first contact entraps a central air disk and forms a rapidly expanding outer liquid edge. Bubble rings are then formed as observed above. Figure 4.11(a) looks

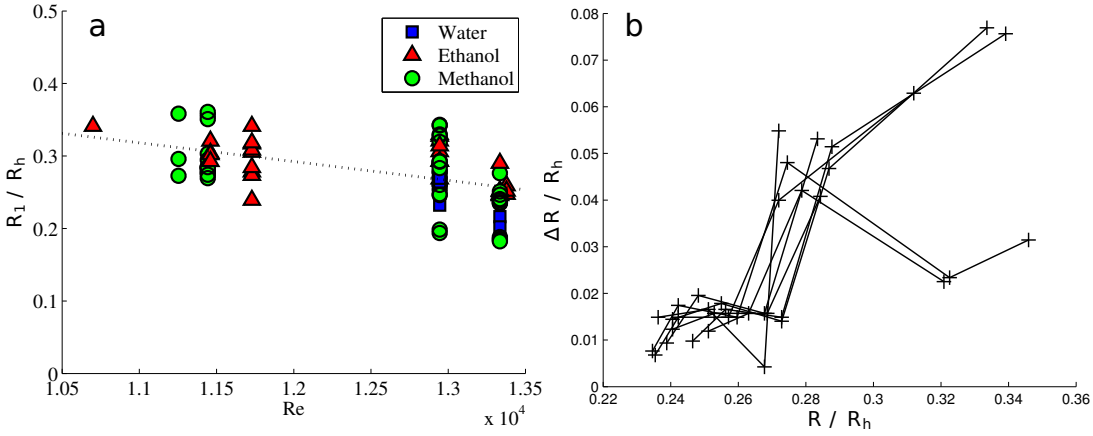

Figure 4.11: (a) First onset of bubble rings for water drop impacting onto a water, ethanol or methanol layer of different depths (see also Fig. 4.16). (b) Spacing of adjacent rings ΔR, vs radial distance R from the impact center. Data from 8 different realizations for a methanol pool (Re = 13 300, α = 0.98, δ = 250 μm).

at the radial location where the first bubble ring is entrapped. We normalize the radius of the first ring R_1 with the horizontal drop radius when it first contacts the pool, $R_h = D_h/2$. The data shows large spread, but an overall trend is for the onset to occur earlier for larger impact Re. The lowest entrapment radius is 0.18, similar to the 0.2 limit observed by Thoroddsen (2002) for the onset of the ejecta sheet. This onset radius of the ejecta is also in agreement with the inviscid numerics of Weiss and Yarin (1999).

Figure 4.11(b) shows the distance between the adjacent bubble rings measured for numerous identical impact conditions. The spacing of the rings tends to increase with distance and the entrapped bubbles become larger.

4.3.4 Effect of pool depth and drop shape

To ascertain the influence of the pool depth we systematically vary the layer thickness δ, from about 25 μm to 1 mm. Figure 4.12(a-c) compares the bubble rings for the 3 smallest pool depths δ. The ring structures are qualitatively similar in all cases, but the shallowest pool shows the earliest and finest bubble rings,

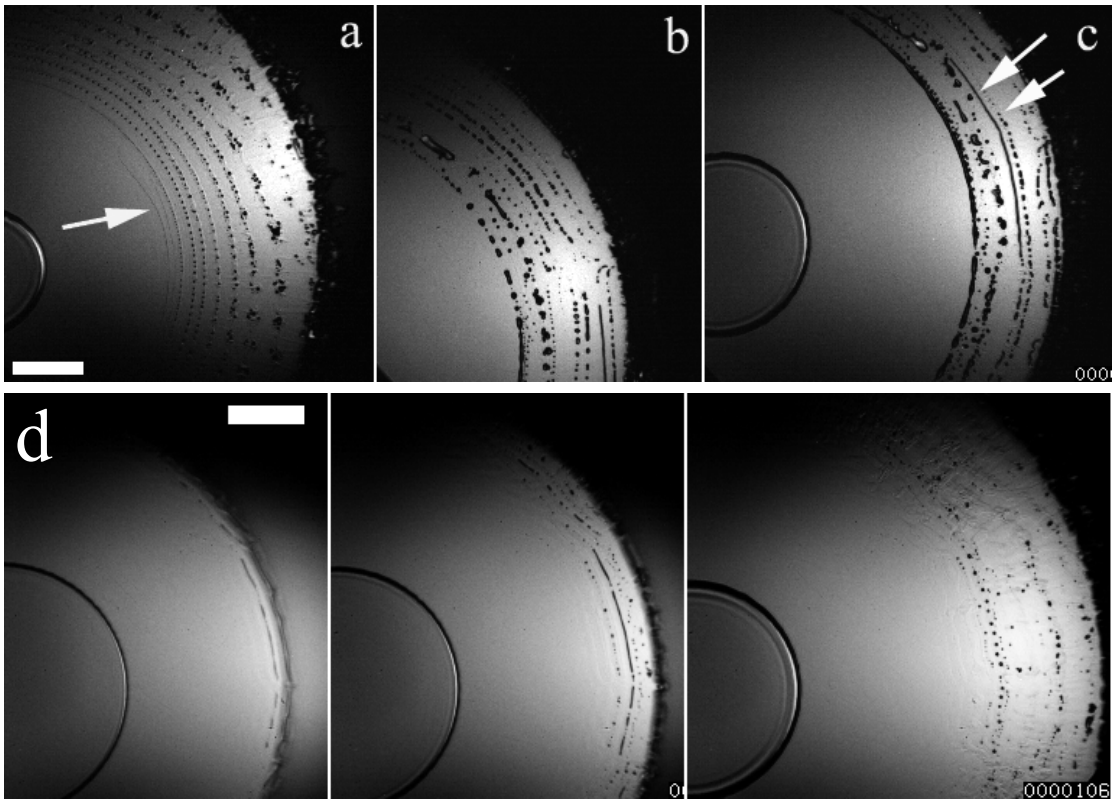

Figure 4.12: Effect of pool depth on the bubble rings for water drop impacting onto methanol, with $\delta \simeq 25$ (a), 50 (b) and 75 μm (c) ($Re = 12\,900$, $\alpha = 0.80$). The frames are all shown 24 μs after the first contact in (a-c). (d) Deeper methanol pool with $\delta \simeq 500$ μm. Frames shown at 10, 14 & 28 μs after first contact. The scale bars are 200 μm long. See also supplemental videos.

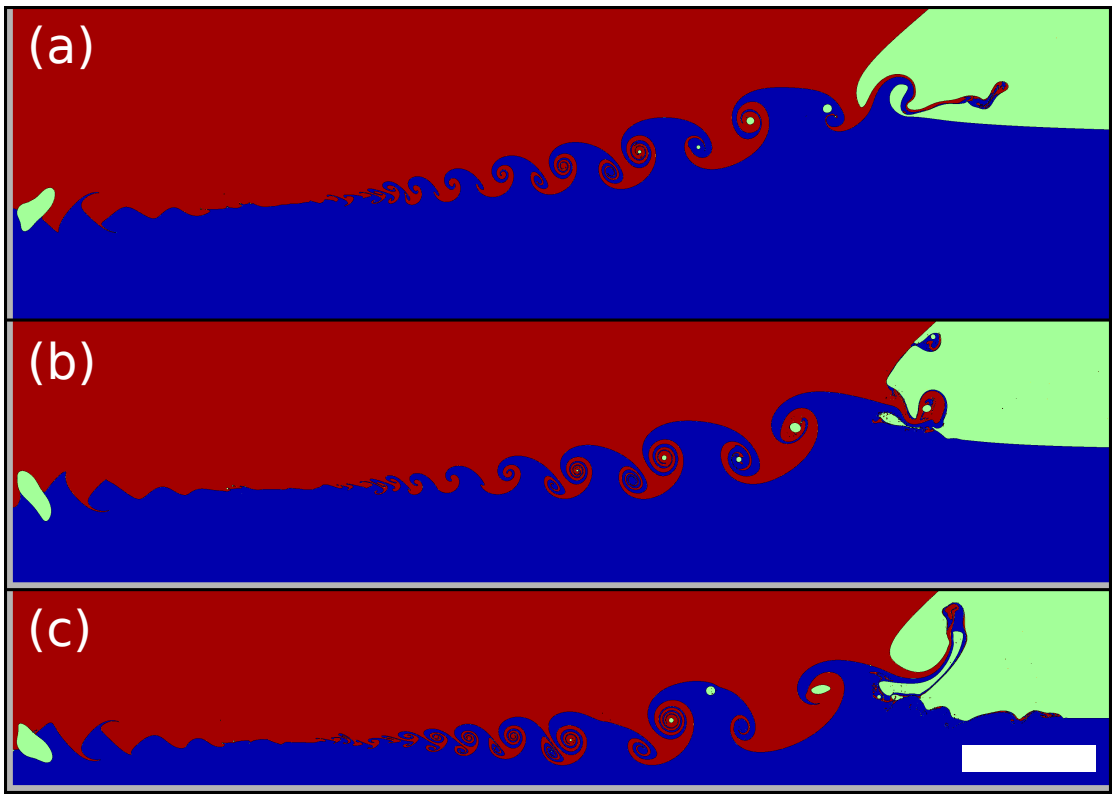

Figure 4.13: Effect of pool depth on the vortex street at $t^* = 0.0526$, for Re = 13 700. Pool depth $\delta = 800$ μm (a), 200 μm (b), 100 μm (c). The top of the 3 images are at the same location, relative to the original pool surface. The pool depth is larger than shown in the image in (a), but is completely included for (b) & (c), where the bottom is indicated in gray. The maximum and minimum level of refinement in the domain are respectively 12 500 and 778 cells per drop diameter and $D_{cut} = 1.3$ μm. The bar is 200 μm long. We can observe that one part of the ejecta sheet is climbing on the drop in (b), while the main ejecta sheet continues to emerge below. This is similar to what was observed numerically by Thoraval et al. (2012b) and experimentally by Zhang et al. (2012). The formation of this higher part of the ejecta sheet can be observed in the supplemental video. It then merges with the drop in this case. See supplemental videos.

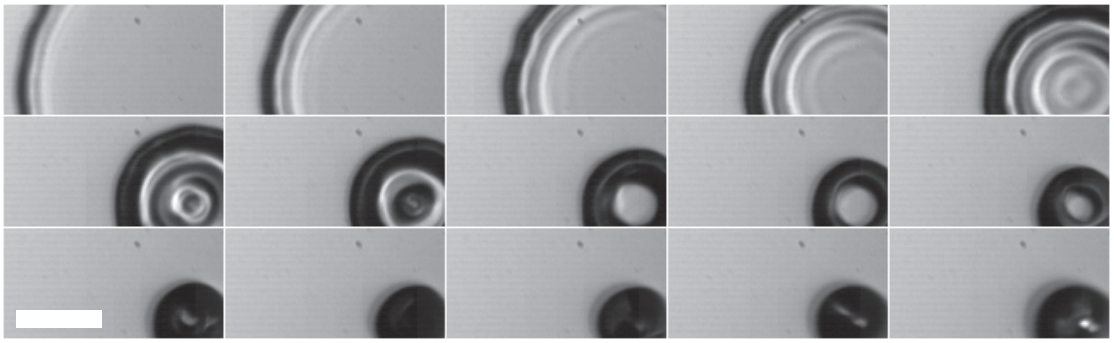

Figure 4.14: Contraction of the central air disk for a water drop impacting on a thin water film (Re = 11 600, α = 0.86, δ = 250 μm). The convergence of capillary waves punctures the center of the disk, producing an air toroid in the third frame of the second row, later contracting into a spherical bubble. Similar formation of a central air toroid can be observed in the supplemental video of Fig. 4.5(e), as well as in other water drop impacts on ethanol or methanol films. Frames are shown 7.1 μs apart, with an exposure time of 1 μs. See supplemental video.

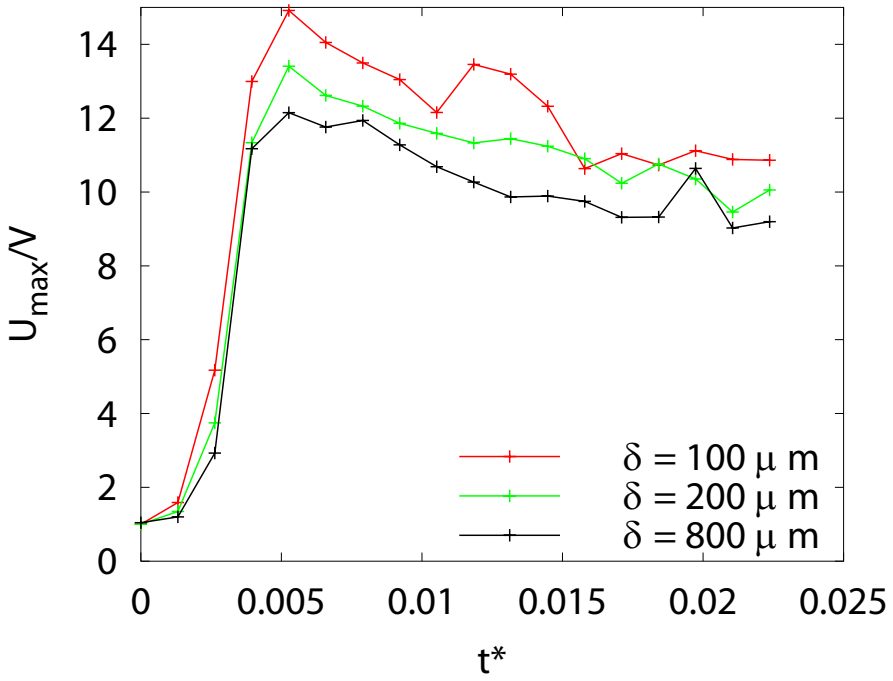

Figure 4.15: Maximum velocity U_{max} in the liquid from the numerical simulations of Fig. 4.13, for 3 different pool depths.

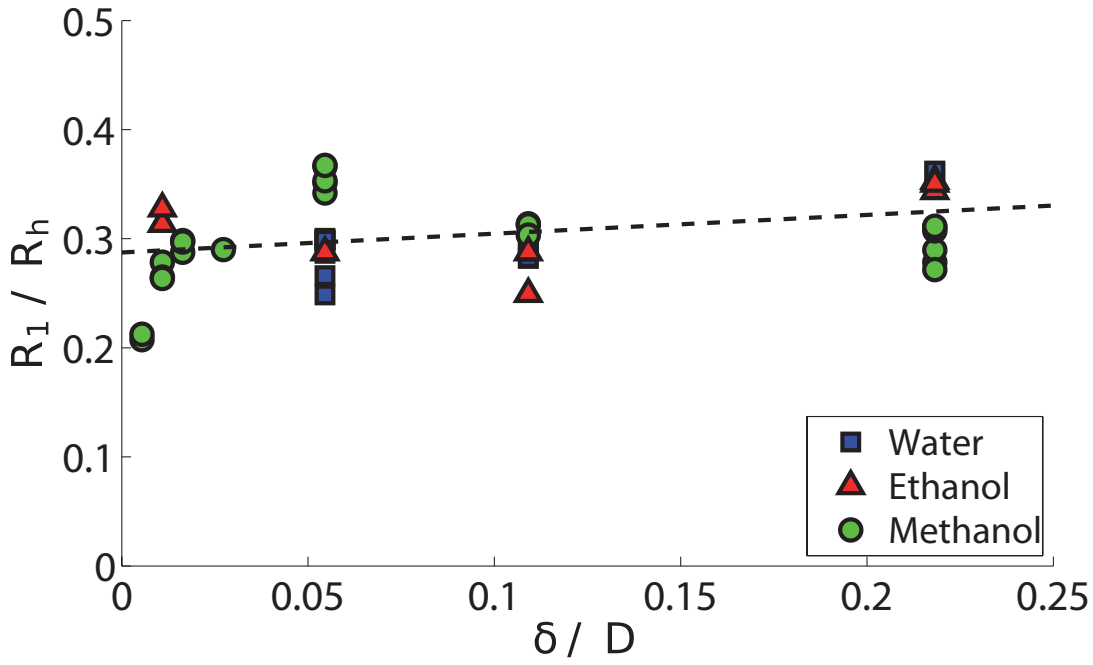

Figure 4.16: Experimental observation of the first bubble ring entrapment radius (Re = 12 900, α = 0.80) for different pool depths.

some of which are sub-pixel in diameter. The second ring in Fig. 4.12(a) allows us to measure the separation of micro-bubbles, giving λ = 8.8 μm, suggesting a diameter of the original air torus $d_{tor} \simeq$ 1.4 μm, and a bubble diameter of 2.9 μm. This is consistent with the smallest bubbles observed in Fig. 4.1(b) with a larger magnification. The earliest ring appears even smaller, arrow in Fig. 4.12(a). Figure 4.12(d) shows fewer but qualitatively similar ring entrapment, for much thicker layer.

Previous results of Thoraval et al. (2012b) suggested that the oscillations of the base of the ejecta sheet is responsible for the bubble rings entrapment, for a drop impacting a deep pool at high Re and K. Figure 4.13 shows numerical results for three different shallower pool depths. The two-liquid interface is highlighted by colouring the drop and pool differently. It shows that the same mechanism is also present for shallow pools, with only minor changes. However, the drop penetrates further into the pool for larger δ. The vortex street is therefore constrained

in a shallower region for shallower pools, and develops more horizontally. This constraining effect increases the maximum liquid velocity by as much as 20%, as shown in Fig. 4.15. The boundary layer developing on the glass plate could be important for the shallowest pools.

The first bubble ring is entrapped at R_1/R of respectively 0.37, 0.31 and 0.28 for pool depths $\delta = 800$, 200 and 100 μm respectively. This confirms the previous experimental observation of Fig. 4.12 that earlier rings are observed for shallower pools. Figure 4.16 also shows this experimentally in a more systematic way, but the difference is not very pronounced. Moreover, the smallest bubble ring observed in Fig. 4.13(c) has a diameter d_{tor} 1.5 μm (only 4 cells), very consistent with experimental observations of Fig. 4.12(a). The radial location of this first entrapment and its diameter are both consistent between experimental and numerical observations, even though the numerical simulations only consider one liquid.

In all three cases, we can see in the numerics that the central air disk punctures at the centre during its contraction into a central bubble, thus forming an air torus. This is also observed in some of the experiments, as seen in Fig. 4.14, where an air torus is formed, which later contracts into one bubble.

We observe experimentally that the most robust bubble rings are produced by a flat-bottom drop, as shown by the comparison of Fig. 4.5(e) & (f) and Fig. 4.8(d, e) and 4.9, with fewest bubble rings in 7(e), which is more spherical. The largest number of rings is also produced by such oblate drops (Fig. 4.5(f) and Fig. 4.24(b)). This is consistent with the numerical results of Fig. 4.17, showing a larger number of rings for the oblate drop. They even suggest that a prolate drop could completely suppress the bubble ring entrapments for the same effective diameter, as is shown in Fig. 4.17(a).

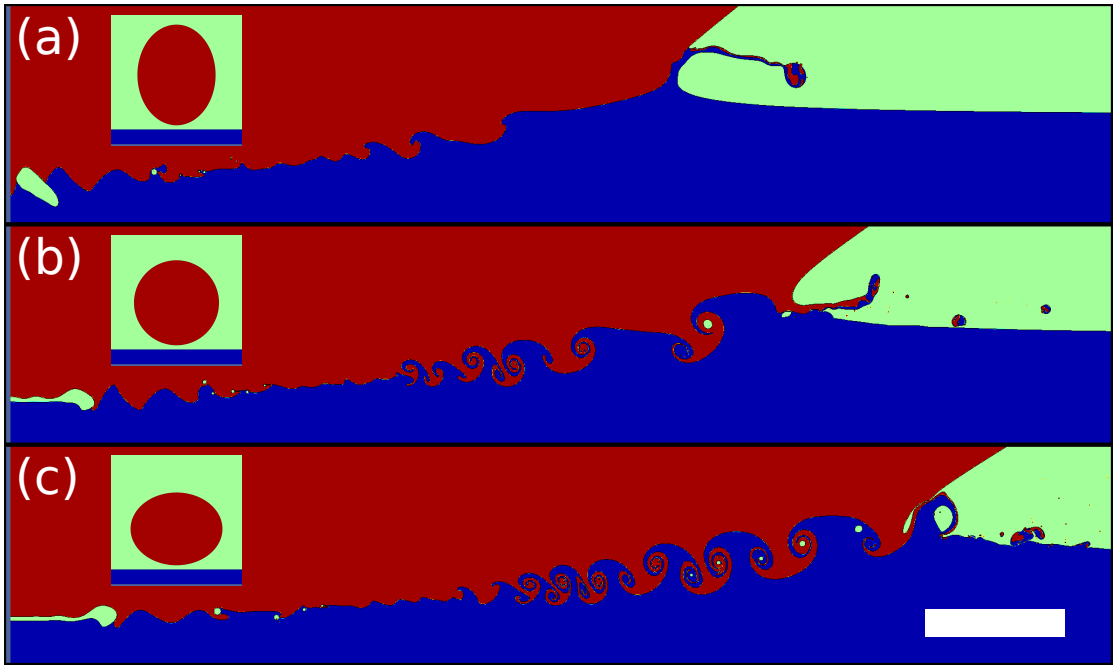

Figure 4.17: Effect of drop shape on the early dynamics at $t^* = 0.0406$, for $Re = 12\,900$ and $\delta = 800$ μm. The drop is modeled as an ellipsoid of revolution, where α is (a) 1.29, (b) 1, (c) 0.79. (a) and (c) correspond to the maximum horizontal deformations of the fitting equation (4.3), with $a = 0.162$, keeping the same effective diameter. The maximum and minimum level of refinement in the domain are respectively 5240 and 655 cells per drop diameter, and $D_{cut} = 3.1$ μm. The scale bar is 200 μm long. See supplemental videos.

4.3.5 Edge breakup and splashing

Numerical simulations have shown that the ejecta sheet can impact alternatively on the drop and the pool during the vortex shedding. The tip of the ejecta can thus detach into a liquid torus exiting the neck region at high speed (Thoraval et al., 2012b). Such tori are highly unstable to Rayleigh instability and break rapidly into splashed micro-droplets of similar sizes. However, this earliest splashing of micro-droplets by axisymmetric breakup of the ejecta sheet had not been observed previously in experiments.

By looking carefully at Fig. 4.8(d, e), 4.9 & 4.10, we can identify this early splashing by the breakup of the tip of the ejecta sheet after the entrapment of a few bubble rings, as was suggested by the numerical simulations. The liquid toroid in Fig. 4.8(e) separates at $t^* \simeq 25$ μs after the first contact, and a velocity of 20.5 m/s, which corresponds to 7.1 times the impact velocity. The tip velocity of the ejecta sheet in the numerical simulations at the same non-dimensional time, is 6.2 for $Re = 12\,900$ (Fig. 4.17(b)), and 7.4 for $Re = 13\,700$ (Fig. 4.13(b)), which is in excellent agreement with the experimental observations.

Figure 4.18 shows more detail of the breakup of the edge at a slightly lower Re. The ejecta sheet breaks via holes puncturing behind the rim. The thicker ejecta rim is therefore left connected to the neck by liquid tendrils, but subsequently becomes fully detached.

To remove the ambiguity of the bottom view, we have also looked at this early splashing from the side above the free surface. Figure 4.19(a) confirms the bottom view images, showing the ejecta sheet emerging from the neck, puncturing behind the rim and separating a liquid toroid from the neck. Liquid tendril are also observed in the fourth frame, and are slingshot ahead of the rim, creating the protrusions observed in the last frame, similar to the last frame of the first row of Fig. 4.8(e). The slingshot of the broken ejecta sheet can also be observed in numerical simulation, as in supplemental video of Fig. 4.17(a), and is similar to

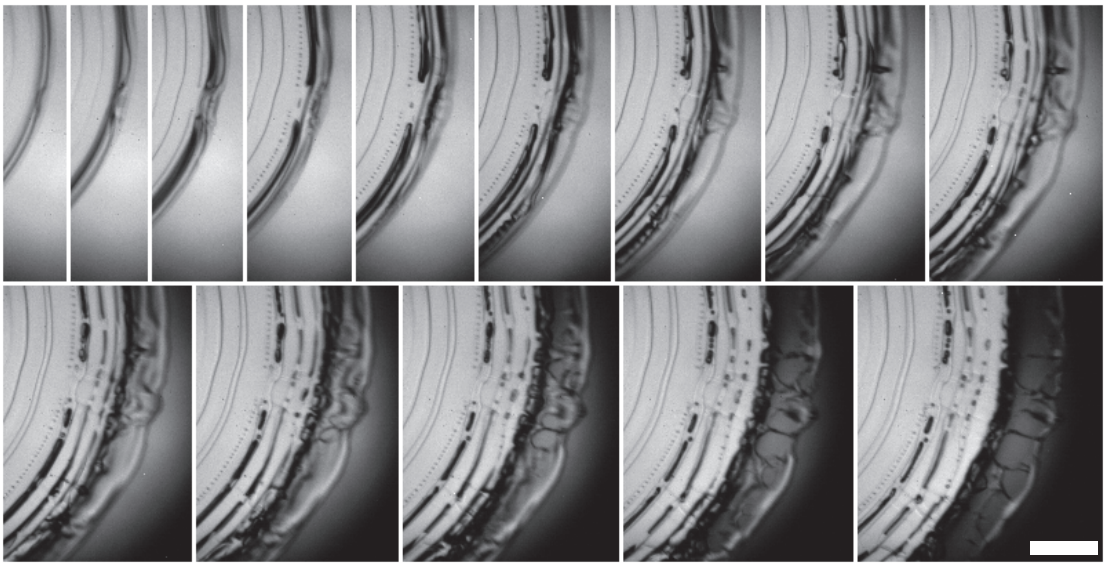

Figure 4.18: Details of the ejecta sheet breakup, for a water drop impacting a thin film of ethanol (Re = 11 700, α = 0.79, δ = 75 μm). The ejecta sheet starts to puncture on the second frame of the second row. The growth of the holes leave tendrils connecting the neck to the liquid rim. The scale bar is 200 μm long. Frames are shown 2 μs apart. See supplemental video.

the slingshot mechanism described in Thoroddsen et al. (2011).

Two consecutive liquid rings are observed in Fig. 4.19(b). It also shows the emergence of a greatly disturbed ejecta sheet after this early splashing. A larger bottom view confirms this side view observations in Fig. 4.19(c). This mechanism, of a detachment of a thin torus of liquid, explains the synchronized emergence of uniform sized micro-droplets observed ahead of the main irregular ejecta sheet, see Fig. 4.19(d) as well as Fig. 2(c) in Thoroddsen (2002). The irregular sheet is clearly shown in Fig. 4.10.

The splashing of several liquid tori is consistent with numerical simulations showing that the ejecta sheet can breakup during the successive impacts on the drop and the pool. Supplemental video of Fig. 4.17(a) shows such a case where the ejecta sheet breaks first by climbing on the drop and then impacting on the pool, thus creating two consecutive liquid tori.

After the first ring entrapment, regular spanwise instabilities can appear in

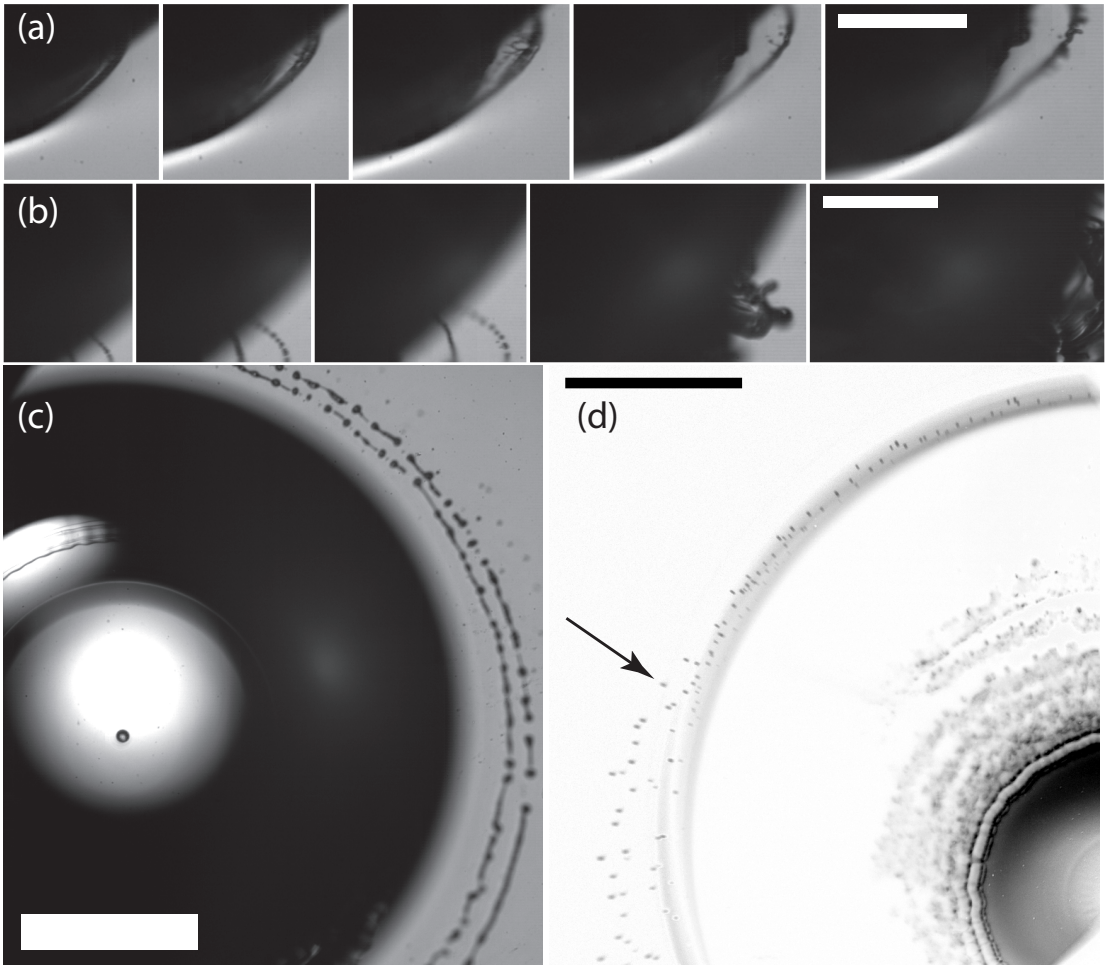

Figure 4.19: Detachment of liquid toroids by breakup of the ejecta sheet. Scale bars are 500 μm for (a,b) and 1 mm for (c,d). All images have an exposure time of 1 μs. (a) Side view of the liquid toroid detachment for a thin film of ethanol (Re = 12 600, α = 1.11, δ = 125 μm). The ejecta sheet punctures in the third frame, breaking into tendrils. Those tendrils are slingshot in front of the liquid rim which has not yet broken, as observed in the last frame. The frames are shown 10 μs apart. (b) Side view of two liquid toroid detachments for a thin film of methanol (Re = 12 600, α = 1.11, δ = 125 μm). The frames are shown 10 μs apart for the first 3 frames, and then 80 μs. The splashing of liquid toroids is followed by the emergence of an irregular ejecta sheet, as can be seen also on the larger bottom view of Fig. 4.10. (c) Larger bottom view of two consecutive rings of liquid droplets and toroidal sections detaching for an ethanol pool (Re = 11 600, α = 0.86, δ = 125 μm). (d) First droplets emerging from underneath the drop in the same conditions as Fig. 4.10. Image difference between two adjacent frames, to highlight the splashing droplets. Shown in inverted gray-scale. The exposure is 1 μs long.

the ejecta sheet, as is clearly seen in the second panel of Fig. 4.8(d), as well as Fig. 4.8(e) & 4.9. The fine azimuthal breakup when the ejecta bends and impacts onto a pool have been reported by Thoroddsen et al. (2011) (their Fig. 5) and may be of similar origin. Furthermore, the early appearance of similar azimuthal instabilities have also been observed by Thoroddsen et al. (2012b) in a free-surface cusp, which is formed during a drop impacting onto a solid surface. Numerical simulations show that the ejecta sheet breaks when it impacts on the drop or the pool, by stretching between the new connection and the faster rim. This instability is therefore consistent with the impact of the ejecta sheet on the drop or the pool. Similar breakup of a liquid sheet by stretching was also observed experimentally by Roisman et al. (2007) for spray impacts.

4.3.6 Vortex shedding and rotation around bubble rings

The difference in refractive index between the drop and the pool (see Table 4.1) allows us to visualize vorticity structures inside the liquid. As the coherent vortices bend and wrap up the interface between the two liquids, a dark line can be observed at their edges with our back-light imaging setup.

Numerical simulations have shown that the first oscillations of the base of the ejecta sheet have a smaller amplitude and do not entrap any bubble rings, see Thoraval et al. (2012b) (their Fig. 4(c,f,g)) and our Figs. 4.13 & 4.17. This is consistent with our experimental observations of Figs. 4.8(e), 4.18, 4.22(a) & 4.24, where dark arcs form before the first bubble rings. They show the shedding of vortices from the neck before the start of the bubble-ring entrapment.

As the neck moves outwards radially, the angle between the pool and the drop becomes larger, and bubble rings are entrapped, as observed above. Numerical simulations have shown that these rings are often entrapped in an alternating way at the top and the bottom of the ejecta sheet. At the same time, they shed vortices of alternating sign in the liquid. Bubble rings are therefore entrapped at the core

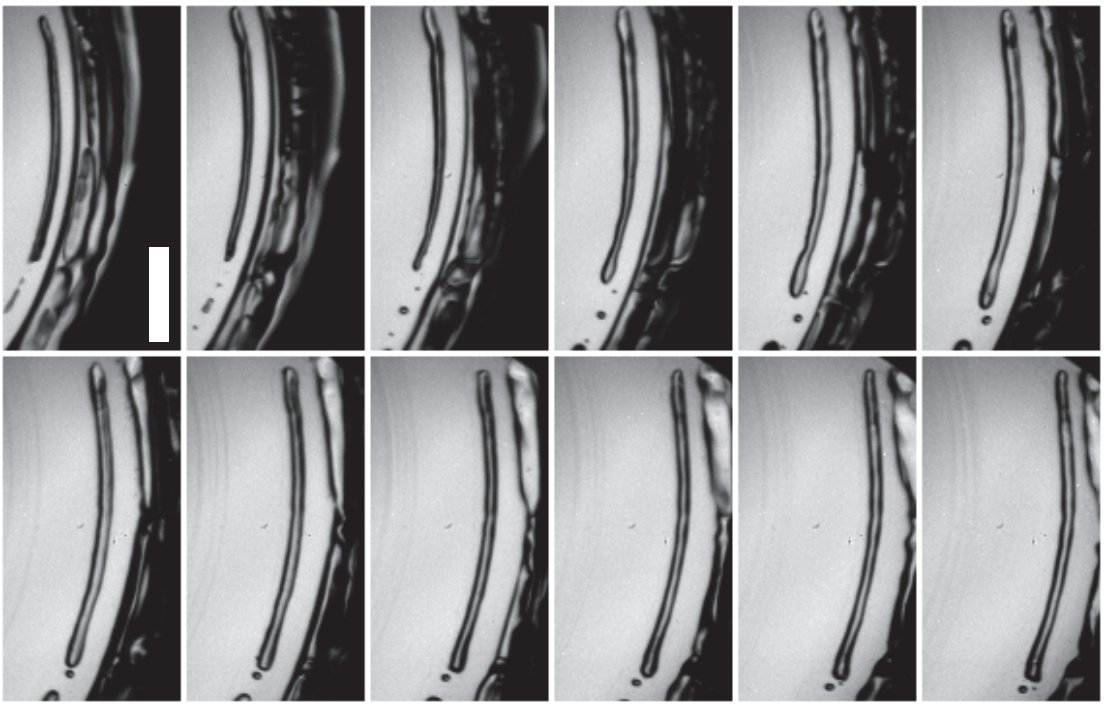

Figure 4.20: Entrapment of a large air cylinder for a water drop impacting a thin film of methanol (Re = 11 400, α = 1.05, δ = 50 μm). The small bubble at the bottom right of the long cylinder make a complete rotation around the cylinder between frames 4 and 12. The frames are shown 4 μs apart. The scale bar is 200 μm long. See supplemental video.

of vortex rings. Dark lines are indeed observed experimentally around the bubbles, supporting this shedding of vorticity scenario. The rotation is also made apparent by the dynamics of a micro-bubble rotating around a larger bubble cylinder in Fig. 4.20. We can obtain an estimate of the rotation speed in the vortex rings by tracking a 2 μm particle seeded into the pool liquid (Fig. 4.21), giving a rotation period of 18 μs in this example.

The dynamics of the air entrapped in this vortex street is also affected by the rotation around it. One can expect the rotation to delay the capillary breakup of the air cylinders (Rosenthal, 1962, Ashmore and Stone, 2004, Eggers and Villermaux, 2008). This is indeed evident in Fig. 4.20, where the cylinder of diameter about 29 μm can be observed for more than 94 μs before breaking, corresponding to $t/\tau_\sigma \simeq 7$ based on the methanol properties. The air cylinder also elongates by about 25% between the first and the last frame, consistent with the theory that it resides inside a vortex. The relative motion of the bottom tip of the air cylinder and the closest micro-bubble below shows that the stretching due to the radial motion cannot account for this elongation. Even smaller cylinders can be stabilized, as observed in Fig. 4.12(c). Two air tori are formed next to each other, with similar diameters $d_{tor} \simeq 8\,\mu$m (see arrows in the figure), but break up at very different times from formation, of $t/\tau_\sigma \simeq 4$ and 12, based on the liquid properties of the methanol. These delayed breakups show the strong stabilization effect of the circulation around these air tubes. The breakup wavelength is also larger, as the theory suggests (Ashmore and Stone, 2004).

The row of vortices shed in the liquid can also interact with adjacent ones. In some realizations two closely entrapped air tori rotate around each other, with the line of small bubbles rotating around the bigger one. Figure 4.22(b) shows such a sequence, where we track one rotation, which takes $T = 104$ μs. Numerical simulations show that vortices of different strength are created at the top and bottom of the ejecta sheet (Thoraval et al., 2012b). The longer time evolution

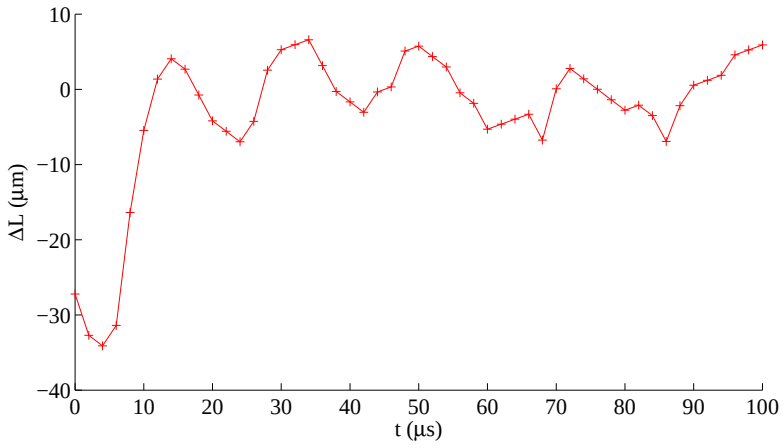

Figure 4.21: Tracking of a 2 μm particle rotating around a vortex core for a drop impacting on a pool of ethanol (Re = 11 400, α = 1.05, δ = 125 μm). ΔL is the distance to the initial positions, minus the mean radial translation component identified by a linear regression. The period of rotation is here about 18 μs.

shows that this difference can make the bubble rings rotate around each other while translating (Fig. 4.22(c) and supplementary videos). These dynamics are consistent with the experimental observation of the rotation around bubble rings.

Some of the bubble tracks simply translate past each other during their radial motions, for example visible in the videos accompanying Figs. 4.22 & 4.24. The bubbles are initially sitting at slightly different depths, and this difference in vertical location is amplified by the vorticity, as shown above. Moreover, as the bubble tori break into bubbles, their vertical width will slightly increase, sampling larger mean shear. These relative translations of bubbles could therefore result from a vertical mean gradient of horizontal velocity within the pool depth.

4.3.7 Three-dimensional instabilities

The axisymmetry of the impact is rapidly broken by different instabilities (see Figs. 4.5, 4.8 & 4.9). For a water pool, we have observed that undulations develop in the neck as soon as an ejecta forms (Fig. 4.5). This leads to entrapment of isolated bubbles (Fig. 4.5 & 4.6) and creates less regular bubble rings compared

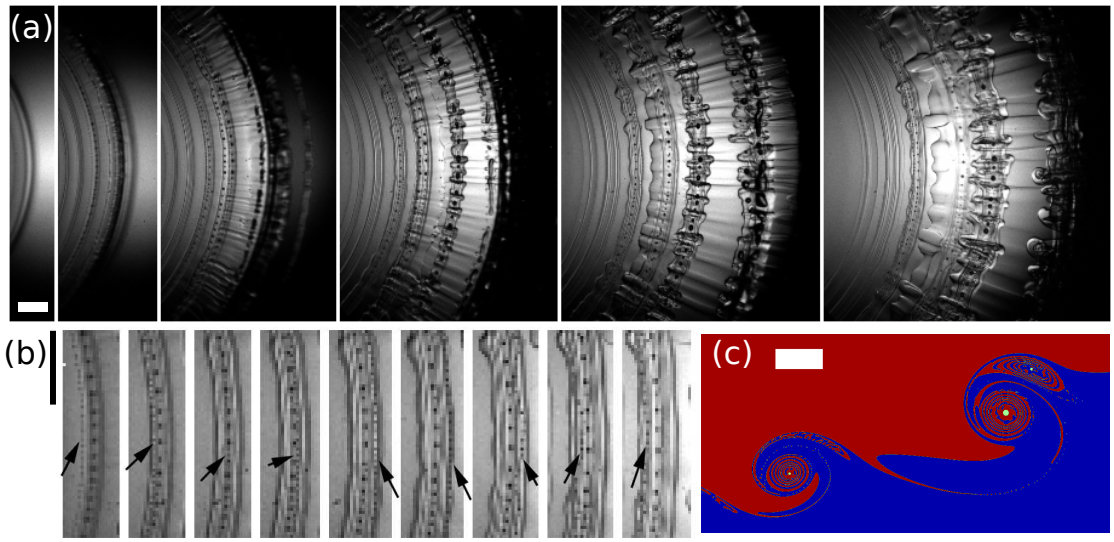

Figure 4.22: (a) Bubble rings formed during the impact of a water drop onto a shallow pool of ethanol (Re = 13 300, α = 0.98, δ = 250 μm). The frames are shown at 8, 20, 38, 66 & 112 μs after the first one, showing a total of 7 bubble rings. (b) Close-up view of a line of fine bubbles which circulate around another line of slightly larger bubbles, from the video in (a). Total duration of these frames is 104 μs. See also supplemental videos. (c) Numerical simulations of a water drop impacting on a thin film of the same liquid (Re = 13 800, α = 1, δ = 800 μm). This focused view of the interface at t* = 0.481 shows the rotation of a pair of bubble tori at the core of adjacent vortex rings. The scale bars are all 100 μm long. See supplemental videos.

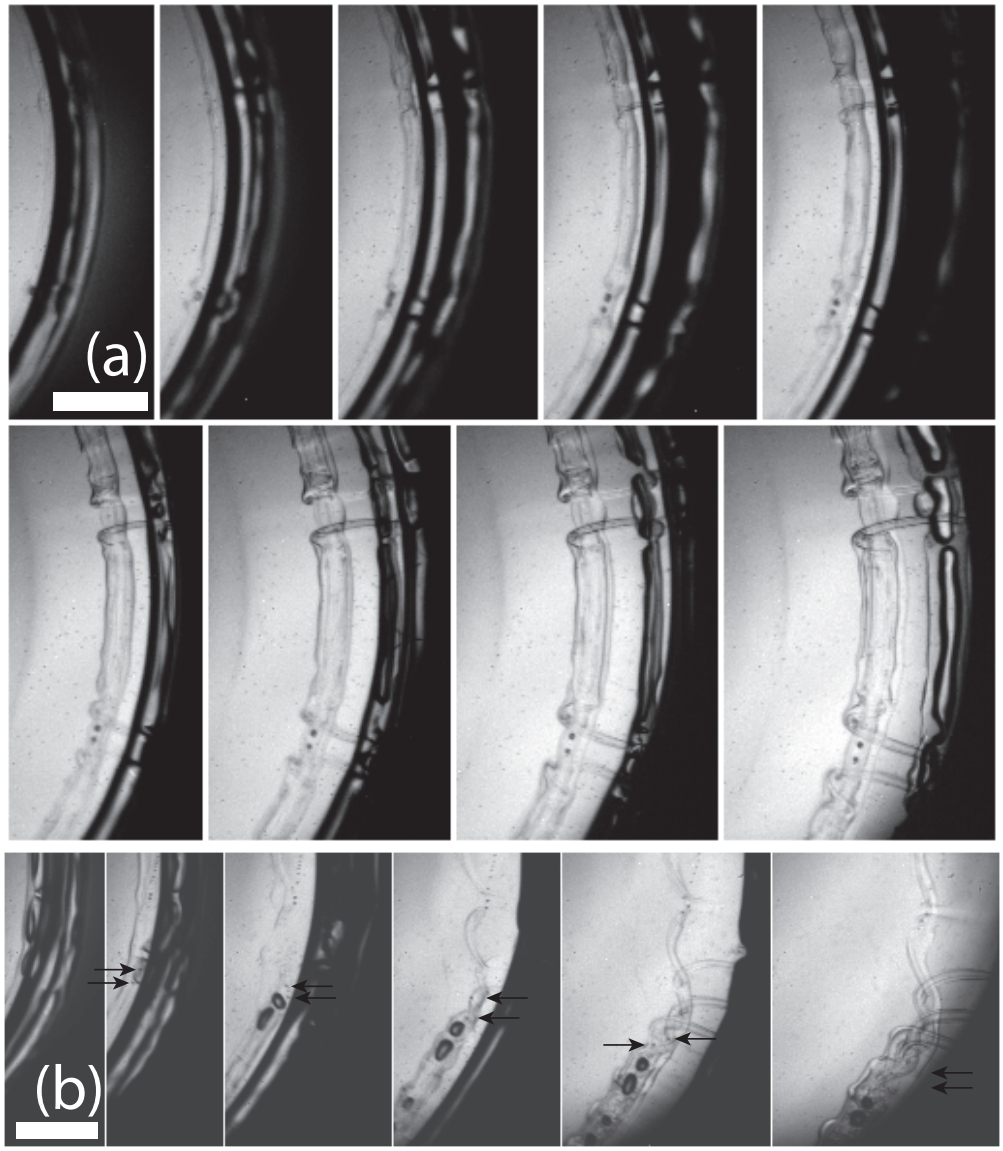

Figure 4.23: (a) Roll-up of isolated streamwise vortex pairs for a water drop impacting a film of ethanol seeded with 2 μm particles (Re = 11 400, α = 1.05, δ = 125 μm). The first images show that the vortex pairs are starting at the same azimuthal location as local disturbances in the front. The bottom vortex pair first entraps a bubble, later splitting in two. Frames are shown 3, 6, 9, 12, 17, 23, 27, 35 μs after the first one. (b) Roll-up and sideways motion of streamwise vortices for a water drop impacting a film of ethanol seeded with 2 μm particles (Re = 11 400, α = 1.05, δ = 125 μm). Frames are shown 3, 10, 18, 32 & 47 μs after the first one. The scale bars are 200 μm long. See supplemental videos.

to ethanol or methanol pools. Even in those lower surface tension liquids, the most regular rings appear at smaller entrapment radii, where the ejecta sheet has not broken yet and remains axisymmetric. After the breakup of the ejecta sheet, the loss of axisymmetry is imprinted on the bubble entrapments, as shown by the bubble arcs observed in Fig. 4.9, with legs extending in the radial direction towards the neck.

We have already suggested in §4.3.5 that some of the azimuthal instabilities come from the breakup of the ejecta sheet, when it bends and touches the drop or pool surfaces. Overturning gravity waves also rebound and destabilize underlying vortices, but at a much larger scale than herein, see Watanabe et al. (2005). Figure 4.18 clearly demonstrates the effect of isolated neck disturbances on the bubble entrapment. A small perturbation is visible in the first frame and develops in time. The two first bubble rings which form in the following frames are broken at the same azimuthal location and the ejecta ruptures there first.

Three-dimensional instabilities also develop inside the liquid, and are made apparent by the difference in refractive index. Radial lines are visible in Figs. 4.8(e), 4.10, 4.22(a), 4.23 & 4.24. They show the formation of streamwise vortices between the primary spanwise vortex rings, which often reach to the free surface in the neck. For the lower Re cases (Figs. 4.23), isolated streamwise vortices are observed. In Fig. 4.23(a), they appear in pairs, at the same location as a front perturbation. The lower one in the image starts at an isolated location on the side of a vortex ring, where it entraps one micro-bubble. Two lines are then visible on each side of this initial entrapment and extend up to the front. This suggests that the vortex pair arises from the same vortex loop, rolling-up around the vortex ring. The connection between the two streamwise vortex lines should then form a vortex loop with one section in the azimuthal direction, near its origin around the bubble. The presence of a strong vorticity around this bubble is demonstrated by its breakup into two smaller bubbles (in the 4th panel of Fig. 4.23(a)). Moreover,

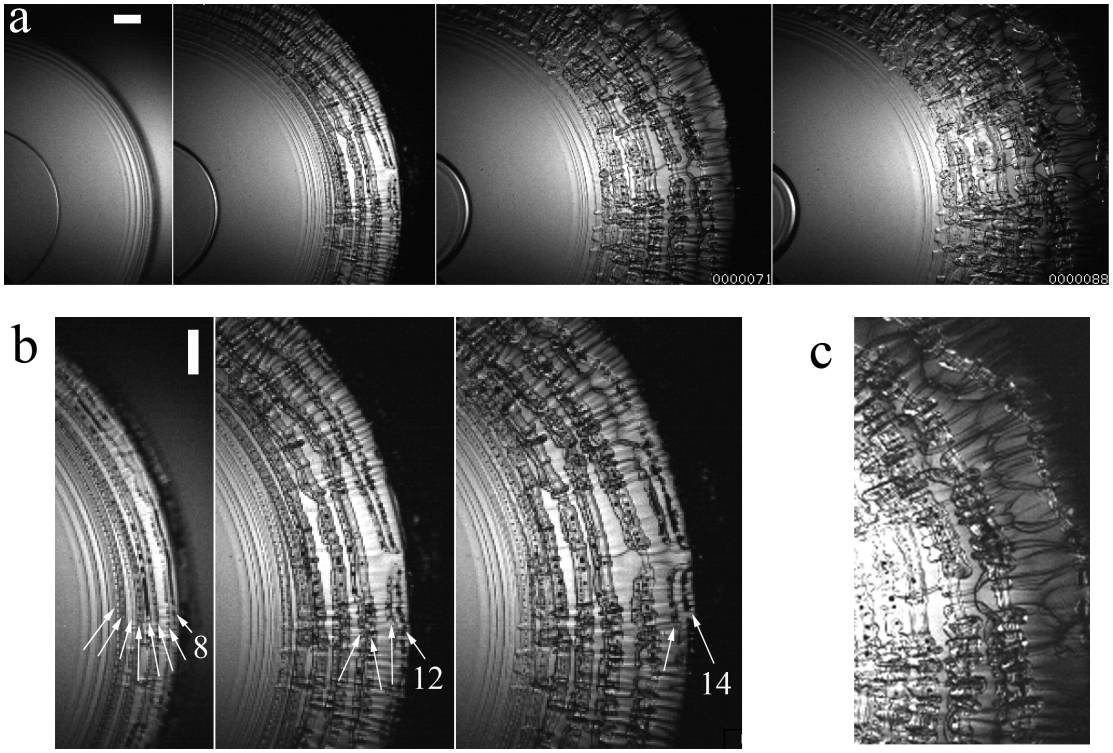

Figure 4.24: Bubble rings and vortex entanglement (Re = 12 900, α = 0.80). (a) Frames shown are 8, 22, 41 & 58 μs from first contact on ethanol (δ = 250 μm). (b) Careful examination of the fine bubbles, show 14 separate bubble rings, which are pointed out by the arrows. (c) Close-up of the vortex tangles at t = 58 μs. The scale bars are 100 μm long. See also supplementary video.

the later dynamics shows the secondary streamwise vortex tubes roll up around the primary spanwise vortex ring. Figure 4.23(b) shows a similar case where streamwise vortices roll-up around a vortex ring. This roll-up can be identified by following two micro-bubbles at the core of the vortices (black arrows).

Interesting parallels can be made with similar three-dimensional instabilities occurring in the wake of a cylinder (Williamson, 1996). The local Reynolds number at the base of the ejecta sheet Re_b will be affected by both the radial velocity of the neck and the velocity within the liquid. Re_b can be increased both by increasing the impact velocity or by using a more oblate drop. Indeed, as the impact Re increases, the ejecta sheet emerges from a faster moving neck (Josserand and Zaleski, 2003, Thoraval et al., 2012b), and at a higher velocity (Thoroddsen, 2002, Josserand and Zaleski, 2003), thus leading to higher Re_b. A flat bottom drop also geometrically generates a faster moving neck, and produces larger velocities in the liquid, see Fig. 4.15. Both effects lead to a larger concentration of streamwise vortices (Figs. 4.8(e), 4.10, 4.22(a), 4.23 & 4.24). This is similar to the onset of three-dimensional instabilities of the vortex street behind a circular cylinder (Williamson, 1988, 1996), where finer streamwise vortices and a smaller spanwise wavelength are observed at higher Re. Similar vortex loops are also observed in both cases, as described above. Moreover, rapid motion of the bubbles in the spanwise direction along the vortices is observed in our experiments, see Figs. 4.5(f) and 4.9. Similar lateral motion was also observed behind "vortex dislocations" in the wake of a cylinder (Williamson, 1992, 1996).

4.4 Conclusions

Observations from below the impacting drop have herein demonstrated that the mechanism suggested in Thoraval et al. (2012b) does indeed entrap micron sized air tori. The oscillations of the ejecta sheet can thereby entrap a row of

bubble rings. The vorticity entering the liquid during those oscillations and bubble entrapments is then destabilized into complex 3D structures. The combination of azimuthal instabilities and vertical oscillations of the ejecta sheet produces a large range of new bubble entrapment scenarios.

Besides imaging the formation and breakup of partial bubble rings, of equal significance is our observation that for water-on-water impacts the outer neck is unstable to azimuthal undulations at even very moderate Reynolds numbers (Figs. 4.5(d) & 4.6). This poses a challenge to theoretical and numerical studies, which invariably assume axisymmetry.

We note that the bubble rings observed herein differ in fundamental ways from the Oguz-Prosperetti rings (Oguz and Prosperetti, 1989), as the base of the ejecta here is not driven by surface tension, but rather by the impact pressure. This high localized pressure is indeed the mechanism responsible for driving out the ejecta sheet.

However, the details of the air entrapment and its dependence on the impact conditions is still not clear. Large scope exists for further work, as the present study perhaps raises as many questions as it answers. What role do Marangoni or Rayleigh-Taylor instabilities play in the two-liquid dynamics? The large parameter space of other liquids needs to be studied. Even for the same liquids, in the drop and pool, the interplay between Re, We and α which allows bubble ring entrapment, or preserves an extended axisymmetric ejecta, remains to be determined. The three-dimensional instabilities of the vortex street also need to be studied in more detail and compared to the well-known instabilities of the cylinder wake and the shear layer. However, in the vortex street observed here, the vortices are shed from a deformable free-surface, adding to the complexity of the analysis. The influence of the shed vorticity on the dynamics of the neck, both vertically and in the azimuthal direction, should also be added to the factors influencing the stability analysis of splashing.

Chapter 5

Micro-bubble morphologies at low impact velocities

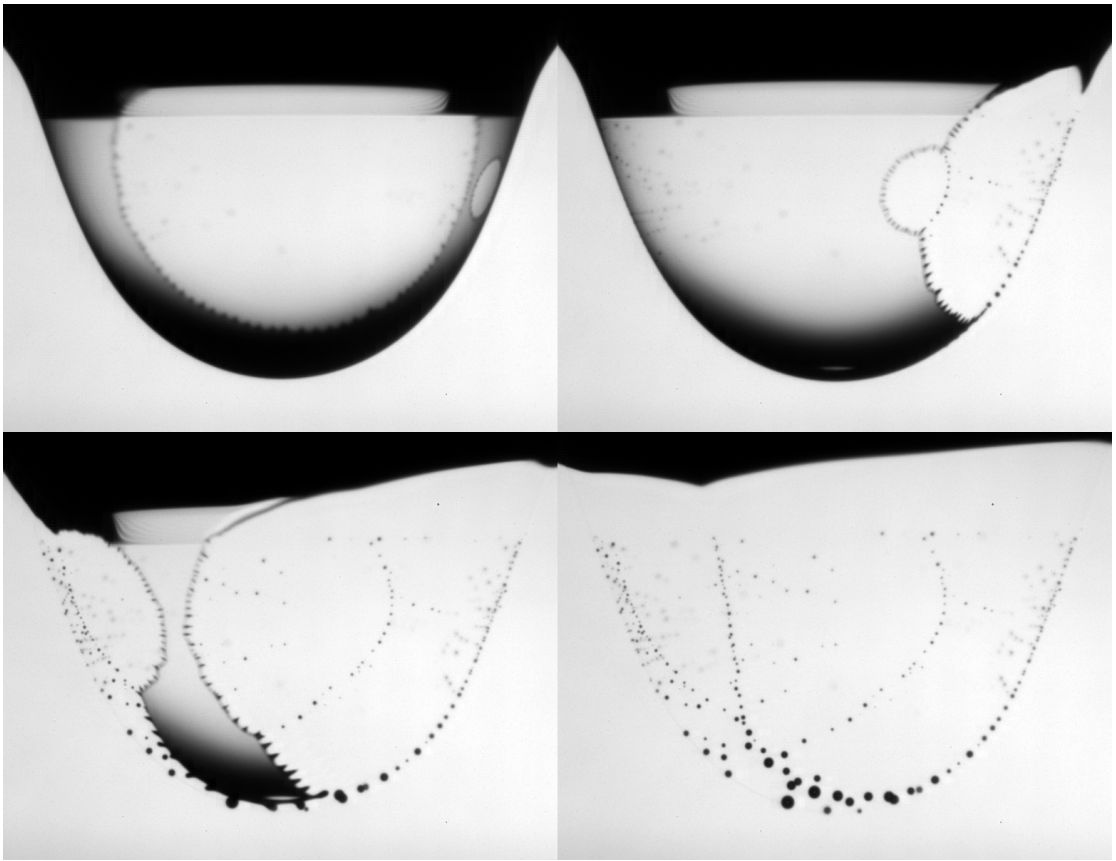

Figure 5.1: Breakup of the air film in a bubble necklace for a drop of ν = 10 cSt silicone oil on a deep pool of the same liquid, for Re = 103, We = 21, D = 2.4 mm, U = 0.43 m/s. Frames are shown 250 μs apart. Figure selected as the cover of *Journal of Fluid Mechanics*, Volume **708**. See supplemental video.

Abstract

When a drop impacts at low velocity onto a pool surface, a hemispheric air layer cushions and can delay direct contact. Herein we use ultra-high-speed video to study the rupture of this layer to explain the resulting variety of observed distribution of bubbles. The size and distribution of microbubbles is determined by the number and location of the primary punctures. Isolated holes lead to the formation of bubble necklaces when the edges of two growing holes meet, whereas bubble nets are produced by regular shedding of micro-bubbles from a sawtooth edge instability. For the most viscous liquids the air film contracts faster than the capillary-viscous velocity through repeated spontaneous ruptures of the edge. From the speed of hole opening and the total volume of micro-bubbles we conclude the air sheet ruptures when its thickness approaches ~ 100 nm.

This chapter is based on Thoroddsen et al. (2012e).

5.1 Introduction

The impact of a drop onto a pool surface can greatly enhance the gas-transfer through the liquid-air interface and is therefore of interest in diverse fields such as climate and marine science (Wanninkhof et al., 2009, Czerski et al., 2011). The bursting of a sub-micron gas film is also important to understand the fundamental mechanisms involved in film breakup (de Gennes et al., 2004, Reiter and Sharma, 2001, Reyssat and Quéré, 2006, Neitzel and Dell'Aversana, 2002) and the microbubbles generated can enhance nucleate boiling (Dhir, 1998). For low impact velocities, the air under the drop cushions the impact and prevents immediate contact. This layer can stretch into a submicron hemispheric film of air, which either causes rebounding of the drop (Couder et al., 2005), or ruptures to form a myriad of entrapped micro-bubbles. The details of this rupture are unknown, principally due to the very rapid capillary-driven motions. Mesler and co-workers (Esmailizadeh and Mesler, 1986, Sigler and Mesler, 1990). presented a series of papers showing snapshots of bubble structures for water, without time-resolved imaging.

Thoroddsen et al. (2003) imaged detailed dynamics of the entrapment of a central bubble, along with a handful of realizations for film breakup for water drops. However, Mills et al. (2012) showed convincingly that the water case suffers from highly random film ruptures and is not repeatable, even if surfactants are included. Recently, Saylor and Bounds (2012) have shown that air film formation and breakup are much more repeatable for silicone oils than for water. We exploit this discovery to allow for precisely triggered observations with ultra-high-speed video imaging, at frame-rates up to 1 million fps (Etoh et al., 2003), to explain the mechanisms underlying the variety of observed bubble morphologies, such as bubble necklaces and bubble nets.

Liquid	Density ρ [g/cm^3]	Viscosity μ [cP]	Surf. tens. σ [dyn/cm]	Cap. length a [mm]	Capill. Velo. σ/μ [m/s]	Crit. thick. δ_* $2\mu^2/(\rho\sigma)$ [μm]
Distilled water	0.997	0.894	72.1	2.72	80.6	0.0222
Perfluorohexane	1.710	1.1	11.9	0.842	10.8	0.120
Silicone oil 0.65	0.760	0.494	15.9	1.46	32.2	0.0404
Silicone oil 1	0.818	0.818	16.9	1.45	20.7	0.0968
Silicone oil 5	0.915	4.57	19.7	1.48	4.31	2.32
Silicone oil 10	0.935	9.35	20.1	1.48	2.15	9.30
Silicone oil 30	0.955	28.6	20.8	1.49	0.726	82.6
Silicone oil 100	0.965	96.5	20.9	1.49	0.217	923
Silicone oil 350	0.970	340	21.1	1.49	0.0622	11300
Silicone oil 1000	0.970	970	21.2	1.49	0.0219	91500

Table 5.1: Properties of the different liquids used in the experiments. Properties for Silicone oils are taken from the *ShinEtsu* data sheets.

5.2 Experimental Setup

We use drops of silicone oils over a wide range of viscosities from ν = 0.65 to 1000 cSt, as well as perfluorohexane liquid (C_6F_{14}), with properties given in Table 1. The impact conditions are characterized by a Reynolds number, $Re = \rho DU/\mu$ and a Weber number $We = \rho DU^2/\sigma$, where D is the drop diameter (1.6-3 mm) and U is the impact velocity ($\sim$ 0.5 m/s); ρ, μ and σ are respectively the density, dynamic viscosity and surface tension of the liquid. The ultra-high-speed video camera (Etoh et al., 2003) takes 102 frames with 312×260 px, irrespective of the frame rate used. In combination with a long-distance microscope we get down to a resolution of 2.1 μm/px.

5.3 Results

5.3.1 Bubble morphology: Hanging necklaces and bubble chandeliers.

Figure 5.2(a) shows a typical rupture of the highly stretched air film. Here the rupture occurs simultaneously at two points with the holes rapidly growing in size and traveling around the periphery leaving a *necklace* of bubbles where the holes

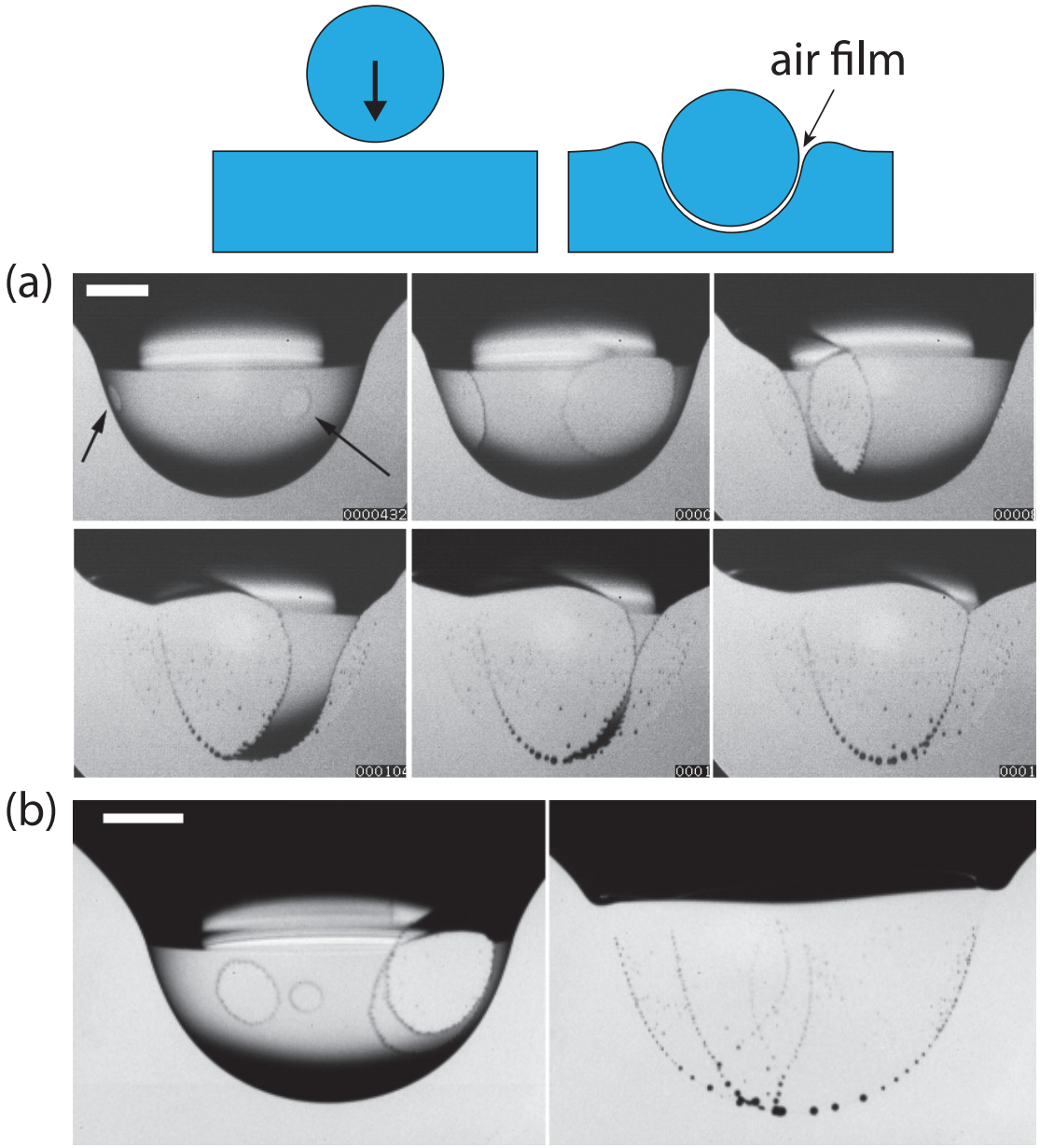

Figure 5.2: Typical formation of a hanging bubble necklace for silicone oil, ν = 10 cSt, for Re = 103, We = 21, D = 2.4 mm, U = 0.43 m/s. (a) The air sheet punctures at two places (arrows), the right puncture is on the back-side of the axisymmetric air hemisphere. The frames are shown at 48, 208, 464, 656, 752 & 816 μs, relative to the time where the first rupture is observed. (b) Bubble lines following the rupture of 6 holes (4 visible in first frame, with 2 forming later on) as shown by the 6 final bubble lines. Frames shown at t = 192 & 800 μs after start of first rupture. Scale bars 500 μm. See also supplemental videos.

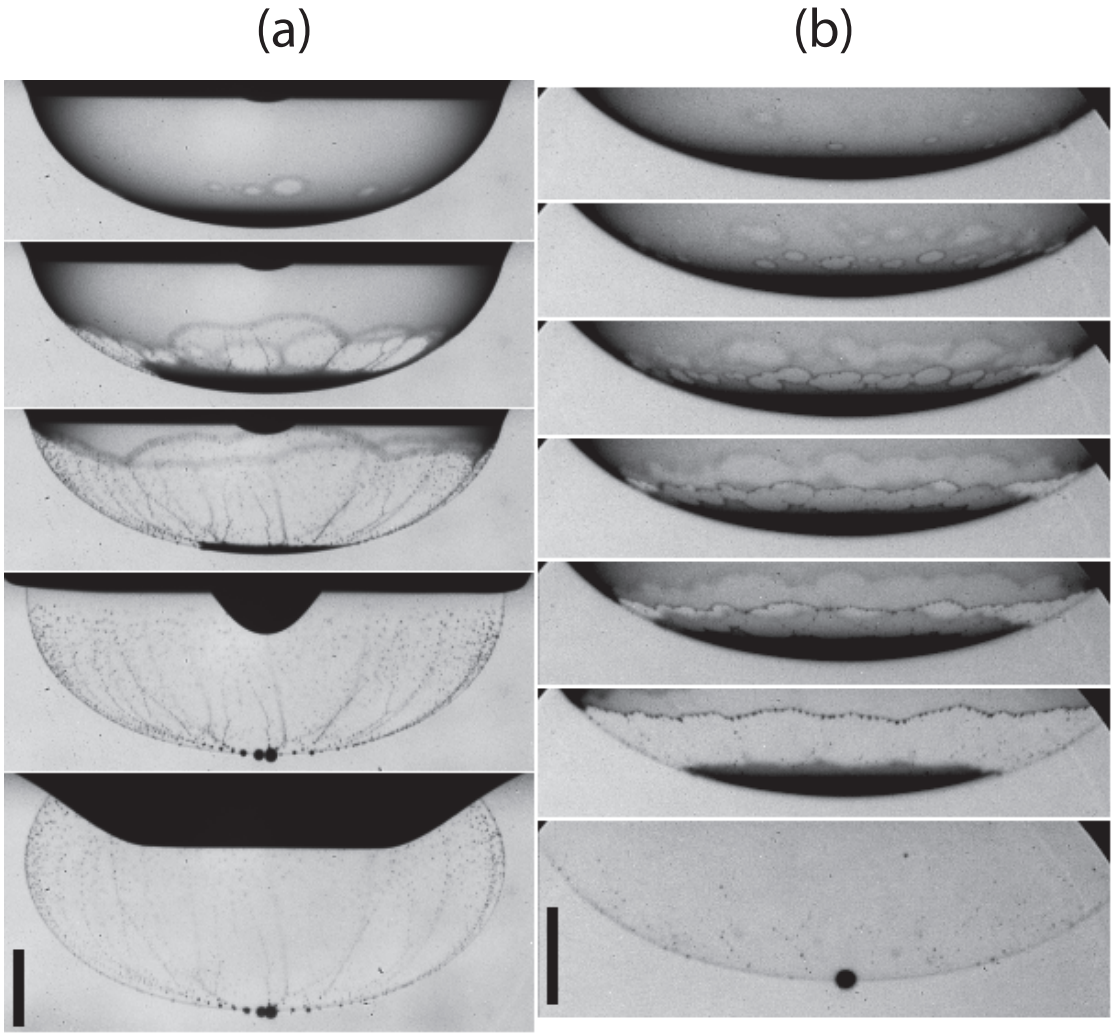

Figure 5.3: Typical bottom ring of ruptures leading to the formation of *bubble chandeliers* for D = 2.4 mm and (a) 5 cSt silicone oil, at Re = 220, We = 24, U = 0.46 m/s, shown at t = 0, 64, 160, 512 & 2656 μs after first puncture. (b) For 30 cSt silicone oil, at Re = 50, We = 43, U = 0.63 m/s. First 5 frames are spaced by 32 μs. The bottom bubble has d_b =114 μm, giving an average thickness of bottom air-cap, below the ring of ruptures, as $\delta \simeq 250$ nm. Bars are 500 μm. See supplemental videos.

meet, in a vertical plane. If only two holes are formed this is the inevitable resulting bubble structure, no matter how far apart these two holes are situated along the periphery, as there is always a vertical plane of symmetry cutting between these two holes. The gradual variation of bubble sizes along the necklace suggests that the film thickness and its area is imprinted onto the necklace, i.e. where the film is thicker, the bubbles are larger and vice-versa. This assumes the air flow within the thin film is insignificant compared to the motion of the edge. Based on the bubble size distribution, in Fig. 5.2(a), we infer that the film is thicker along the bottom and ruptures first at a fixed intermediate depth along the side-wall, where we expect the film to be thinnest, i.e. where the bubbles are smallest along the necklace and the film area is largest. Figure 5.2(b) shows another realization with 6 holes, which leaves 6 separate branches of bubbles. The net of bubble-lines is therefore a consequence of the original number and location of ruptures.

In Fig. 5.2 the isolated punctures in the air film appear when the impact is near the bouncing boundary where surface tension and viscous stresses have fully decelerated the drop, whereas for higher impact velocities the ruptures occur during stretching and thinning of the film. Ruptures therefore tend to occur at numerous locations simultaneously. Figure 5.3 shows such cases, where a multitude of ruptures occur along an azimuthal ring. This splits the hemisphere into two sections, one is pulled downwards to form a bottom bubble, whereas the rest is pulled upwards leaving faint vertical trails of micro-bubbles where the original holes meet. The edge moves much faster up away from the ruptures, again suggesting a significantly thinner air-layer along the sides. Similar formation of multiple holes along a ring may explain the *bubble chandeliers* observed in water (Sigler and Mesler, 1990, Mills et al., 2012, Liow and Cole, 2007).

Figure 5.4 shows the parameter regions, in terms of We and Ohnesorge ($Oh = \mu/\sqrt{\rho\sigma D}$) numbers, where the various breakup mechanisms occur. It identifies the lower boundary between bouncing drops and film rupture. This occurs at $We = 12$

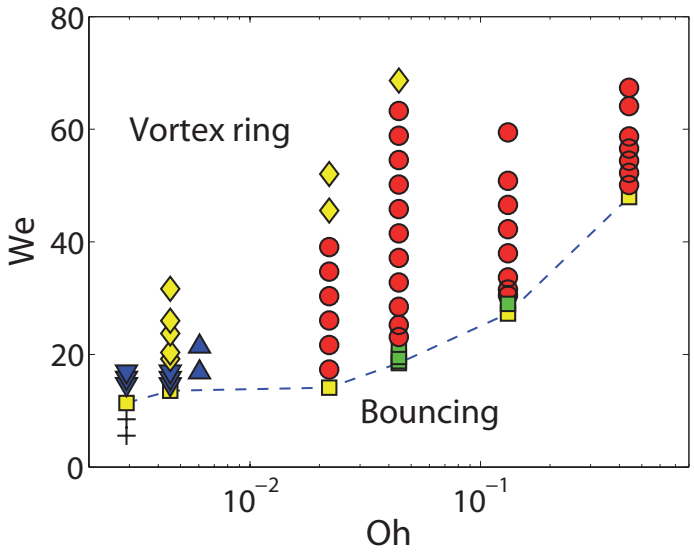

Figure 5.4: Parameter space of the experiments for a range of silicone oil viscosities and impact velocities. (-□-) Upper boundary for bouncing drops. (■) Isolated holes (< 10 ruptures). (●) Multiple ruptures along an azimuthal ring. (▼, ▲) Central jet and bottom puncture, including experiments with perfluorohexane identified by ▲. (◆) Early entrapment of a central air disk. (+) Film ruptures during late stage of crater rebound.

& 18 for 0.65 and 10 cSt silicone oils respectively, in good agreement with earlier results Saylor and Bounds (2012). Figure 5.5 shows how the depth of the ring of ruptures moves progressively closer to the original free surface, as the drop impact velocity increases. This approaches the early entrapment of an air disk as studied by Thoroddsen et al. (2003).

We expect the punctures to occur by van der Waals forces destabilizing the very thin films (≃ 200 nm (Couder et al., 2005). The azimuthal spacing of the initial holes is ~ 200 μm (estimated from second panel in Fig. 5.3b) which is in qualitative agreement with the wavelength λ which balances van der Waals and capillary pressures (Dorbolo et al., 2005), i.e. $\lambda = \delta^2/\sqrt{A/(6\pi\sigma)} \sim 100$ μm, where $\delta \simeq 200$ nm is the air film thickness, if we use 5×10^{-20} J for the Hamaker constant A, following Israelachvili (2011). The strong dependence on δ is in good agreement with new holes opening in time (Fig. 5.3), and the sharp transition from isolated

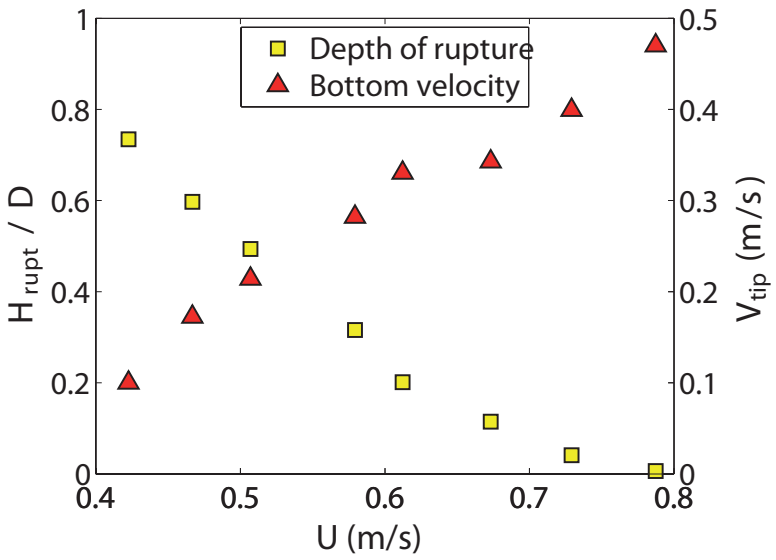

Figure 5.5: Depth of the ring of ruptures (■) and penetration velocity (▲) at the bottom tip of the air film at time of rupture, vs impact velocity, for 10 cSt and $Oh = 0.044$.

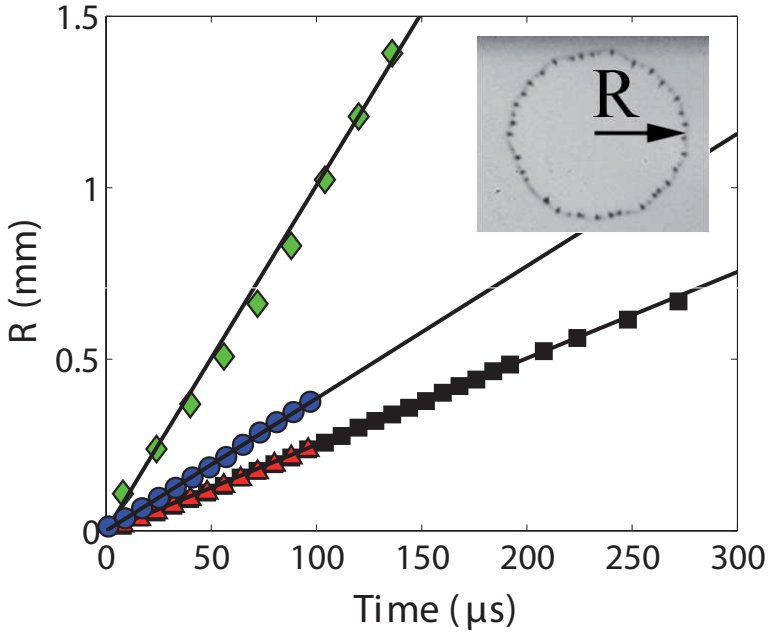

Figure 5.6: Horizontal hole radius vs time for silicon oils of 0.65 (♦), 5 (●) and 10 cSt (■,▲). The holes open up at a nearly constant velocity of 11, 3.8 & 2.5 m/s respectively.

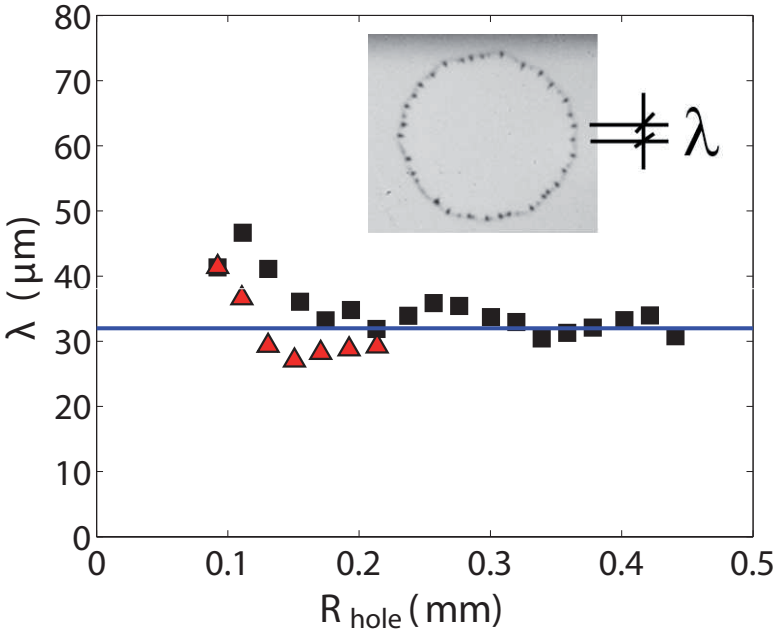

Figure 5.7: Average wavelength of the edge undulations for 10 cSt.

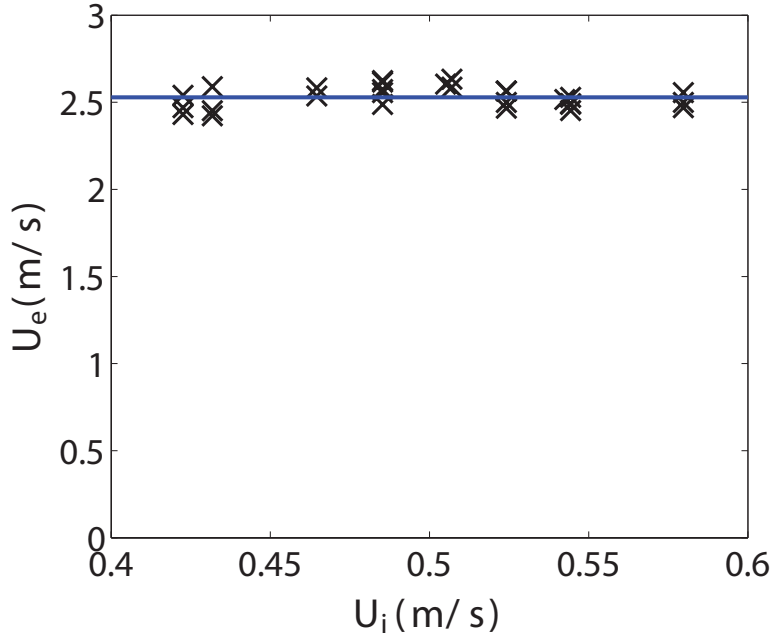

Figure 5.8: Horizontal rupture speed of the edge of the air film within 10 cSt silicon oil, measured for a range of different drop impact velocities, at $Oh = 0.044$.

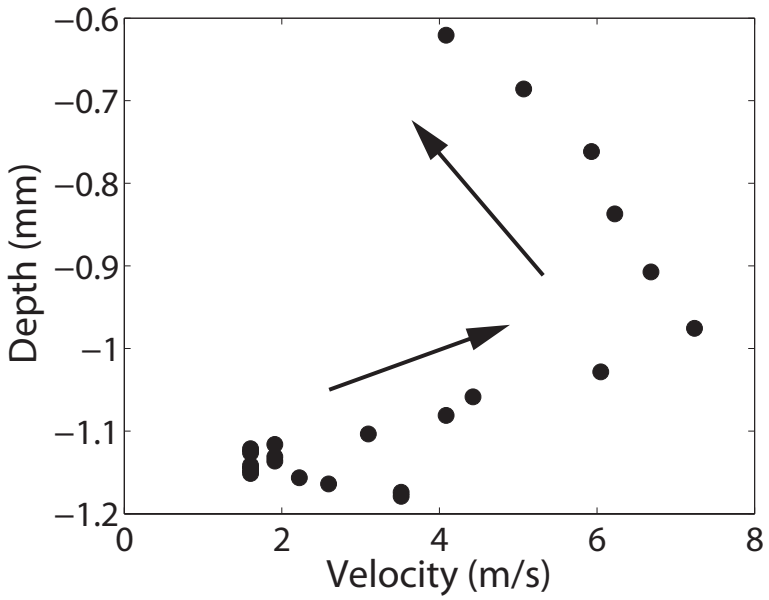

Figure 5.9: Rupture velocity following the bottom tip rupture from a central jet, for perfluorohexane drop, corresponding to Figure 5(a), $Re = 640$ and $We = 15$.

holes to multiple ruptures as impact velocity increases, thinning the film faster.

5.3.2 Film thickness and speed of rupture

During drop impacts the lubrication pressure in the air creates a dimple below the drop thereby entrapping a bottom disk of air, as shown by Thoroddsen et al. (2003). Similar film thickness distributions are observed in numerous drainage films, as reviewed by Chan et al. (2011), and more recently by high-speed observations of van der Veen et al. (2012) for a water drop impacting a solid surface. The thinner air film along the side of the crater is also consistent with our observations of the film breaking on the side, and the final bubble distribution.

After rupture of the air film, it retracts under the action of surface tension. When viscous effects can be neglected, the velocity of the edge can be estimated by the Taylor-Culick velocity $u_\sigma = \sqrt{2\sigma/(\rho\delta)}$ (Oguz and Prosperetti, 1989, Brenner and Gueyffier, 1999, Song and Tryggvason, 1999, Lhuissier and Villermaux, 2011, Gordillo et al., 2011). This approximation is valid for films thicker than $\delta_\star =$

$2\mu^2/(\rho\sigma)$. For our lowest viscosity case (ν = 0.65 cSt), the edge velocity of 11 m/s (Fig. 5.6) would correspond to δ = 350 nm, consistent with previous estimate and larger than $\delta_\star$ = 40 nm (see Table 5.1). However, for more viscous drops (ν = 5 and 10 cSt), the edge velocity decreases, suggesting that viscous effects become important. Indeed, an estimate based on micro-bubble volumes gives a thickness on the side of $\delta \simeq 125$ nm, for ν = 10 cSt in Fig. 5.10(a), smaller than $\delta_\star \sim 10$ μm. In this viscous dominated regime, the edge velocity now scales as the capillary-viscous velocity $u_\mu = \sigma/\mu$ (Reyssat and Quéré, 2006, Aryafar and Kavehpour, 2008). Note that δ no longer enters this relationship, as the driving surface tension and resisting viscous stress have the same dependence on the characteristic length scale δ. This is consistent with the edge velocity for 10 cSt in Fig. 5.6, where $Ca_e = u_e\mu/\sigma = 1.16$, i.e. viscous balanced. This transition is made clear in Fig. 5.14 by comparing experimental measurements with theory over a large range of viscosities.

5.3.3 Rupture speed is independent of drop impact velocity

As a consequence of the proposed van der Waals rupture mechanism, the local thickness of the film when it ruptures should be the same irrespective of how the dynamics reached this air film thickness. Moreover, for this intermediate viscosity of 10 cSt, the edge velocity of such thin films is mostly influenced by viscosity and will not depend strongly on the film thickness. Therefore, we expect that the horizontal hole-opening rupture velocity will not depend on the drop impact velocity. We have verified this over a range of drop impact velocities where individual hole openings can be measured, showing no significant variation in Fig. 5.8. These experiments were performed for a fixed Ohnesorge number $Oh = \mu/(\sqrt{\rho\sigma D}) = 0.044$, while varying the impact velocity.

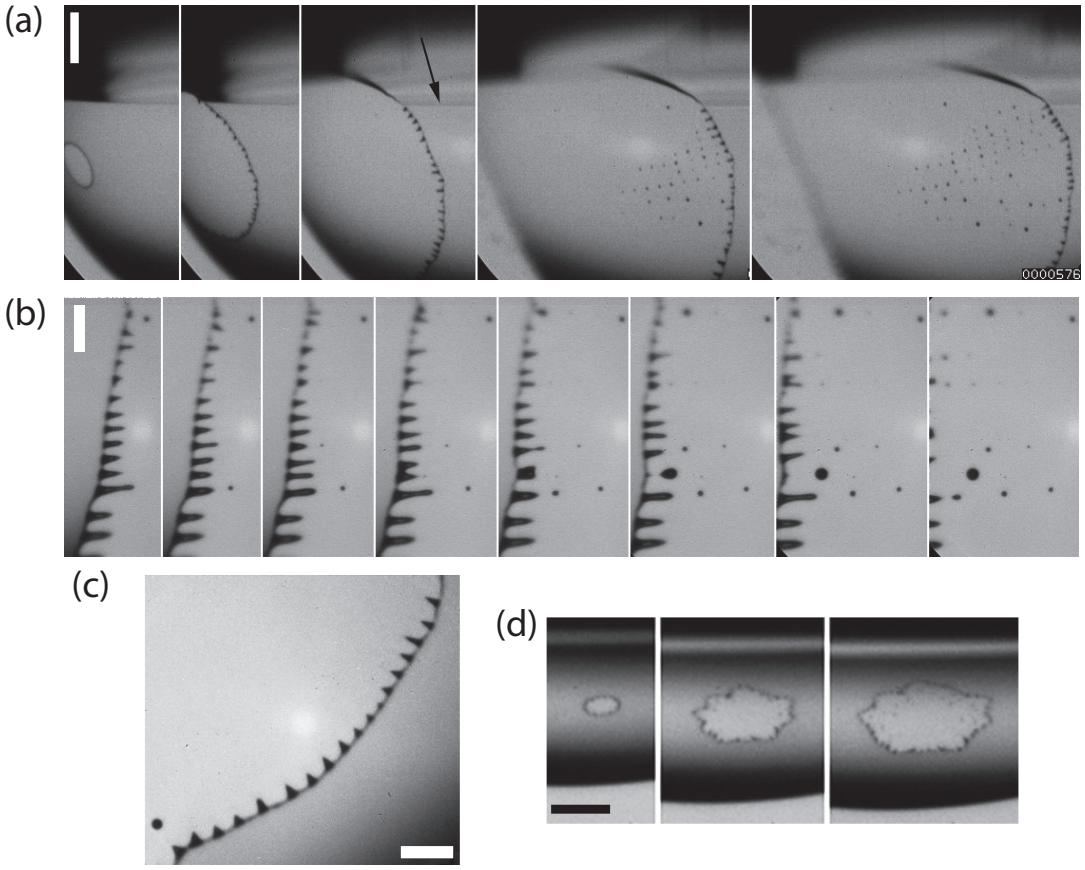

Figure 5.10: Typical formation of edge instabilities, for 10 cSt silicone oil in (a,b,c) and 100 cSt in (d). (a) Typical formation of a bubble net, at Re = 100, We = 20. The frames are shown 34, 130, 242, 418 & 514 μs after rupture. Bar is 200 μm. The average thickness of the air sheet, can be estimated by assuming steady state in the air flow and measuring the area and bubble-volume within the net at the vertical location of the rupture, giving $\delta \simeq 125$ nm ±25%. (b,c) Typical instability at the edge of the growing hole, for Re = 127, We = 28. The frames are spaced by 16 μs. Some teeth shed evenly spaced bubbles in a row, while a larger bubble is shed when two adjacent teeth merge. Micro-bubble diameters are here between 5 - 30 μm. Bar is 100 μm. (c) Regular meta-stable shark-teeth undulations, with the edge moving to the bottom right. Bar is 100 μm. (d) Star-like sub-harmonic undulations on the edge, for Re = 19, We = 67. Bar 200 μm. See supplemental videos.

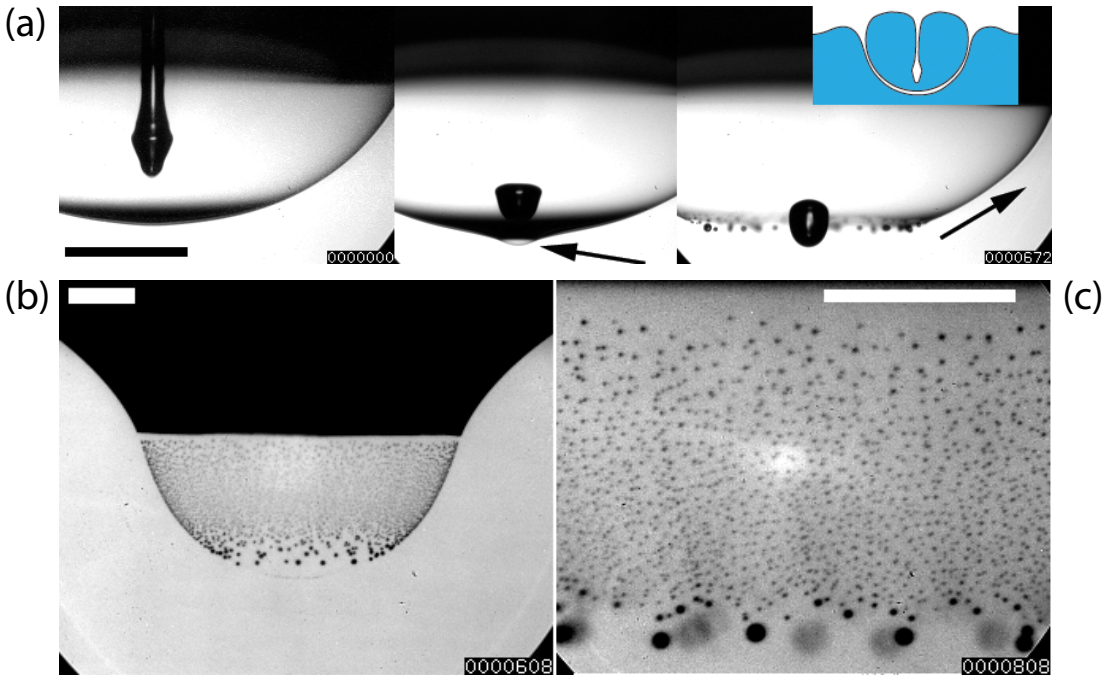

Figure 5.11: (a) Film puncturing for *perfluorohexane*, at Re = 640, We = 15. The jet generated by the collapse of the cylindrical cavity which forms at the top of the drop, penetrating to the bottom, where it pushes the air film downwards on the centerline, to form a pronounced dimple (arrow in middle frame) puncturing the film, subsequently retracting upwards towards the pool surface, breaking into a net of bubbles. The edge velocity is shown in Fig. 5.9. (b) Close-up of the bubble morphology, following punctures at the bottom tip, for silicone oil ν =1 cSt, at Re = 880, We = 16. (c) Close-up of a bubble net, with a total of ~ 5600 microbubbles produced for silicone oil ν =1 cSt, at Re = 980, We = 20. Bars are 500 μm. See supplemental videos.

5.3.4 Edge Instability: Breakup of the growing edge

The edge of the hole in the air layer does not initially shed bubbles, but grows thicker as it collects the air from the receding air layer and develops a spanwise instability leading to the separation of micro-bubbles. Figure 5.10 shows typical shapes of the expanding edge, revealing regular *teeth*, here spaced by about 38 μm. For new holes the undulations are already visible 34 μs after puncture, growing in amplitude and the first micro-bubbles are shed 250 μs after the hole opens. For small holes, the wavelength of the teeth is approximately constant, with new teeth growing or suddenly appearing between the old ones, as the length of the hole periphery grows (Fig. 5.7). Closer to the bottom cap the teeth become larger as the film is thicker. Two main mechanisms produce the bubbles, i.e. regular shedding from the tips of the teeth and secondly by the sideways motion of two adjacent teeth. When they merge they grow in size and pinch off a larger bubble. Both mechanisms are present in Fig. 5.10(b). The spacing of trailing bubbles is fairly regular, but they emerge at distinct locations along the front, often leaving behind a *bubble net*.

Figure 5.10(c) is a close-up of the teeth, which are initially stable. Their base and amplitude are about equal size, around 25 μm. They are therefore much wider than the thickness of the air-sheet feeding them and are thereby semi-stable and flat structures, consistent with numerical work of a retracting liquid edge (Bagué et al., 2007). The undulations end abruptly, where the film becomes thicker as the drop and free surface start to diverge from each other, see the arrow in the third frame in Fig. 5.10(a). The spacing of these teeth along the edge appears related to the local thickness of the air film. For example in Fig. 5.10(b) they are wider closer to the bottom of the curved interface.

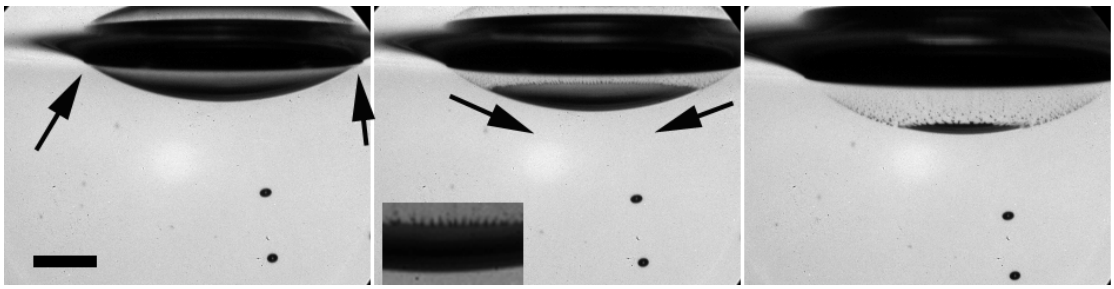

Figure 5.12: Formation of a bubble cap for silicone oil of ν = 1000 cSt, for $Re \sim 2$, $We \sim 100$, at t = 1.15, 1.47 and 2.69 ms after impact. Rupture starts axisymmetrically at the outer edge (arrows) in the first frame. The volume of air in the bottom bubble (3.3 $\times 10^{-4}$ mm^3) and all the microbubbles (6.9 $\times 10^{-4}$ mm^3, estimated by counting individual bubbles) divided by the area of the bubble cap in the first frame (3.7 mm^2) gives an average $\delta \simeq 270$ nm. Bar is 500 μm. Inset shows rupturing of the edge. See supplemental video.

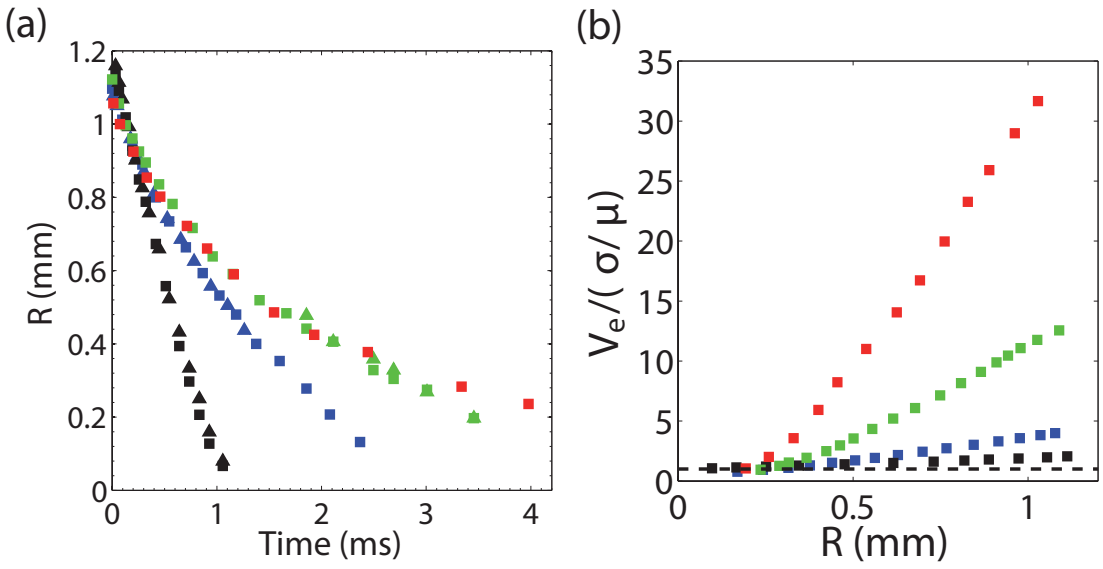

Figure 5.13: (a) Contraction of the air cap, for ν = 30 (■,▲), 100 (▲), 350 (■,▲), 1000 cSt (■). (b) Contraction velocity normalized by capillary viscous velocity.

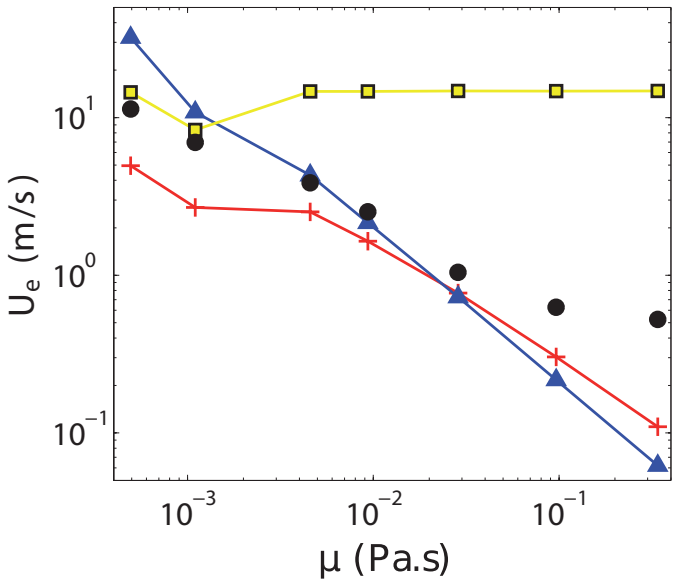

Figure 5.14: Maximum horizontal edge velocity of ruptures for different viscosities (●). Compared to σ/μ (-▲-); the logarithmic correction presented in Reyssat and Quéré (2006) (-+-) and Taylor-Culick velocity $\sqrt{2\sigma/(\rho\delta)}$ (-□-), assuming 200 nm film thickness.

5.3.5 Bottom puncturing by a liquid jet

The largest deformations of a drop, as it hits the pool surface, are expected for drops larger than the capillary length $a = \sqrt{\sigma/(\rho g)}$. This is indeed born out in Fig. 5.11(a) where new dynamics emerge. In this particular configuration ($D/a \sim 2$) an air cavity is formed at the top of the drop, by its overall deformation during the impact (Bartolo et al., 2006, Thoroddsen et al., 2007). As this air cavity closes, it generates an internal air cylinder, and the surface deformations also generate a liquid jet which penetrates the drop to emerge at its bottom where it punctures the film at a pronounced dimple (arrow in second frame). For this configuration the air film has not reached the critical rupture thickness, but is forced by the jet to break at the axis of symmetry, making the overall breakup dynamics essentially axisymmetric, with the edge propagating upwards towards the pool surface. These internal drop dynamics can explain the large central bubble appearing in some of the earlier studies (Fig. 7(a) of Mills et al. (2012)).

The speed of the edge propagation can tell us something about the thickness of the air film, especially for low viscosities and thicker films, where we expect Taylor-Culick law to hold. In Fig. 5.9 we track the tangential velocity of the edge, vs. depth. It is clear that the bottom part of the air film is also thickest as the hole grows much slower in this region, developing a thick edge of air, until it encounters a much thinner section on the sides. This sudden reduction in thickness leaves a set of large bubbles along a ring, before very fast effective motion of the breakup front ($u_e \simeq 7$ m/s; $Ca_e = 0.65$) and production of uniform bubble nets, in Fig. 5.11(c). Without the puncturing of the bottom jet, one would expect the film to eventually rupture at the depth where the speed is maximum.

5.3.6 Larger liquid viscosities:

Figure 5.12 shows the contraction of the air sheet under the largest viscosity drop of silicone oil (ν =1000 cSt). The initial rupture occurs near the upper edge, often at isolated points, but the realization shown here ruptures axisymmetrically along the entire periphery and the edge moves downwards leaving a uniform distribution of micro-bubbles. The initial velocity of the apparent edge of the film u_e, is about 0.6 m/s, which is 30 times larger than the capillary-viscous velocity for this liquid, $u_\mu = \sigma/\mu \simeq 2$ cm/s. Therefore, the classical models where the film fluid is collecting in the rim cannot explain the motion of the edge. This is also illustrated in Fig. 5.14, where the horizontal edge velocity does not decrease as much as expected by the models at high viscosities. The rapid motion of the edge, must therefore proceed through a different mechanism, manifest by strong edge instability and radial ruptures of the air sheet, in Fig. 5.12. In a similar way, the dewetting rates of viscous films can increase by rim instabilities (Reiter and Sharma, 2001).

5.4 Conclusions

Herein we have imaged the various breakup mechanisms of submicron air layers caught under impacting drops. The systematic changes in the rupture depth give a clear way of estimating the We–Oh regime where bubble chandeliers are formed. The imaging of the resulting micro-bubbles gives us a direct estimate of the air film thickness at rupture. We have also identified a different puncture mechanism with a central jet traveling through the drop. These results will allow better estimates of the resulting air transport through air-liquid interfaces and may be the easiest way to repeatably produce such highly unstable submicron films of gas within a liquid.

Chapter 6

Concluding Remarks

In this dissertation, we have described new splashing mechanisms, and observed the breakup dynamics of the air film forming between the drop and the pool.

High speed imaging of the early dynamics of the ejecta sheet has revealed a large variety of phenomena, such as bumping, quartering, ejecta sheets rising on the drop and irregular splashing.

This systematic experimental study gave the overview necessary to chose the parameters of extremely high refinement numerical simulations of the impact, reproducing experimental features, and explaining the irregular splashing observed at high impact velocities.

Further high-speed imaging, up to a million frames per second, were necessary to verify experimentally some of the prediction of the numerical simulations. We have therefore been able to make the first observations of toroidal shaped bubbles entrapped below the drop, and liquid toroids detaching from the ejecta sheet. This brings an answer to the long standing question of the experimental evidence of these axisymmetric features, but may not be the only mechanisms producing them.

Finally, we have shown that the breakup of the air film below the drop happens through rupturing of its edge, by three-dimensional instabilities.

The results presented here may raise more questions than they answer. Many aspects still need to be clarified or explored further, such as the effect of different

liquids used in the drop and the pool, or a better modelling of these dynamics.

References

Agbaglah, G., Delaux, S., Fuster, D., Hoepffner, J., Josserand, C., Popinet, S., Ray, P., Scardovelli, R., and Zaleski, S. (2011). Parallel simulation of multiphase flows using octree adaptivity and the volume-of-fluid method. *Comptes Rendus Mécanique*, **339** (2-3): 194–207.

Agbaglah, G., Josserand, C., and Zaleski, S. (2013). Longitudinal instability of a liquid rim. *Physics of Fluids*, **25** (2): 022103.

Alcouffe, R. E., Brandt, A., Dendy, Jr., J. E., and Painter, J. W. (1981). The Multi-Grid Method for the Diffusion Equation with Strongly Discontinuous Coefficients. *SIAM Journal on Scientific and Statistical Computing*, **2** (4): 430–454.

Aryafar, H. and Kavehpour, H. P. (2008). Hydrodynamic instabilities of viscous coalescing droplets. *Physical Review E*, **78** (3): 037302.

Ashmore, J. and Stone, H. A. (2004). Instability of a rotating thread in a second immiscible liquid. *Physics of Fluids*, **16** (1): 29–38.

Aziz, S. D. and Chandra, S. (2000). Impact, recoil and splashing of molten metal droplets. *International Journal of Heat and Mass Transfer*, **43** (16): 2841–2857.

Bagué, A., Zaleski, S., and Josserand, C. (2007). Droplet formation at the edge of a liquid sheet. In *6th International Conference on Multiphase Flow*, paper No. 669, Leipzig, Germany.

Ball, P. (2012). Focus: Unexpected Turbulence in a Splash. *Physics*, **5**: 72.

Bartolo, D., Josserand, C., and Bonn, D. (2006). Singular Jets and Bubbles in Drop Impact. *Physical Review Letters*, **96** (12): 124501.

Batchelor, G. K. (2000). *An Introduction to Fluid Dynamics*. Cambridge University Press, Cambridge, UK.

Blanchard, D. C. and Woodcock, A. H. (1957). Bubble formation and modification in the sea and its meteorological significance. *Tellus*, **9** (2): 145–158.

Bolleddula, D. A., Berchielli, A., and Aliseda, A. (2010). Impact of a heterogeneous liquid droplet on a dry surface: Application to the pharmaceutical industry. *Advances in Colloid and Interface Science*, **159** (2): 144–159.

Brenner, M. P. and Gueyffier, D. (1999). On the bursting of viscous films. *Physics of Fluids*, **11** (3): 737–739.

Carroll, K. and Mesler, R. (1981). Part II: Bubble entrainment by drop-formed vortex rings. *AIChE Journal*, **27** (5): 853–856.

Castrejón-Pita, A. A., Castrejón-Pita, J. R., and Hutchings, I. M. (2012). Experimental observation of von Kármán vortices during drop impact. *Physical Review E*, **86** (4): 045301(R).

Chan, D. Y. C., Klaseboer, E., and Manica, R. (2011). Film drainage and coalescence between deformable drops and bubbles. *Soft Matter*, **7** (6): 2235–2264.

Chan, T. F. and W. L. Wan (2000). Robust multigrid methods for nonsmooth coefficient elliptic linear systems. *Journal of Computational and Applied Mathematics*, **123** (1-2): 323–352.

Chandra, S. and Avedisian, C. T. (1991). On the Collision of a Droplet with a Solid Surface. *Proceedings of the Royal Society A: Mathematical, Physical and Engineering Sciences*, **432** (1884): 13–41.

Chandrasekhar, S. (1981). *Hydrodynamic and Hydromagnetic Stability*. Dover Publications, New York.

Chatzikomis, C., Pattinson, S. W., Koziol, K. K. K., and Hutchings, I. M. (2012). Patterning of carbon nanotube structures by inkjet printing of catalyst. *Journal of Materials Science*, **47** (15): 5760–5765.

Coppola, G., Rocco, G., and de Luca, L. (2011). Insights on the impact of a plane drop on a thin liquid film. *Physics of Fluids*, **23** (2): 022105.

Cossali, G., Coghe, A., and Marengo, M. (1997). The impact of a single drop on a wetted solid surface. *Experiments in Fluids*, **22** (6): 463–472.

Couder, Y., Fort, E., Gautier, C.-H., and Boudaoud, A. (2005). From Bouncing to Floating: Noncoalescence of Drops on a Fluid Bath. *Physical Review Letters*, **94** (17): 177801.

Cresswell, R. W. and Morton, B. R. (1995). Drop-formed vortex rings- The generation of vorticity. *Physics of Fluids*, **7** (6): 1363–1370.

Czerski, H., Twardowski, M., Zhang, X., and Vagle, S. (2011). Resolving size distributions of bubbles with radii less than 30 μm with optical and acoustical methods. *Journal of Geophysical Research*, **116**: C00H11.

Davidson, M. R. (2002). Spreading of an inviscid drop impacting on a liquid film. *Chemical Engineering Science*, **57** (17): 3639–3647.

de Gennes, P.-G., Brochard-Wyart, F., and Quéré, D. (2004). *Capillarity and Wetting Phenomena: Drops, Bubbles, Pearls, Waves*. Springer.

de Ruiter, J., Oh, J. M., van den Ende, D., and Mugele, F. (2012). Dynamics of Collapse of Air Films in Drop Impact. *Physical Review Letters*, **108** (7): 074505.

DeBar, R. B. (1974). Fundamentals of the KRAKEN code. Technical report, California Univ., Livermore (USA).

Deegan, R. D., Brunet, P., and Eggers, J. (2008). Complexities of splashing. *Nonlinearity*, **21** (1): C1–C11.

Dhiman, R. (2009). *Splashing and breakup of droplets impacting on a solid surface*. Doctor of philosophy, University of Toronto.

Dhiman, R. and Chandra, S. (2008). Rupture of radially spreading liquid films. *Physics of Fluids*, **20** (9): 092104.

Dhiman, R. and Chandra, S. (2010). Rupture of thin films formed during droplet impact. *Proceedings of the Royal Society A: Mathematical, Physical and Engineering Sciences*, **466** (2116): 1229–1245.

Dhir, V. K. (1998). Boiling Heat Transfer. *Annual Review of Fluid Mechanics*, **30**: 365–401.

Dombrowski, N. and Fraser, R. P. (1954). A Photographic Investigation into the Disintegration of Liquid Sheets. *Philosophical Transactions of the Royal Society A: Mathematical, Physical and Engineering Sciences*, **247** (924): 101–130.

Dombrowski, N. and Johns, W. R. (1963). The aerodynamic instability and disintegration of viscous liquid sheets. *Chemical Engineering Science*, **18** (7): 203–214.

Dorbolo, S., Reyssat, E., Vandewalle, N., and Quéré, D. (2005). Aging of an antibubble. *Europhysics Letters (EPL)*, **69** (6): 966–970.

Driscoll, M. M. and Nagel, S. R. (2011). Ultrafast Interference Imaging of Air in Splashing Dynamics. *Physical Review Letters*, **107** (15): 154502.

Duchemin, L. and Josserand, C. (2011). Curvature singularity and film-skating during drop impact. *Physics of Fluids*, **23** (9): 091701.

Duchemin, L. and Josserand, C. (2012). Rarefied gas correction for the bubble entrapment singularity in drop impacts. *Comptes Rendus Mécanique*, **340** (11-12): 797–803, arXiv:1208.0159.

Eden, A. M., Bargteil, A. W., Goktekin, T. G., Eisinger, S. B., and O'Brien, J. F. (2007). A method for cartoon-style rendering of liquid animations. In *Proceedings of Graphics Interface 2007 on - GI '07*, 51–55, New York, New York, USA. ACM Press.

Edgerton, H. E. and Killian, J. R. (1939). *Flash! Seeing the unseen by ultra high-speed photography*. Hale, Cushman and Flint, Boston.

Eggers, J. and Villermaux, E. (2008). Physics of liquid jets. *Reports on Progress in Physics*, **71** (3): 036601.

Elmore, P. A., Pumphrey, H. C., and Crum, L. A. (1989). Further Studies of the Underwater Noise Produced by Rainfall. Technical report, University of Mississippi.

Emady, H. N., Kayrak-Talay, D., Schwerin, W. C., and Litster, J. D. (2011). Granule formation mechanisms and morphology from single drop impact on powder beds. *Powder Technology*, **212** (1): 69–79.

Esmailizadeh, L. and Mesler, R. (1986). Bubble entrainment with drops. *Journal of Colloid and Interface Science*, **110** (2): 561–574.

Etoh, T. G., Poggemann, D., Kreider, G., Mutoh, H., Theuwissen, A., Ruckelshausen, A., Kondo, Y., Maruno, H., Takubo, K., Soya, H., Takehara, K., Okinaka, T., and Takano, Y. (2003). An image sensor which captures 100 consecutive frames at 1 000 000 frames/s. *IEEE Transactions on Electron Devices*, **50** (1): 144–151.

Ferziger, J. H. and Perić, M. (2002). *Computational methods for fluid dynamics*. Springer, 3rd edition.

Fitt, B. D. L., McCartney, H. A., and Walkalate, P. (1989). The Role Of Rain In Dispersal Of Pathogen Inoculum. *Annual Review of Phytopathology*, **27**: 241–270.

Fontez, M. (2012). Caméras ultra-rapides: La violence du monde prise sur le vif. *Science & Vie*, **1143**: 82–91.

Foote, G. B. (1975). The Water Drop Rebound Problem: Dynamics of Collision. *Journal of the Atmospheric Sciences*, **32** (2): 390–402.

Fuster, D. (2013). An energy preserving formulation for the simulation of multiphase turbulent flows. *Journal of Computational Physics*, **235**: 114–128.

Garg, K., Krishnan, G., and Nayar, S. (2007). Material based splashing of water drops. In *EGSR'07 Proceedings of the 18th Eurographics conference on Rendering Techniques*, 171–182.

Gekle, S., Peters, I. R., Gordillo, J. M., van Der Meer, D., and Lohse, D. (2010). Supersonic Air Flow due to Solid-Liquid Impact. *Physical Review Letters*, **104** (2): 024501.

Gomaa, H., Weigand, B., Haas, M., and Munz, C. D. (2009). Direct Numerical Simulation (DNS) on the Influence of Grid Refinement for the Process of Splashing. In *High Performance Computing in Science and Engineering '08*, pages 241–255. Springer Berlin Heidelberg.

Gordillo, J., Sevilla, A., Rodríguez-Rodríguez, J., and Martínez-Bazán, C. (2005). Axisymmetric Bubble Pinch-Off at High Reynolds Numbers. *Physical Review Letters*, **95** (19): 194501.

Gordillo, L., Agbaglah, G., Duchemin, L., and Josserand, C. (2011). Asymptotic behavior of a retracting two-dimensional fluid sheet. *Physics of Fluids*, **23** (12): 122101.

Gueyffier, D. (2000). *Etude de l'impact de gouttes sur un film liquide mince. Développement de la corolle et formation de projections*. PhD thesis, Université Pierre et Marie Curie (Paris VI).

Gueyffier, D. and Zaleski, S. (1998). Formation de digitations lors de l'impact d'une goutte sur un film liquide. *Comptes Rendus de l'Académie des Sciences - Series IIB - Mechanics-Physics-Astronomy*, **326** (12): 839–844.

Gunn, R. and Kinzer, G. D. (1949). The terminal velocity of fall for water droplets in stagnant air. *Journal of Meteorology*, **6** (4): 243–248.

Harlow, F. H. and Shannon, J. P. (1967a). Distortion of a Splashing Liquid Drop. *Science*, **157** (3788): 547–550.

Harlow, F. H. and Shannon, J. P. (1967b). The Splash of a Liquid Drop. *Journal of Applied Physics*, **38** (10): 3855–3866.

Hicks, P. D. and Purvis, R. (2010). Air cushioning and bubble entrapment in three-dimensional droplet impacts. *Journal of Fluid Mechanics*, **649**: 135–163.

Hicks, P. D. and Purvis, R. (2011). Air cushioning in droplet impacts with liquid layers and other droplets. *Physics of Fluids*, **23** (6): 062104.

Hicks, P. D. and Purvis, R. (2012). Compressible air cushioning in liquid-solid impacts. In *Proceedings of 2nd International Conference on Violent Flows*, 1–8, Nantes, France.

Hirt, C. W. and Nichols, B. D. (1981). Volume of fluid (VOF) method for the dynamics of free boundaries. *Journal of Computational Physics*, **39** (1): 201–225.

Howison, S. D., Ockendon, J. R., Oliver, J. M., Purvis, R., and Smith, F. T. (2005). Droplet impact on a thin fluid layer. *Journal of Fluid Mechanics*, **542**: 1–23.

Hulse-Smith, L., Mehdizadeh, N. Z., and Chandra, S. (2005). Deducing Drop Size and Impact Velocity from Circular Bloodstains. *Journal of Forensic Sciences*, **50** (1): JFS2003224.

Israelachvili, J. N. (2011). Van der Waals Forces between Particles and Surfaces. In *Intermolecular and Surface Forces*, chapter 13, pages 253–289. Elsevier, 3rd edition.

Josserand, C., Ray, P., and Zaleski, S. (2010). Air entrapment and splashing treshold in drop impacts. In *7th International Conference on Multiphase Flow, ICMF 2010*, 1–7.

Josserand, C. and Zaleski, S. (2003). Droplet splashing on a thin liquid film. *Physics of Fluids*, **15** (6): 1650–1657.

Jung, S. and Hutchings, I. M. (2012). The impact and spreading of a small liquid drop on a non-porous substrate over an extended time scale. *Soft Matter*, **8**: 2686–2696.

Kayafas, G., Jussim, E., and Edgerton, H. E. (1987). *Stopping Time: The Photographs of Harold Edgerton*. Henry N. Abrams, New York, NY, USA.

Kiger, K. T. and Duncan, J. H. (2012). Air-Entrainment Mechanisms in Plunging Jets and Breaking Waves. *Annual Review of Fluid Mechanics*, **44**: 563–596.

Kim, J. (2007). Spray cooling heat transfer: The state of the art. *International Journal of Heat and Fluid Flow*, **28** (4): 753–767.

Knock, C. and Davison, M. (2007). Predicting the position of the source of blood stains for angled impacts. *Journal of Forensic Sciences*, **52** (5): 1044–1049.

Kolinski, J. M., Rubinstein, S. M., Mandre, S., Brenner, M. P., Weitz, D. A., and Mahadevan, L. (2012). Skating on a Film of Air: Drops Impacting on a Surface. *Physical Review Letters*, **108** (7): 074503.

Korobkin, A. A., Ellis, A. S., and Smith, F. T. (2008). Trapping of air in impact between a body and shallow water. *Journal of Fluid Mechanics*, **611**: 365–394.

Krechetnikov, R. (2010). Stability of liquid sheet edges. *Physics of Fluids*, **22** (9): 092101.

Krechetnikov, R. and Homsy, G. M. (2009). Crown-forming instability phenomena in the drop splash problem. *Journal of Colloid and Interface Science*, **331** (2): 555–559.

Lamb, H. (1945). *Hydrodynamics*. Dover Publications, New-York, 6th edition.

Lasheras, J. C. and Choi, H. (1988). Three-dimensional instability of a plane free shear layer: an experimental study of the formation and evolution of streamwise vortices. *Journal of Fluid Mechanics*, **189**: 53–86.

Lezzi, A. M. and Prosperetti, A. (1991). The stability of an air film in a liquid flow. *Journal of Fluid Mechanics*, **226**: 319–347.

Lhuissier, H. and Villermaux, E. (2009). Soap Films Burst Like Flapping Flags. *Physical Review Letters*, **103** (5): 054501.

Lhuissier, H. and Villermaux, E. (2011). The destabilization of an initially thick liquid sheet edge. *Physics of Fluids*, **23** (9): 091705.

Liow, J.-L. and Cole, D. E. (2007). Bubble entrapment mechanisms during the impact of a water drop. In *16th Australasian Fluid Mechanics Conference (AFMC)*, 866–869, Brisbane, Australia. School of Engineering, The University of Queensland.

Liu, Y., Tan, P., and Xu, L. (2013). Compressible air entrapment in high-speed drop impacts on solid surfaces. *Journal of Fluid Mechanics*, **716**: R9.

Losasso, F., Gibou, F., and Fedkiw, R. (2004). Simulating water and smoke with an octree data structure. *ACM Transactions on Graphics (TOG)*, **23** (3): 457–462.

Mandre, S. and Brenner, M. P. (2012). The mechanism of a splash on a dry solid surface. *Journal of Fluid Mechanics*, **690**: 148–172.

Mani, M., Mandre, S., and Brenner, M. P. (2010). Events before droplet splashing on a solid surface. *Journal of Fluid Mechanics*, **647**: 163–185.

Marston, J., Thoroddsen, S. T., Ng, W., and Tan, R. (2010). Experimental study of liquid drop impact onto a powder surface. *Powder Technology*.

Marston, J. O., Li, E. Q., and Thoroddsen, S. T. (2012a). Evolution of fluid-like granular ejecta generated by sphere impact. *Journal of Fluid Mechanics*, **704**: 5–36.

Marston, J. O., Zhu, Y., Vakarelski, I. U., and Thoroddsen, S. T. (2012b). Deformed liquid marbles: Freezing drop oscillations with powders. *Powder Technology*, **228**: 424–428.

Martin, G. D., Hoath, S. D., and Hutchings, I. M. (2008). Inkjet printing - the physics of manipulating liquid jets and drops. *Journal of Physics: Conference Series*, **105**: 012001.

Mehdi-Nejad, V., Mostaghimi, J., and Chandra, S. (2003). Air bubble entrapment under an impacting droplet. *Physics of Fluids*, **15** (1): 173–183.

Michalak, T. E., Yerkes, K. L., Thomas, S. K., and McQuillen, J. B. (2010). Acceleration Effects on the Cooling Performance of a Partially Confined FC-72 Spray. *Journal of Thermophysics and Heat Transfer*, **24** (3): 463–479.

Mills, B. H., Saylor, J. R., and Testik, F. Y. (2012). An experimental study of Mesler entrainment on a surfactant-covered interface: The effect of drop shape and Weber number. *AIChE Journal*, **58** (1): 46–58.

Moreira, A., Moita, A., and Panão, M. (2010). Advances and challenges in explaining fuel spray impingement: How much of single droplet impact research is useful? *Progress in Energy and Combustion Science*, **36** (5): 554–580.

Morton, D., Rudman, M., and Liow, J.-L. (2000). An investigation of the flow regimes resulting from splashing drops. *Physics of Fluids*, **12** (4): 747.

Mundo, C., Sommerfeld, M., and Tropea, C. (1995). Droplet-wall collisions: Experimental studies of the deformation and breakup process. *International Journal of Multiphase Flow*, **21** (2): 151–173.

Neitzel, G. P. and Dell'Aversana, P. (2002). Noncoalescence and nonwetting behavior of liquids. *Annual Review of Fluid Mechanics*, **34**: 267–289.

Noh, W. F. and Woodward, P. (1976). SLIC (Simple Line Interface Calculation). In *Proceedings of the Fifth International Conference on Numerical Methods in Fluid Dynamics*, **59**: 330–340, Enschede, The Netherlands. Springer, Berlin.

Oguz, H. N. and Prosperetti, A. (1989). Surface-tension effects in the contact of liquid surfaces. *Journal of Fluid Mechanics*, **203**: 149–171.

Oguz, H. N. and Prosperetti, A. (1990). Bubble entrainment by the impact of drops on liquid surfaces. *Journal of Fluid Mechanics*, **219**: 143–179.

Ootsuka, N., Etoh, T. G., Takehara, K., Oki, S., Takano, Y., Hatsuki, Y., and Thoroddsen, S. T. (2005). Air-bubble entrapment due to a drop. In *26th International Congress on High-Speed Photography and Photonics*, **5580** (1): 153–162, Alexandria, VA, USA. SPIE.

Palacios, J., Hernández, J., Gómez, P., Zanzi, C., and López, J. (2012). On the impact of viscous drops onto dry smooth surfaces. *Experiments in Fluids*, **52** (6): 1449–1463.

Peck, B. and Sigurdson, L. (1994). The three-dimensional vortex structure of an impacting water drop. *Physics of Fluids*, **6** (2): 564–576.

Peregrine, D. H. (1981). The fascination of fluid mechanics. *Journal of Fluid Mechanics*, **106**: 59–80.

Popinet, S. (2003). Gerris: a tree-based adaptive solver for the incompressible Euler equations in complex geometries. *Journal of Computational Physics*, **190** (2): 572–600.

Popinet, S. (2009). An accurate adaptive solver for surface-tension-driven interfacial flows. *Journal of Computational Physics*, **228** (16): 5838–5866.

Popinet, S. (2011). Gerris flow solver. http://gfs.sf.net.

Prosperetti, A. and Oguz, H. N. (1993). The Impact of Drops on Liquid Surfaces and the Underwater Noise of Rain. *Annual Review of Fluid Mechanics*, **25** (1): 577–602.

Pumphrey, H. C., Crum, L. A., and Bjø rnø, L. (1989). Underwater sound produced by individual drop impacts and rainfall. *The Journal of the Acoustical Society of America*, **85** (4): 1518–1526.

Pumphrey, H. C. and Elmore, P. A. (1990). The entrainment of bubbles by drop impacts. *Journal of Fluid Mechanics*, **220**: 539–567.

Rayleigh, L. (1879). On the capillary phenomena of jets. *Proceedings of the Royal Society of London*, **29** (196-199): 71–97.

Rein, M. (1993). Phenomena of liquid drop impact on solid and liquid surfaces. *Fluid Dynamics Research*, **12** (2): 61–93.

Reiter, G. and Sharma, A. (2001). Auto-Optimization of Dewetting Rates by Rim Instabilities in Slipping Polymer Films. *Physical Review Letters*, **87** (16): 166103.

Reyssat, E. and Quéré, D. (2006). Bursting of a fluid film in a viscous environment. *Europhysics Letters (EPL)*, **76** (2): 236–242.

Rieber, M. and Frohn, A. (1999). A numerical study on the mechanism of splashing. *International Journal of Heat and Fluid Flow*, **20** (5): 455–461.

Rioboo, R., Tropea, C., and Marengo, M. (2001). Outcomes from a drop impact on solid surfaces. *Atomization and Sprays*, **11** (2): 155–165.

Roisman, I., Gambaryan-Roisman, T., Kyriopoulos, O., Stephan, P., and Tropea, C. (2007). Breakup and atomization of a stretching crown. *Physical Review E*, **76** (2): 026302.

Roisman, I. V., Horvat, K., and Tropea, C. (2006). Spray impact: Rim transverse instability initiating fingering and splash, and description of a secondary spray. *Physics of Fluids*, **18** (10): 102104.

Rosenthal, D. K. (1962). The shape and stability of a bubble at the axis of a rotating liquid. *Journal of Fluid Mechanics*, **12** (3): 358–366.

Sawan, M. E. and Carbon, M. W. (1975). A review of spray-cooling and bottom-flooding work for lwr cores. *Nuclear Engineering and Design*, **32** (2): 191–207.

Saylor, J. R. and Bounds, G. D. (2012). Experimental Study of the Role of the Weber and Capillary Numbers on Mesler Entrainment. *AIChE Journal*, **58** (12): 3841–3851.

Saylor, J. R. and Grizzard, N. K. (2004). The optimal drop shape for vortices generated by drop impacts: the effect of surfactants on the drop surface. *Experiments in Fluids*, **36** (5): 783–790.

Scardovelli, R. and Zaleski, S. (1999). Direct numerical simulation of free-surface and interfacial flow. *Annual Review of Fluid Mechanics*, **31** (1): 567–603.

Sigler, J. and Mesler, R. (1990). The behavior of the gas film formed upon drop impact with a liquid surface. *Journal of Colloid and Interface Science*, **134** (2): 459–474.

Smith, F. T., Li, L., and Wu, G. X. (2003). Air cushioning with a lubrication/inviscid balance. *Journal of Fluid Mechanics*, **482**: 291–318.

Song, M. and Tryggvason, G. (1999). The formation of thick borders on an initially stationary fluid sheet. *Physics of Fluids*, **11** (9): 2487–2493.

Stow, C. D. and Hadfield, M. G. (1981). An Experimental Investigation of Fluid Flow Resulting from the Impact of a Water Drop with an Unyielding Dry Surface. *Proceedings of the Royal Society A: Mathematical, Physical and Engineering Sciences*, **373** (1755): 419–441.

Tatebe, O. (1993). The Multigrid Preconditioned Conjugate Gradient Method. In *6th Copper Mountain Conference on Multigrid Methods*, 621–634, Copper Mountain, Colorado (USA). NASA.

Taylor, G. (1959a). The Dynamics of Thin Sheets of Fluid. II. Waves on Fluid Sheets. *Proceedings of the Royal Society A: Mathematical, Physical and Engineering Sciences*, **253** (1274): 296–312.

Taylor, G. (1959b). The Dynamics of Thin Sheets of Fluid. III. Disintegration of Fluid Sheets. *Proceedings of the Royal Society A: Mathematical, Physical and Engineering Sciences*, **253** (1274): 313–321.

Thomson, J. J. and Newall, H. F. (1885). On the Formation of Vortex Rings by Drops Falling into Liquids, and Some Allied Phenomena. *Proceedings of the Royal Society of London*, **39** (239-241): 417–436.

Thoraval, M.-J., Takehara, K., Etoh, T. G., Popinet, S., Ray, P., Josserand, C., Zaleski, S., and Thoroddsen, S. T. (2012a). Drop impact: From bumping to irregular splashing. In *9th European Fluid Mechanics Conference (EFMC9)*, talk 0431, Rome, Italy. Euromech.

Thoraval, M.-J., Takehara, K., Etoh, T. G., Popinet, S., Ray, P., Josserand, C., Zaleski, S., and Thoroddsen, S. T. (2012b). von Kármán Vortex Street within an Impacting Drop. *Physical Review Letters*, **108** (26): 264506, arXiv:1202.6569.

Thoraval, M.-J., Takehara, K., Etoh, T. G., and Thoroddsen, S. T. (2013a). Drop impact entrapment of bubble rings. *Journal of Fluid Mechanics*, **724**: 234–258, arXiv:1211.3076.

Thoraval, M.-J., Takehara, K., Etoh, T. G., and Thoroddsen, S. T. (2013b). FLM volume 724 issue 1 Cover and Front matter. *Journal of Fluid Mechanics*, **724**: f1–f4.

Thoraval, M.-J. and Thoroddsen, S. T. (2010). Dynamics of the ejecta sheets generated by a drop impact. In *63rd Annual Meeting of the APS Division of Fluid Dynamics*, **55** (16): talk HR.00009, Long Beach, California, USA.

Thoraval, M.-J. and Thoroddsen, S. T. (2011). Ejecta sheet dynamics. In *KAUST Graduate Research Symposium*, poster. KAUST, Thuwal, Saudi Arabia.

Thoraval, M.-J., Thoroddsen, S. T., Takehara, K., and Etoh, T. G. (2012c). Bubble Rings Entrapment. In *Video submission to the Gallery of Fluid Motion APS DFD 2012*. arXiv:1210.3836.

Thoraval, M.-J., Thoroddsen, S. T., Takehara, K., and Etoh, T. G. (2012d). Toroidal bubble entrapment under an impacting drop. In *65th Annual Meeting of the APS Division of Fluid Dynamics*, **57** (17): talk G4.00002, San Diego, California, USA. APS.

Thoraval, M.-J., Thoroddsen, S. T., Takehara, K., Etoh, T. G., Ray, P., Josserand, C., and Zaleski, S. (2011). Drop interaction with the ejecta sheet. In *64th Annual Meeting of the APS Division of Fluid Dynamics*, **56** (18): talk S5.00008, Baltimore, Maryland, USA.

Thornton, J. (2006). Directable simulation of stylized water splash effects in 3d space. In *ACM SIGGRAPH 2006 Sketches*, 94.

Thoroddsen, S., Thoraval, M.-J., Takehara, K., and Etoh, T. G. (2012a). The breakup of thin air films caught under impacting drops. In *65th Annual Meeting of the APS Division of Fluid Dynamics*, **57** (17): talk G4.00001, San Diego, California, USA. APS.

Thoroddsen, S. T. (2002). The ejecta sheet generated by the impact of a drop. *Journal of Fluid Mechanics*, **451**: 373–381.

Thoroddsen, S. T., Etoh, T. G., and Takehara, K. (2003). Air entrapment under an impacting drop. *Journal of Fluid Mechanics*, **478**: 125–134.

Thoroddsen, S. T., Etoh, T. G., and Takehara, K. (2007). Microjetting from wave focusing on oscillating drops. *Physics of Fluids*, **19** (5): 052101.

Thoroddsen, S. T., Etoh, T. G., and Takehara, K. (2008). High-Speed Imaging of Drops and Bubbles. *Annual Review of Fluid Mechanics*, **40**: 257–285.

Thoroddsen, S. T., Etoh, T. G., Takehara, K., Ootsuka, N., and Hatsuki, Y. (2005). The air bubble entrapped under a drop impacting on a solid surface. *Journal of Fluid Mechanics*, **545**: 203–212.

Thoroddsen, S. T. and Sakakibara, J. (1998). Evolution of the fingering pattern of an impacting drop. *Physics of Fluids*, **10** (6): 1359–1374.

Thoroddsen, S. T. and Shen, A. Q. (2001). Granular jets. *Physics of Fluids*, **13** (1): 4.

Thoroddsen, S. T., Takehara, K., and Etoh, T. G. (2010). Bubble entrapment through topological change. *Physics of Fluids*, **22** (5): 051701.

Thoroddsen, S. T., Takehara, K., and Etoh, T. G. (2012b). Micro-splashing by drop impacts. *Journal of Fluid Mechanics*, **706**: 560–570.

Thoroddsen, S. T., Thoraval, M.-J., Takehara, K., and Etoh, T. G. (2011). Droplet Splashing by a Slingshot Mechanism. *Physical Review Letters*, **106** (3): 034501.

Thoroddsen, S. T., Thoraval, M.-J., Takehara, K., and Etoh, T. G. (2012c). Bubble Chandeliers. In *Video submission to the Gallery of Fluid Motion APS DFD 2012*. arXiv:1210.3837.

Thoroddsen, S. T., Thoraval, M.-J., Takehara, K., and Etoh, T. G. (2012d). FLM volume 708 issue 1 Cover and Front matter. *Journal of Fluid Mechanics*, **708**: f1–f2.

Thoroddsen, S. T., Thoraval, M.-J., Takehara, K., and Etoh, T. G. (2012e). Microbubble morphologies following drop impacts onto a pool surface. *Journal of Fluid Mechanics*, **708**: 469–479.

Thoroddsen, S. T., Thoraval, M.-J., Takehara, K., and Etoh, T. G. (2012f). Microbubbles caught under impacting drops. In *9th European Fluid Mechanics Conference (EFMC9)*, talk 0432, Rome, Italy. Euromech.

Thürey, N., Wojtan, C., Gross, M., and Turk, G. (2010). A multiscale approach to mesh-based surface tension flows. *ACM Transactions on Graphics*, **29** (4): 1.

Tryggvason, G., Scardovelli, R., and Zaleski, S. (2011). *Direct numerical simulations of gas-liquid multiphase flows*. Cambridge University Press, Cambridge, UK.

Van Dam, D. B. and Le Clerc, C. (2004). Experimental study of the impact of an ink-jet printed droplet on a solid substrate. *Physics of Fluids*, **16** (9): 3403–3414.

van der Veen, R. C. A., Tran, T., Lohse, D., and Sun, C. (2012). Direct measurements of air layer profiles under impacting droplets using high-speed color interferometry. *Physical Review E*, **85** (2): 026315.

Villermaux, E. (2007). Fragmentation. *Annual Review of Fluid Mechanics*, **39**: 419–446.

Villermaux, E. and Clanet, C. (2002). Life of a flapping liquid sheet. *Journal of Fluid Mechanics*, **462**: 341–363.

Wanninkhof, R., Asher, W. E., Ho, D. T., Sweeney, C., and McGillis, W. R. (2009). Advances in Quantifying Air-Sea Gas Exchange and Environmental Forcing. *Annual Review of Marine Science*, **1**: 213–244.

Watanabe, Y., Saeki, H., and Hosking, R. J. (2005). Three-dimensional vortex structures under breaking waves. *Journal of Fluid Mechanics*, **545**: 291–328.

Weiss, D. A. and Yarin, A. L. (1999). Single drop impact onto liquid films: neck distortion, jetting, tiny bubble entrainment, and crown formation. *Journal of Fluid Mechanics*, **385**: 229–254.

Williamson, C. and Govardhan, R. (2004). Vortex-Induced Vibrations. *Annual Review of Fluid Mechanics*, **36**: 413–455.

Williamson, C. H. K. (1988). The existence of two stages in the transition to three-dimensionality of a cylinder wake. *Physics of Fluids*, **31** (11): 3165–3168.

Williamson, C. H. K. (1992). The natural and forced formation of spot-like 'vortex dislocations' in the transition of a wake. *Journal of Fluid Mechanics*, **243**: 393–441.

Williamson, C. H. K. (1996). Vortex Dynamics in the Cylinder Wake. *Annual Review of Fluid Mechanics*, **28**: 477–539.

Wojtan, C. (2010). *Animating physical phenomena with embedded surface meshes*. Phd, Georgia Institute of Technology.

Wojtan, C., Thürey, N., Gross, M., and Turk, G. (2010). Physics-inspired topology changes for thin fluid features. *ACM Transactions on Graphics*, **29** (4): 8.

Worthington, A. M. (1876). On the Forms Assumed by Drops of Liquids Falling Vertically on a Horizontal Plate. *Proceedings of the Royal Society of London*, **25** (171-178): 261–272.

Worthington, A. M. (1877). A Second Paper on the Forms Assumed by Drops of Liquids Falling Vertically on a Horizontal Plate. *Proceedings of the Royal Society of London*, **25** (171-178): 498–503.

Worthington, A. M. (1882). On Impact with a Liquid Surface. *Proceedings of the Royal Society of London*, **34** (220-223): 217–230.

Worthington, A. M. (1895). *The splash of a drop*. London.

Worthington, A. M. (1908). *A study of splashes*. Longmans, Green, and co.

Xu, L., Zhang, W. W., and Nagel, S. R. (2005). Drop Splashing on a Dry Smooth Surface. *Physical Review Letters*, **94** (18): 184505.

Yarin, A. L. (2006). Drop Impact Dynamics: Splashing, Spreading, Receding, Bouncing... *Annual Review of Fluid Mechanics*, **38**: 159–192.

Yokoi, K. (2008). A Numerical Method for Free-Surface Flows and Its Application to Droplet Impact on a Thin Liquid Layer. *Journal of Scientific Computing*, **35** (2-3): 372–396.

Yokoi, K. (2011). Numerical studies of droplet splashing on a dry surface: triggering a splash with the dynamic contact angle. *Soft Matter*, **7** (11): 5120–5123.

Yokoi, K. (2013). A practical numerical framework for free surface flows based on CLSVOF method, multi-moment methods and density-scaled CSF model: Numerical simulations of droplet splashing. *Journal of Computational Physics*, **232** (1): 252–271.

Yu, D. and Tryggvason, G. (1990). The free-surface signature of unsteady, two-dimensional vortex flows. *Journal of Fluid Mechanics*, **218**: 547–572.

Yu, J., Wojtan, C., Turk, G., and Yap, C. (2012). Explicit Mesh Surfaces for Particle Based Fluids. *Computer Graphics Forum*, **31** (2pt4): 815–824.

Zhang, L. V., Brunet, P., Eggers, J., and Deegan, R. D. (2010). Wavelength selection in the crown splash. *Physics of Fluids*, **22** (12): 122105.

Zhang, L. V., Toole, J., Fezzaa, K., and Deegan, R. D. (2012). Evolution of the ejecta sheet from the impact of a drop with a deep pool. *Journal of Fluid Mechanics*, **690**: 5–15.

Appendices

Appendix A

Numerical Simulations

Abstract

Drop impact is a standard example of multiphase flow simulations, due to its geometric simplicity, the beauty of its outcomes and the numerous applications (See Chapter 1). It is however a very challenging problem, due to the presence of the interface, surface tension effects, topological changes, and the very fine features involved compared to the drop diameter. These include air entrapment and splashing, that are the focus of this thesis.

Herein, we perform axisymmetric numerical simulations using the open source code Gerris. This code uses a volume-of-fluid technique. Extreme adaptive grid refinement allowed us to reach enough precision to fully resolve the fine details of the ejecta.

A.1 Introduction

The first numerical studies of drop impacts looked at the large deformations of the drop, at time scales larger than 1 ($t^* = t/\tau > 1$, where $\tau = D/U$) (Harlow and Shannon, 1967a,b, Foote, 1975). This included the formation of the crown splash, the cavity dynamics and the formation of the Worthington jet. With the improvement of the numerical methods, finer phenomena were captured, such as the vortex rings, air entrapment and splashing (Oguz and Prosperetti, 1989, 1990, Pumphrey and Elmore, 1990, Morton et al., 2000). More information about the numerical techniques and progress can be found in the reviews of Prosperetti and Oguz (1993), Rein (1993), Yarin (2006), and the book of Tryggvason et al. (2011), with a focus on drop impacts in their Chapter 10.

Recently, a much finer and earlier feature ($t^* < 1$) was identified for high impact velocities: the ejecta sheet. It emerges horizontally in the neck between the drop and the pool, and then rises to give way to the crown. It was first suggested by inviscid simulations of Weiss and Yarin (1999), and confirmed by experimental results of Thoroddsen (2002), and direct numerical simulations of Josserand and Zaleski (2003).

However, none of the previous numerical simulations were able to reproduce the very complex ejecta shapes observed experimentally (see Thoroddsen (2002) and Fig. 8 of Thoroddsen et al. (2008)). This is principally due to their extreme thinness. Our experimental observations have indeed shown that it can become as thin as $\delta = 300$ nm (see Chapter 2), corresponding to $D/\delta \simeq 15\,000$. The maximum resolution of Josserand and Zaleski (2003) had $D/\Delta x = 150$ cells per drop diameter, thus being a factor of a 100 away from this scale. As their maximum Reynolds number studied was 1000, they did not look at the intermediate regimes observed experimentally in Fig. 3.2. The more recent study of Coppola et al. (2011) went up to 1200 cells/D and $Re = 5000$, but did not reproduce the experimental

observations.

Some 3D simulations have also been done (Gueyffier and Zaleski, 1998, Rieber and Frohn, 1999, Gueyffier, 2000, Agbaglah et al., 2011, Yokoi, 2008, Gomaa et al., 2009, Yokoi, 2011, 2013). Even though there is still an important gap to reach realistic 3D simulations, they were able to reproduce some of the long time dynamics.

Recent improvements in codes and the availability of computational resources now allows us sufficient resolution for the task in axisymmetric simulations. The initial goal of our study was to reproduce numerically the experimental observations of Fig. 3.2, so as to understand the transition to irregular splashing. We have chosen to use the freely available code GERRIS (Popinet, 2003, 2009, Agbaglah et al., 2011, Popinet, 2011) because of its flexibility (dynamic adaptive mesh refinement), and its high parallelization.

Here we give an overview of the numerical method used in GERRIS, and then detail the construction of the parameters that were necessary to achieve our goal.

A.2 Gerris code

A.2.1 Overview

GERRIS is a freely available code, developed by Stéphane Popinet, and supported by NIWA (National Institute of Water and Atmospheric research) and Institut Jean le Rond d'Alembert. A community of users and developers can exchange and contribute to the project around the wiki webpage: `http://gfs.sf.net`. It includes a tutorial, examples, the bibliography of papers used to develop GERRIS or studies that have used GERRIS, and connects the community through mailings lists. We give here some general information about the numerical methods used. More details can be found on Gerris in Popinet (2003, 2009), Agbaglah et al. (2011), Popinet (2011), and in Ferziger and Perić (2002), Tryggvason et al. (2011)

for general numerical methods in fluid dynamics and multiphase flows.

A.2.2 Equations

The GERRIS code solves the incompressible, variable-density, Navier-Stokes equations with surface tension:

$$\rho\left(\partial_t \mathbf{u} + \mathbf{u}\cdot\nabla\mathbf{u}\right) = -\nabla p + \nabla\cdot\left(2\mu\mathbf{D}\right) + \sigma\kappa\delta_s\mathbf{n},$$

$$\partial_t\rho + \nabla\cdot\left(\rho\mathbf{u}\right) = 0,$$

$$\nabla\cdot\mathbf{u} = 0,$$

with $\mathbf{u}$ the fluid velocity vector, $\rho = \rho(\mathbf{x}, t)$ the fluid density, $\mu = \mu(\mathbf{x}, t)$ the dynamic viscosity and $\mathbf{D}$ the deformation rate tensor defined as $D_{ij} \equiv \left(\partial_i u_j + \partial_j u_i\right)/2$. δ_s is the Dirac distribution function for the surface tension concentrated at the interface. The domain can be 2D, 3D or axisymmetric.

These equations are called a "one-fluid" formulation (Tryggvason et al., 2011, §2.5): the same equations apply in the whole domain, with variables ρ and μ, and the interface term is included by adding singular distributions. The volume fraction $c(\mathbf{x}, t)$ is used to define the local density and viscosity:

$$\rho(c) = c\rho_1 + (1-c)\rho_2, \tag{A.1}$$

$$\mu(c) = c\mu_1 + (1-c)\mu_2, \tag{A.2}$$

where the indices 1 and 2 represent each phase. The advection equation is therefore equivalent to the same equation for c.

A.2.3 Discretisation

The domain is composed of adjacent boxes, stitched together. Each box is a quadtree (octree in 3D). Spatial discretisation is done splitting the cells into two in

each directions several times. The level of refinement corresponds to the number of times this splitting is applied to reach the size of the cell. A cell at level 14 is thus about 16 000 times smaller than the box (2^{14}).

The finite volume approach is used with collocated variables at the centre of the cells. The mesh is refined dynamically in specific regions at the fractional timestep, based on flexible user defined conditions (Popinet, 2003). This allows for instance to keep the finest refinement near the interface, or in regions of high vorticity (see §A.4). A uniform mesh at level 16 in 2D or axisymmetric domain would have more than 4 billion cells [$(2^{16})^2$], while our simulation at this level have of the order of 20 million cells.

For simplicity in the code, the level of neighbouring cells cannot differ by more than one. This applies for side and diagonal neighbouring cells.

The scheme to solve the equation is second order in time and space. A classical time splitting projection method leads to the resolution of a Poisson equation. A multigrid Poisson solver is described in Popinet (2003) for the quad/octree data structure of Gerris.

A.2.4 *Volume of Fluid* method

The interface is advected by a *Volume of Fluid* method DeBar (1974), Noh and Woodward (1976), Hirt and Nichols (1981), with a Piecewise Linear Interface Calculation (PLIC) reconstruction (Scardovelli and Zaleski, 1999, Popinet, 2009). This reconstructed interface is then used to estimate the curvature, used by the surface tension term. The interface topology changes thus occur naturally whenever interfaces become closer than one cell. The drawback is that it depends on the size of the cells, and doesn't capture the physical mechanisms involved in these events. It is found however, that as the effects of topology changes are limited in space and time, they do not affect much the overall evolution, provided that the typical scale of the surrounding features are well captured.

A.2.5 Spatial filtering

As we are simulating drop impacts with experimental parameters similar to those in Figure 3.2, we have very large density ratios. This is known to cause a slow convergence of the multi-grid Poisson solver (Alcouffe et al., 1981, Tatebe, 1993, Chan and W. L. Wan, 2000, Tryggvason et al., 2011). Smoothing the interface by a spatial filter can significantly improve this issue (Popinet, 2009, Fuster, 2013). This is done by replacing $c(\mathbf{x}, t)$ in Equations A.1 and A.2, by $\tilde{c}(\mathbf{x}, t)$ which is the filtered volume fraction. The spatial filtering takes the average of the four corners (eight corners in 3D) values of each cell. These corner values are an average of the cells around the corner.

Therefore, applying the filter once (called filter 1 here for simplicity) smoothes the interface properties over three cells instead of just one without the filter (one more cell in each direction around the interface). Each additional time the filter is applied, the thickness of the interface grows by 2 cells. Cells further away from the interface are less affected.

However, it also affects the accuracy of the solution by smearing the physical properties around the interface. We have found that applying only one iteration of the filtering operator gave the best results for our study (see §A.3).

A.2.6 Parallelization

The parallelization of the Gerris code is detailed in Agbaglah et al. (2011). The domain is divided into smaller boxes, having the same quad/octrees structure, and the same size. This can be done manually in the parameter file, or automatically by a command splitting the domain (see §A.4). They are then grouped to form a partition of sub-domains, each containing several boxes stitched together. Sub-domains can be run on different processors. The communication between processors is treated as boundary conditions. It creates a ghost layer at the parallel

boundaries, and swaps the values in the ghost cells sharing the same boundary using the MPI library (Message Passing Interface).

The minimum number of boxes and sub-domains required is therefore the number of processors used. However, the adaptive mesh refinement (AMR) leads to an uneven distribution of computational load into the domain. Since this is done dynamically during the computation, the regions with higher requirements will change in time. Good scalability is insured by a load-balancing algorithm. It redistributes boxes between sub-domains to optimize the load balance and communication between processors. This implies that the number of boxes has to be much larger than the number of processors. Another constraint is that each box has to be larger than the coarsest cells in the domain.

We follow the balancing procedure described in Agbaglah et al. (2011, p. 200). The load balancing algorithm is applied at every time step, only if the difference between the maximum and minimum number of elements per processor is larger than 10%.

A.2.7 Post-processing

An interactive graphical interface has been developed for the specific data structure of Gerris: GfsView. It takes advantage of the quad/octree structure to allow fast visualization of the results. It also includes a parallel batch processing to output selected information or images, during or after the computation, using saved gfs files.

To obtain a smoother interface profile, we use the volume fraction tracer T=0.5-isoline, instead of the VOF PLIC reconstruction (Piecewise Linear Interface Calculation).

The output data generated was then analysed with Bash and Octave scripts (see for instance Fig. 3.4).

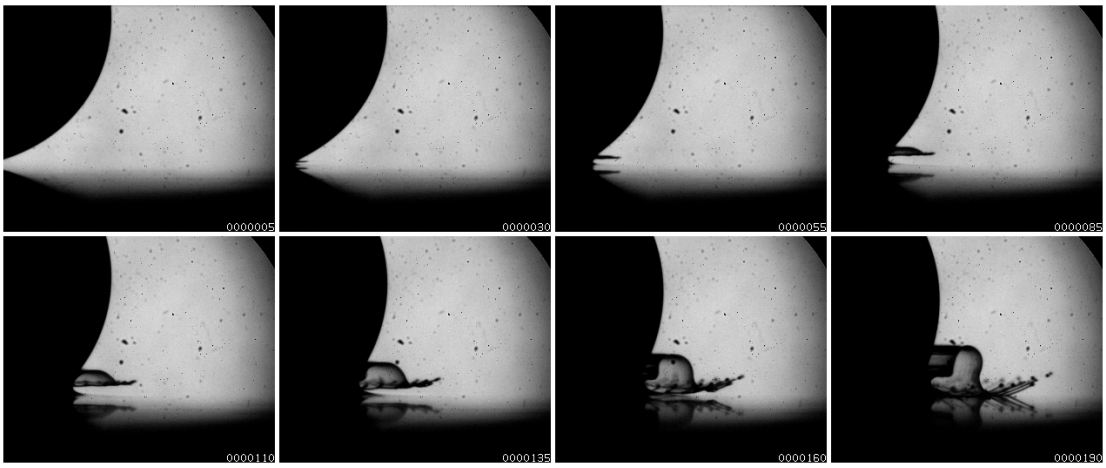

Figure A.1: Experimental observation at times [-5, 20, 45, 75, 100, 125, 150, 180] μs from left to right and top to bottom, for the same experiment as in Figure 3.3(a). The non-dimensional times of those frames are [-0.43, 1.74, 3.91, 6.52, 8.70, 10.87, 13.04, 15.65].

A.3 Building the simulation file

A.3.1 Choice of a test case

As a simulation convergence test, we have chosen to reproduce numerically the drop impact for conditions similar to Fig. 3.3, as it is one of the key experimental observations in the transition to irregular splashing. We show in Fig. A.1 a larger view of the experiment in Figure 3.3(a). Times have been chosen to be the closest to Gerris simulations presented in Fig. A.6.

This bumping case also represents an interest numerically because it involves several interface reconnections. Connecting two interfaces is difficult numerically, because of the large local divergence created. The first challenge thus occurs at the first contact between the drop and the pool. The bumping adds another difficulty to the computation, because the ejecta sheet reconnects with the drop. In some cases, the solver was not able to converge when reaching these topological changes.

The drop does not connect with the pool on the axis of symmetry, but rather on a circular line, thus entrapping a thin air disk, which subsequently contracts into

a bubble. This central air entrapment has received a lot of interest (Thoroddsen and Sakakibara, 1998, Thoroddsen et al., 2003, Smith et al., 2003, Mehdi-Nejad et al., 2003, Van Dam and Le Clerc, 2004, Thoroddsen et al., 2005, Mani et al., 2010, Hicks and Purvis, 2010, 2011, 2012, Driscoll and Nagel, 2011, Duchemin and Josserand, 2011, 2012, Palacios et al., 2012, de Ruiter et al., 2012, Mandre and Brenner, 2012, Kolinski et al., 2012, van der Veen et al., 2012, Liu et al., 2013). However, previous numerical studies of drop impacts usually ignore it, by starting the simulation when the drop has already contacted the pool (Weiss and Yarin, 1999, Davidson, 2002, Josserand and Zaleski, 2003, Coppola et al., 2011). For boundary integral methods used by Weiss and Yarin (1999), Davidson (2002), this is a necessary condition, as they cannot handle any changes in interface topology.

Our simulations start before contact between the drop and the pool (Fig. A.2), thus capturing the air-cushioning effect [Figs. 3.7(d), 3.5(a), and 3.5(d)].

We have observed that using spatial filtering helps the computation to overcome the difficulties of topology changes. However, this also alters the local properties of the fluids around the interface. In this section, we will show the effects of the maximum level of refinement, and the spatial filtering. This will lead us to the parameters chosen for our numerical studies, presented in §A.4.

A.3.2 Physical parameters

We have chosen impact parameters close to the experiment presented in Figure 3.3(a). The physical parameters and their non-dimensional counterparts in Gerris are listed in Table A.1. This experiment has thus the following non-dimensional numbers:

$$Re = 3.64 \cdot 10^3 \qquad \frac{\rho_{liquid}}{\rho_{air}} = 926$$

$$We = 1.22 \cdot 10^3 \qquad \frac{\mu_{liquid}}{\mu_{air}} = 313$$

$$K = We\sqrt{Re} = 7.38 \cdot 10^4$$

All times used below are non-dimensionalized by $\tau = D/U = 1.15$ ms. The

	Experimental parameters	Numerical simulation parameters
U	4 m/s	1
D	4.6 mm	0.44
$L = L_x = L_z$	10.45 mm	1
H	5 mm	0.478
δ	0.23 mm	0.022
ρ_{liquid}	1120 kg/m^3	1
μ_{liquid}	5.66 cP	$1.21 \cdot 10^{-4}$
ρ_{air}	1.21 kg/m^3	$1.08 \cdot 10^{-3}$
μ_{air}	$1.81 \cdot 10^{-2}$ cP	$3.86 \cdot 10^{-7}$
σ	67.4 mN/m	$3.60 \cdot 10^{-4}$
g	9.81 m/s^2	$6.41 \cdot 10^{-3}$
$\tau_G = L/U$	2.61 ms	1

Table A.1: Experimental and numerical simulation parameters. In GERRIS, space is adimensionalized by L instead of D. Non-dimensional units used in the study can be obtained from the GERRIS units by dividing space and time by 0.44 ($\tau = 0.44\ \tau_G$).

origin of time is the theoretical contact time between the drop and the pool if the surface were not deformed. The time can thus be expressed in percentage of the time required for the undisturbed drop to enter the pool if it kept the same velocity. In the experiment, the bumping (impact of the ejecta sheet on the drop) occurs at about 10% of drop entry.

A.3.3 Computational domain and refinement

All simulations use the axisymmetric configuration of GERRIS. The simulation domain is described in Figure A.2. The liquid in the drop has an initial velocity U towards the pool, while the pool liquid and the gas are initially stationary. The boundary conditions are described in the last paragraph of the parameter file (§A.4). It is an open flow boundary condition on the top of the domain (GfsBoundaryOutflow), and a wall no-slip boundary condition on the side and bottom of the domain (Boundary { BcDirichlet U 0 BcDirichlet V 0 }). The default boundary condition for the pressure is used on all boundaries, i.e. a zero normal derivative (Popinet, 2003).

The mesh has been made uniform at the maximum level of refinement in the regions of interest: between the drop and the pool, in the neck region after impact, and inside the ejecta sheet (see §A.4). Better stability was observed with this configuration than with other local refinements (interface or curvature). This also removes possible effects of non-uniform refinement on the dynamics of the interface.

The minimum level of refinement in the domain was kept at 9, equivalent to a uniform grid of 512x512 cells. The grid was then refined dynamically based on vorticity and interface conditions. The grid was also kept uniform inside the ejecta sheet at the maximum level of refinement [Fig. A.3(c)].

A.3.4 Convergence study: maximum level of refinement

Figure A.4 shows how the bumping ejecta shapes change with increased spatial resolution of the simulations.

We can see already that a level of refinement of at least 11 ($D/\Delta x$ = 900) is

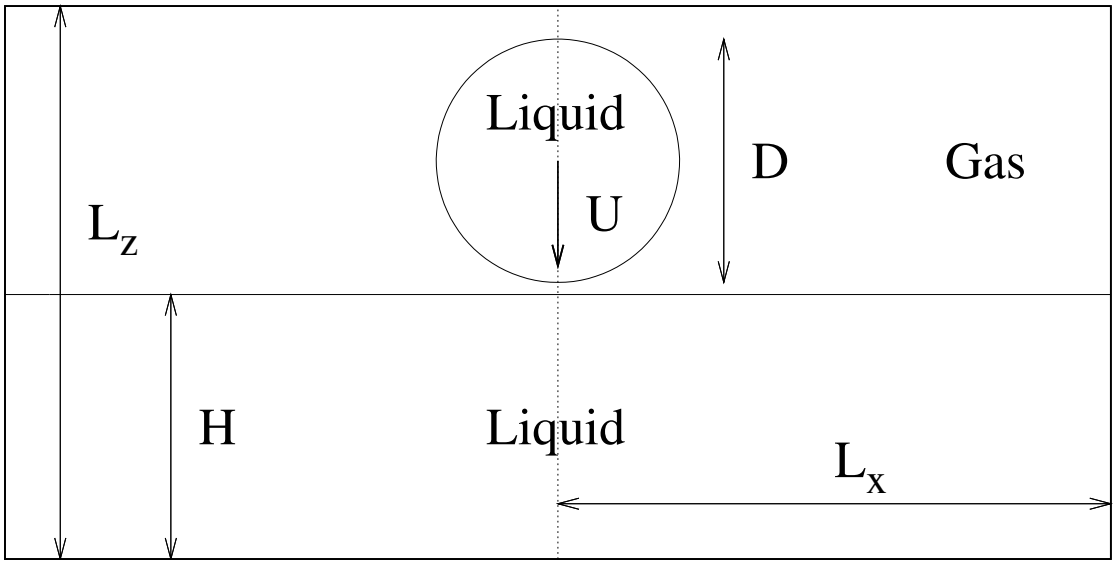

Figure A.2: Initial conditions of the GERRIS simulations. The domain of computation is limited to the right half of the domain drawn above, due to the axisymmetry. The proportions are reproduced here as in the simulations: D = 0.44, H = 0.48, $L_x = L_z$ = 1, and the initial gap between the drop and the pool is 0.022, i.e., 10% of the drop radius.

required to observe the interaction between the ejecta sheet and the drop, and 14 ($D/\Delta x$ = 7 200) to capture correctly the bumping dynamics of the ejecta sheet. This explains why previous studies could not observe these shapes.

However, differences in the dynamics are still observed up to level 16, the

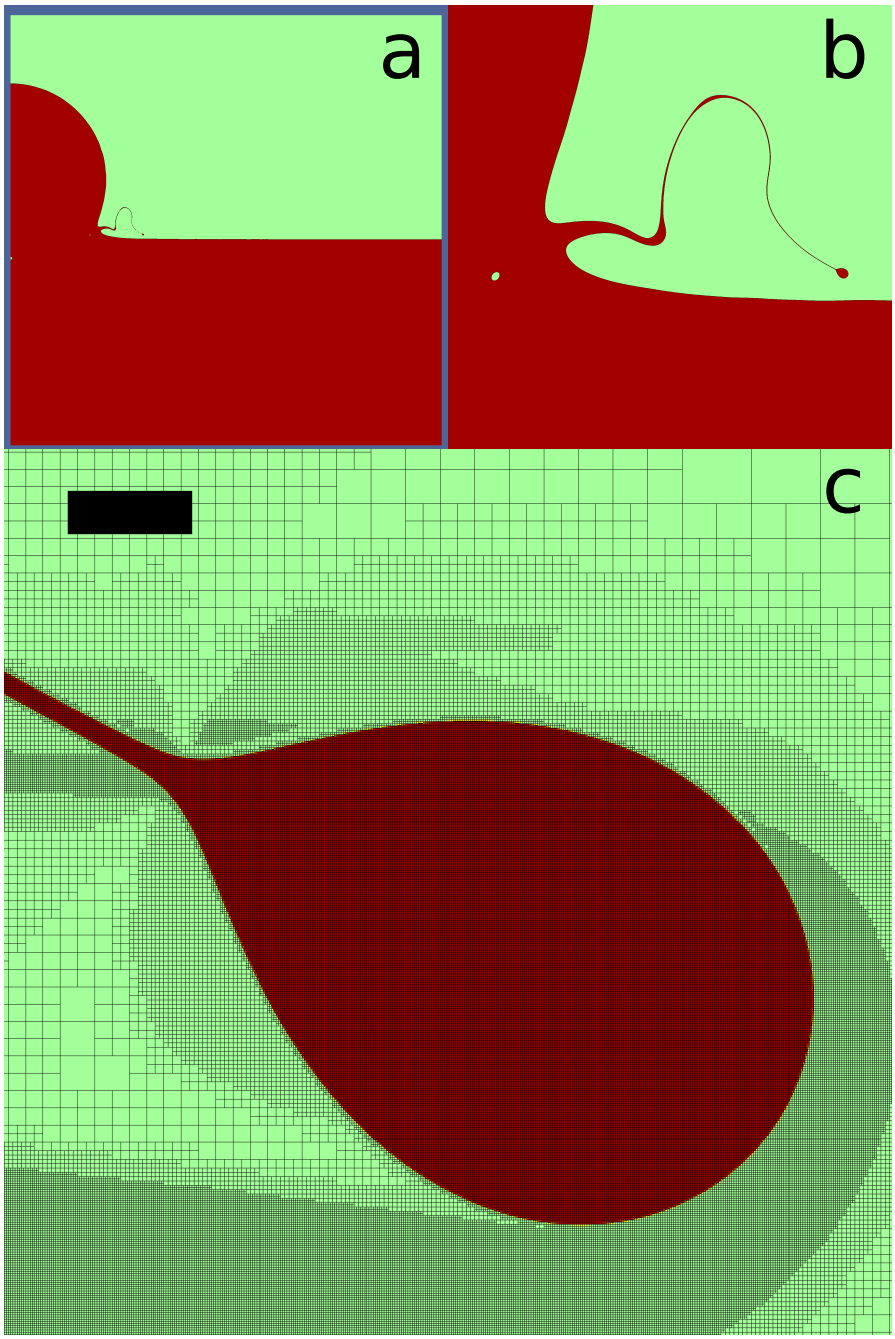

Figure A.3: (a) Overall simulation domain. (b) Zoom on the ejecta shape. (c) Typical grid near the tip of the ejecta sheet at a level 16 of refinement. The scale bar is $2 \times 10^{-3} D$ long.

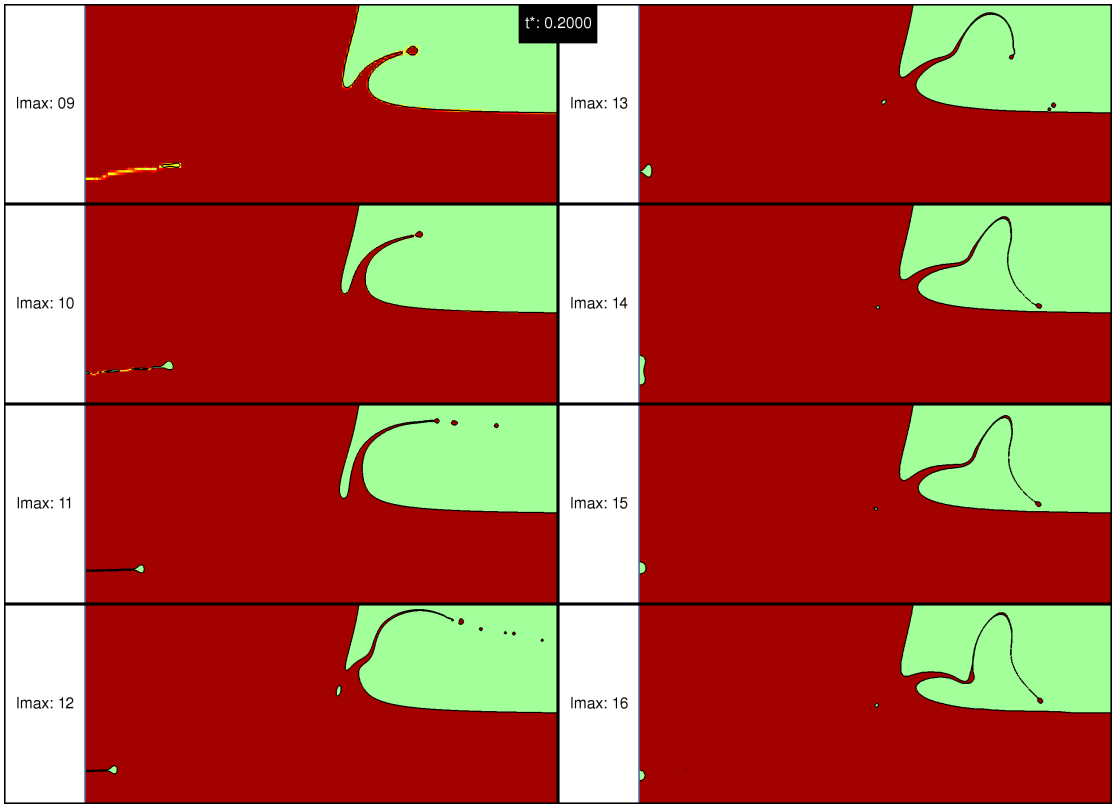

Figure A.4: Convergence study with a filter 3, in the conditions described in Table A.1, at $t^* = 0.2$. A filter 3 is used, and lmax corresponds to the maximum level of refinement.

maximum level of refinement reached in this study. It corresponds to the finest cells being $2^{16} = 65536$ times smaller than the size of the computational domain. A uniform mesh at this level of refinement would contain $2^{16} = 65536$ cells in each direction, and thus a total of $(2^{16})^2$ (4.29 billion) cells. In our simulations, this corresponds to $D/\Delta x = 28\,800$ cells per drop diameter. With a drop of diameter 4.6 mm, the smallest cell is only 160 nm, which allows to identify sub-micron structures.

At level 16 (Fig. A.3), the ejecta sheet can become as thin as 500 nm (only 3 cells) near the tip, due to the extreme stretching. This value is consistent with our indirect experimental measurements of Chapter 2. The results presented in Chapter 3 are at level 14 ($D/\Delta x = 7\,200$), calculated on 64 processors, thereby allowing a systematic investigation of the parameter space with the available computational resources.

The simulations faithfully reproduce all of the observed features, as we showed in Figure 3.3 by comparing experiments and numerics of the detailed evolution of the ejecta sheet in this bumping case. The ejecta sheet emerges smoothly between the drop and the pool and rises fast, creating a curved shape very early (Fig. A.5). Then it impacts with the drop, creating a bump in the ejecta sheet. The tip of the ejecta sheet then impacts the pool (see Chapter 2). This creates higher curvatures leading to the formation of a cusp at the top arc of the ejecta, while the outer part of the sheet is stretched between the pool and this rising cusp. The simulation shows that a toroid of air is trapped during the bumping. It also reveals the detailed mechanism leading to bumping. When the sheet hits the drop surface, the ejecta sheet changes its origin to the newly connected region. Moreover, the ejection angle drops sharply to become more horizontal. This sudden change in emergence angle creates the characteristic bumping shape.

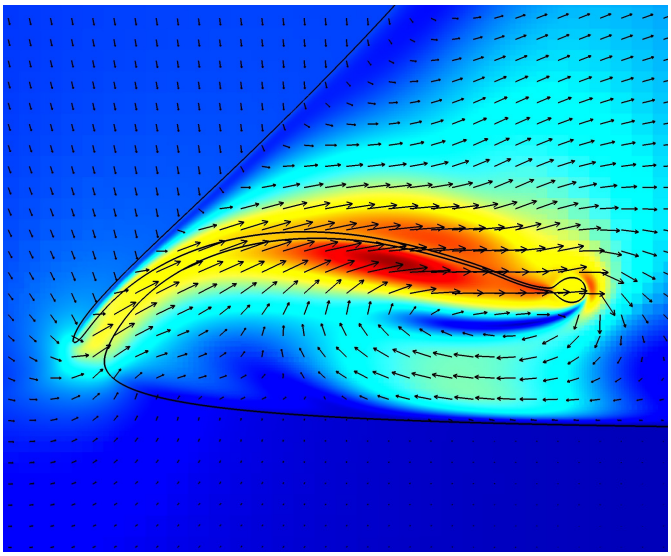

Figure A.5: Velocity field intensity (colour) and vectors, for the same conditions as Fig. 3.3. The drop is on the top left, impacting on the bottom pool. The thick line represents the air/liquid interface. We only show a limited number of velocity vectors to avoid clutter.

A.3.5 Effect of filtering

We show in Fig. A.6 the effect of applying the spatial filtering several times. We compare to the highest resolution simulations we are able to achieve. It clearly shows that the lower number of filters gives more accurate results. This is especially true for the bumping when there is a topology change on the interface: the sharp bump is smoothed by several applications of the filter.

A.3.6 First contact between the drop and the pool

More quantitatively, we can look at the early dynamics of the impact to see the effect of refinement and filtering.

The first contact is characterized in the numerical results by the tracer T=0.5-isoline. We determine that the drop has contacted with the pool when there is a change of topology of this isoline. The time of the first Gerris file saved after contact is recorded here. At this time, the contact region already has a finite radial extension. The contact radius is defined as the point at the centre of this

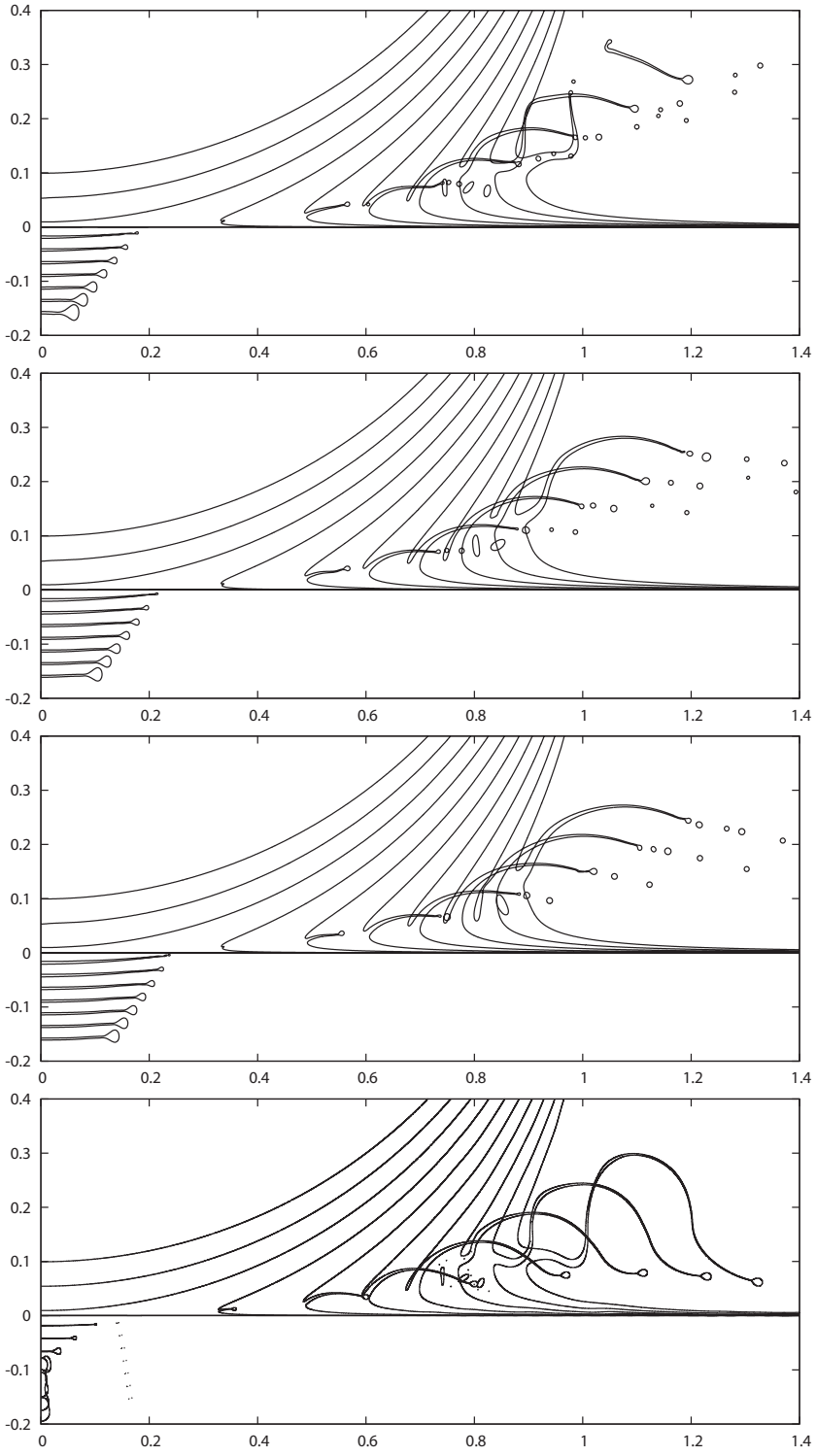

Figure A.6: Effect of filtering. Superposition of the interface profiles starting at non-dimensional time -5% of τ, by steps of $0.01/0.44 \simeq 2.27\%$: [-5.00, -2.73, -0.45, 1.82, 4.09, 6.36, 8.64, 10.91, 13.18, 15.45]. The top image has a filter 1, then 2 and 3, at a maximum level of refinement of 12 ($D/\Delta x$ = 1 800). For comparison, the bottom image shows the same simulation with a filter 3 and a maximum level of refinement of 16 ($D/\Delta x$ = 28 800).

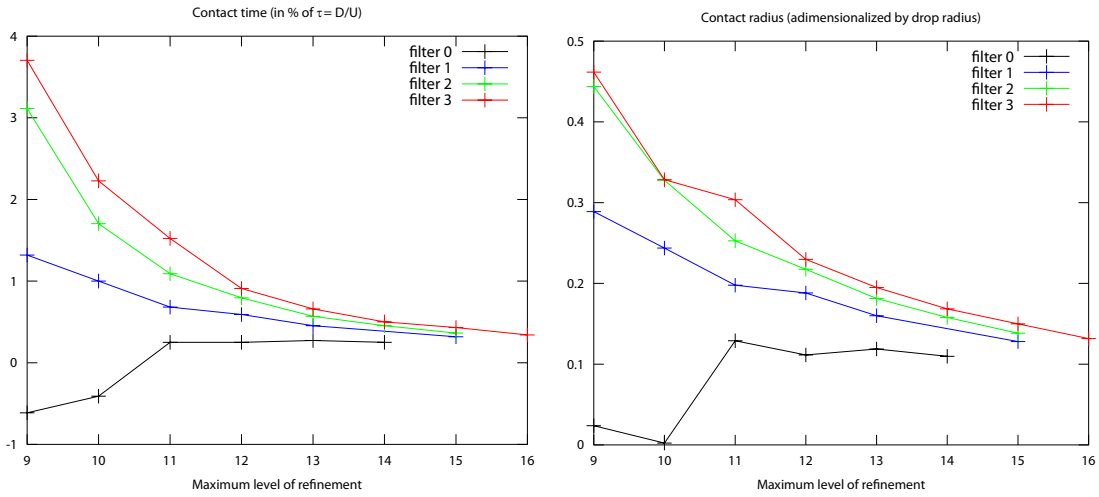

Figure A.7: Characterization of the first contact between the drop and the pool, as a function of maximum level of refinement and number of filters applied. Left: Contact time (in percentage of τ). Right: Radial position of the first contact, normalized by the drop radius.

contact region (average of the outer and inner contact points). The results are plotted in Figure A.7. They show that the filters significantly delay the contact between the drop and the pool, and increase the contact radius, with a stronger effect with more filters. This was expected, since the filter artificially increases the density and viscosity of the gas cushioning the drop. However, even for the larger number of filters, it rapidly converges towards the same value.

A.3.7 Emergence of the ejecta sheet

The emergence time of the ejecta sheet (Fig. A.8) is defined as the first time when the curvature of the T=0.5-isoline changes sign in the neck region, leading to the emergence of the ejecta sheet at later times. At this time, the tip of the ejecta sheet defines the emergence radius (Fig. A.8(top)), showing a clear convergence. The velocity at the tip (Fig. A.8(bottom)) shows that the initial stage of formation of the ejecta sheet is still not fully resolved (velocity still growing at level 16).

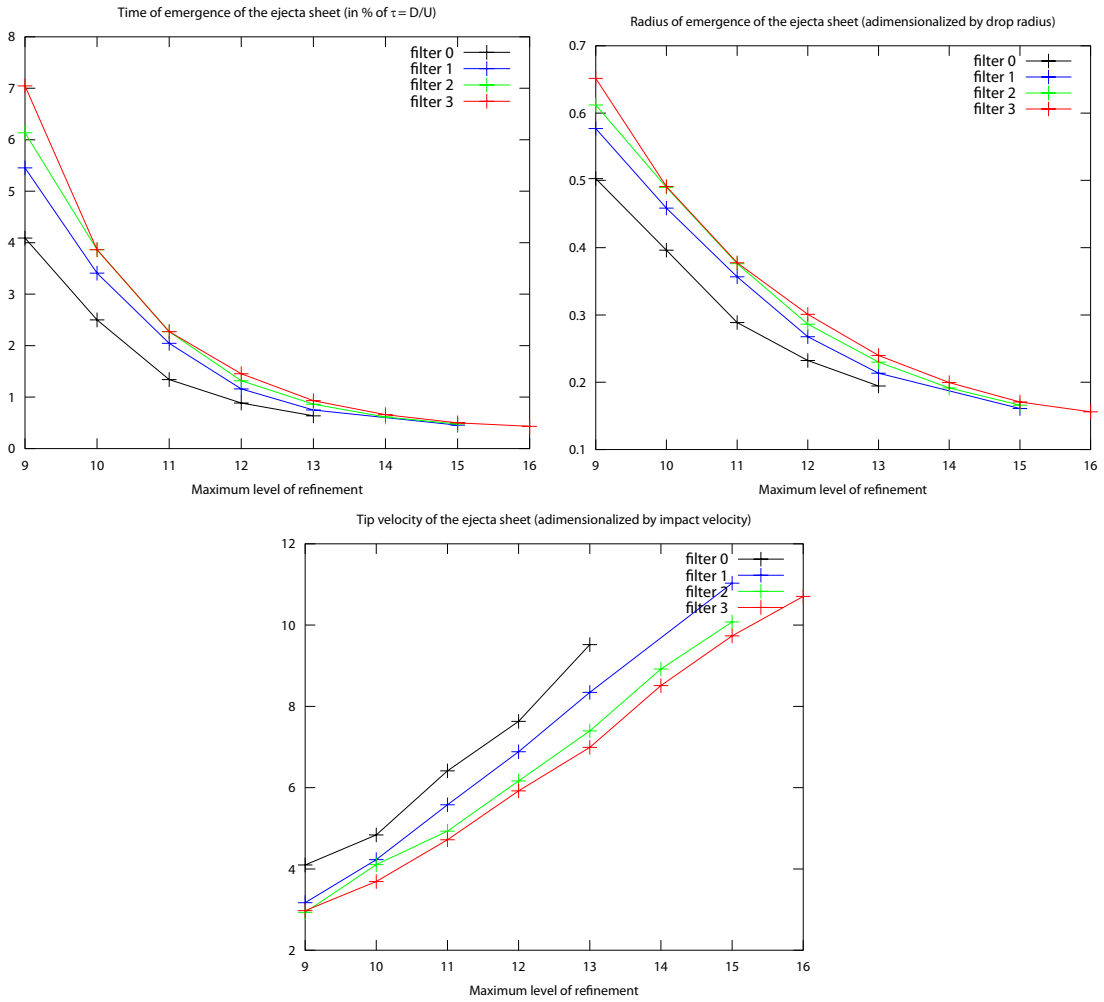

Figure A.8: Characterization of the emergence of the ejecta sheet, as a function of maximum level of refinement and number of filters applied. Top left: Time of emergence (in percentage of τ). Top right: Radius of emergence. Bottom: Tip velocity just after emergence of the ejecta sheet.

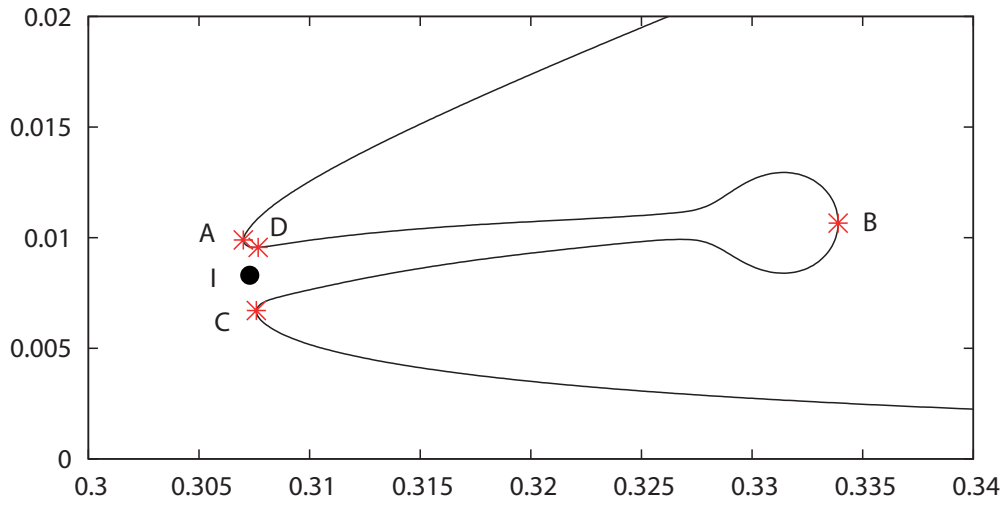

Figure A.9: Definition of the points used to characterize the ejecta sheet following Coppola et al. (2011).

A.3.8 Early evolution of the ejecta sheet

The ejecta sheet has been studied at an early stage of its evolution after emergence (at 4.09%: see Fig. A.10). We are following here the definitions of Coppola et al. (2011) for the characteristic points of the ejecta sheet. These points are represented in Figure A.9. Points A and C are at the base of the ejecta sheet, where the interface reaches a local minimum in radial location. Point B is the tip of the ejecta sheet, defined as the maximum in radial location, between A and C. I is the origin of the ejecta sheet, defined as the middle of A and C. Point D is introduced as a minimum vertical location, to identify the base of the ejecta sheet when there is no longer a minimum in radial location (later stage).

Note that a different definition of the base of the ejecta sheet was used in Chapter 3, as we were interested in the vorticity production.

The length of the ejecta sheet (Fig.A.10 (top left)) is defined as the distance between I and B. The thickness of the ejecta sheet (Fig.A.10 (top right)) is defined as the distance between A and C. The velocity of the ejecta sheet tip (Fig.A.10 (bottom left)) is the velocity at point B, and the base velocity of the ejecta sheet (Fig.A.10 (bottom right)) is the velocity at point I.

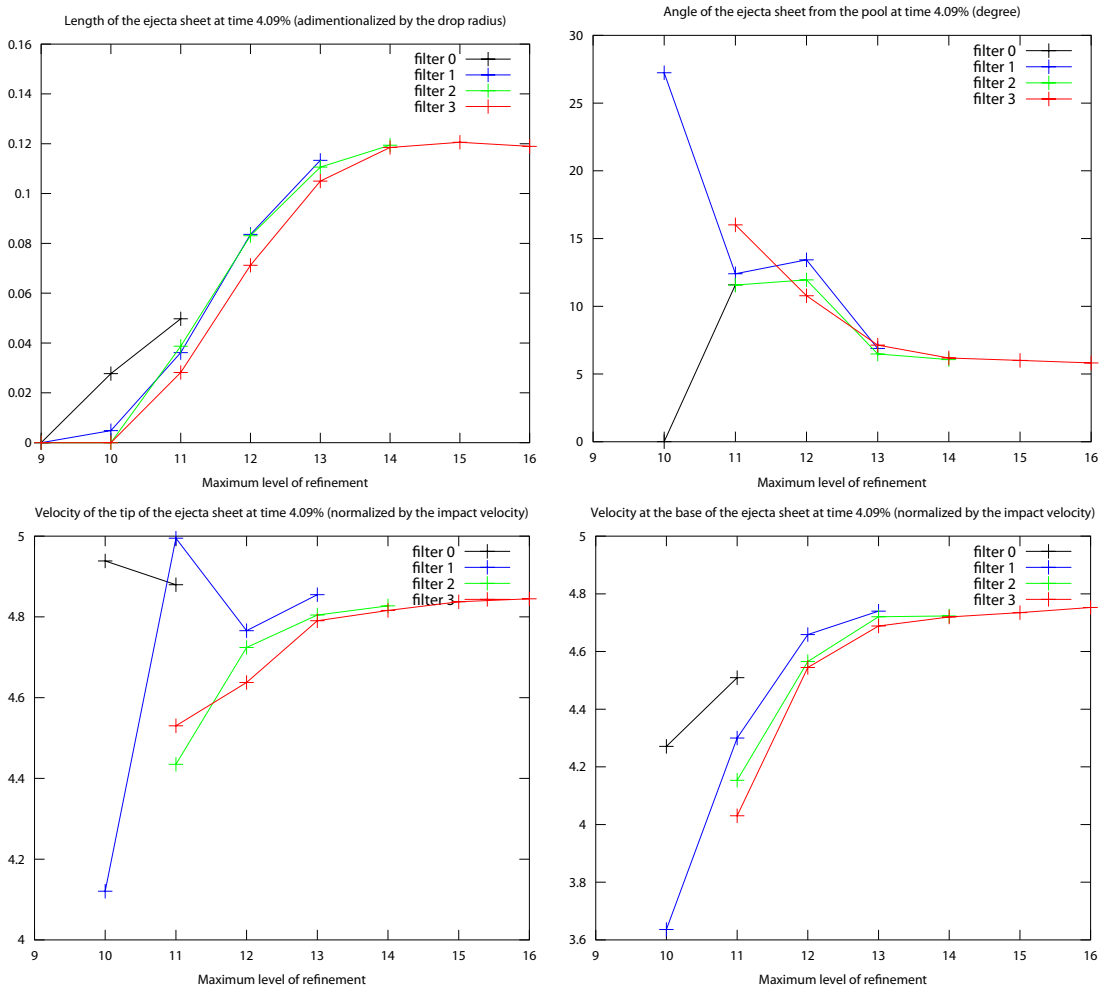

Figure A.10: Characterization of the early dynamics of the ejecta sheet, at $t^* = 4.09\%$ of τ. Top left: Length of the ejecta sheet. Top right: Thickness of the ejecta sheet. Bottom left: Velocity of the ejecta sheet tip. Bottom right: Velocity of the base of the ejecta sheet.

A.3.9 Conclusions

We see that the most accurate results are obtained for the lower number of spatial filters. However, we observe the convergence of the results by increasing the refinement even with 3 iterations of the filter.

The main effect of this filtering is to postpone the contact between approaching interfaces, thus making a softer impact. If the early characteristics of the ejecta sheet seem to be less affected by the filters, the shape of the ejecta sheet is still changing at level 16 (see Fig. A.4). The main difference in the shape is a sharper angle in the bumping at level 16. This smaller angle is probably due to the filtering, as we can see by comparing filters 1 to 3 at level 12 (Fig. A.6).

The scale at which the filter affects the results is likely not correctly captured, as it is only a few cells thick. It is therefore reasonable to use spatial filtering, keeping in mind the drawbacks. We have chosen here to use only one filter, so as to ensure convergence of the solver, while keeping the highest precision in the results. This is especially important to capture the completely new features observed in Chapter 3, where multiple topological changes occur.

This convergence test clearly shows that earlier studies had to be significantly improved to capture the dynamics of bumping, and other dynamics of Fig. 3.2.

A.4 Gerris parameter file

Gerris uses a parameter file (".gfs") as input to define all the condition of each simulation. It also contains the instructions to output information at selected time intervals. The physical parameters in the parameter file enter the equations solved as follows:

$$\frac{d\vec{u}}{dt} = \alpha\left\{-\vec{\nabla}p + \vec{\nabla}\cdot(\mu(\vec{\nabla}\vec{u} + \nabla\vec{u}^{T})) + \sigma\kappa\delta_{s}\vec{n}\right\} + \texttt{Source}\,(\vec{u})$$

where α is defined by GfsPhysicalParams, μ by GfsSourceViscosity, σ by GfsSourceTension, κ by GfsVariableCurvature, the additional source term by GfsSource, δ_s is the Dirac distribution function of the interface, and n is the normal to the interface.

The details of the numerical scheme can be found in Popinet (2009). We provide the full information necessary to reproduce our results, by adding below the GERRIS file used for this study. Its parameters correspond to the one used for Fig. 3.5(c). The domain is a square of dimension 1. To make the file run in parallel, the domain needs to be split into smaller sub-domains. The smaller boxes are generated automatically with the option -s of *Gerris*, and then grouped to partition the domain with the option -b. Each keyword is highlighted in blue, and links to the Gerris website to explain in details its effect with examples. Comments are in green, explaining the different parts of the file.

```
# Title: von Karman Vortex Street within an Impacting Drop
# File name: splash.gfs
# Description: gfs file to generate Fig. 4(c) of
#    von Karman Vortex Street within an Impacting Drop
#    PRL 108, 264506 (2012)
# Author: Marie-Jean THORAVAL - mariejean.thoraval@kaust.edu.sa
# Commands: $ gerris2D -s 7 splash.gfs > splash-s7.gfs
#           $ gerris2D -b 64 splash-s7.gfs > splash-b64.gfs
#           $ mpirun -np 64 gerris2D splash-b64.gfs
# Version: 1.3.2 (111025-074046)
# Running time: 2 weeks on 64 processors

1 0 GfsAxi GfsBox GfsGEdge {} {

Global {
/* Refinement */
#define levelmin 9
#define levelmax 14

/* Physical parameters (SI) */
#define Rho_liq 1120. /* Density liquid (kg/m^3) */
#define Mu_liq 0.0010099 /* Viscosity liquid (kg/(s.m)) */
#define Rho_air 1.21 /* Density air (kg/m^3) */
#define Mu_air 1.81e-5 /* Viscosity air (kg/(s.m)) */
#define Sig 0.0674 /* Surface tension (kg/s^2) */
#define V0 2.8422 /* Impact velocity (m/s) */
#define D 0.0046 /* Drop diameter (m) */
#define g 9.81 /* Gravity (m/s^2) */
#define PH 0.005 /* Pool depth (m) */

/* Simulation parameters */
#define radius 0.22 /* Radius of the drop in the simulation box of size 1 */
#define eps 0.001 /* Refinement away from boundary */
#define Lbox (D/(2*radius)) /* Physical size of the box (m) */
#define gad (Lbox*g/(V0*V0)) /* Gravity */
#define xccS (PH/Lbox - 0.5) /* Pool surface position */
#define xcc(t) (xccS + 1.1*radius - t) /* Drop center: 0.1*radius above the pool at t=0 */
#define ycc 0. /* Drop center */
#define goutte(x,y,t) ((x - xcc(t))*(x - xcc(t)) + (y - ycc)*(y - ycc)) /* Drop shape */
#define Quo_mu (Mu_air/Mu_liq) /* Viscosity ratio */
#define Quo_rho (Rho_air/Rho_liq) /* Density ratio */
#define VAR(T,min,max) (min + CLAMP(T,0.,1.)*(max - min)) /* Make sure T is between 0 and 1 */
#define rho(T) (VAR(T,Quo_rho,1.)) /* Density */
#define mu(T) (VAR(T,Quo_mu,1.)) /* Viscosity */
}

Time { end = 0.2 } # Gerris time TG, with t*=TG/(2*radius), t*=t/tau, tau=D/V0

# Initial refinement: refine near the pool surface
Refine {
      if ((x >= xccS - 0.003) && (x <= xccS + 0.003)) {return levelmax;}
      else {return levelmin;}
}
# Initial refinement: refine near the edge of the drop
Refine {
      if ((goutte(x,y,0) <= (radius+0.003)*(radius+0.003)) && (goutte(x,y,0) >= (radius-0.003)*(radius
     -0.003))) {return levelmax;}
      else {return levelmin;}
}

# Use different tracers to identify the liquid from the drop and the pool.
# T is the main tracer used for curvature calculations.
# Tdrop and Tpool are passive tracers.
VariableTracerVOF T
VariableTracerVOF Tdrop
```

```
65  VariableTracerVOF Tpool
66  VariableFiltered TF T 1
67  VariableCurvature K T
68  SourceTension T (Sig/(Rho_liq*Lbox*V0*V0)) K
69
70  # Initial conditions
71  InitFraction T ({
72        double drop = radius*radius - goutte(x,y,0);
73        double pool = xccS - x;
74        return -union (-drop, -pool);
75  })
76  Init {} {
77        U = ( (goutte(x,y,0) <= radius*radius) ? -1. : 0 )
78  }
79  InitFraction Tdrop ( radius*radius - goutte(x,y,0) )
80  InitFraction Tpool ( xccS - x )
81
82  Source {} U (-1.*gad)
83
84  # Main refinement
85  AdaptGradient { istep = 1 } { maxlevel = levelmax minlevel = levelmin cmax = 1e-6 } T
86  AdaptGradient { istep = 1 } { maxlevel = levelmax minlevel = levelmin cmax = 1e-6 } Tdrop
87  AdaptGradient { istep = 1 } { maxlevel = levelmax minlevel = levelmin cmax = 1e-6 } Tpool
88  AdaptVorticity { istep = 1 } { maxlevel = levelmax minlevel = levelmin cmax = 1e-2 }
89  # Ejecta sheet refinement
90  AdaptFunction { istep = 1 } { maxlevel = levelmax minlevel = levelmin cmax = 0 } ( (x > xccS+eps) && (
        goutte(x,y,t) > (radius+eps)*(radius+eps)) ? T > 0. : 0 )
91  AdaptGradient { istep = 1 } { maxlevel = levelmax minlevel = levelmin cmax = 1e-6 } ( (x > xccS+eps)
        && (goutte(x,y,t) > (radius+eps)*(radius+eps)) ? T : 0 )
92  # Contact refinement 0.1
93  AdaptFunction { istep = 1 } { maxlevel = levelmax minlevel = levelmin cmax = 0 } ( (y < 0.1) && (x >
        xccS-eps) && (goutte(x,y,t) > (radius-eps)*(radius-eps)) ? T > 0. : 0 )
94  AdaptFunction { istep = 1 start = 0.02 } { maxlevel = levelmax minlevel = levelmin cmax = 0 } ( (x >
        xccS-0.2*radius) && (x < xccS+0.2*radius) && (y < 0.1) ? T < 1. : 0 )
95  AdaptGradient { istep = 1 start = 0.02 } { maxlevel = levelmax minlevel = levelmin cmax = 1e-6 } ( (x >
        xccS-0.2*radius) && (x < xccS+0.2*radius) && (y < 0.1) ? T : 0 )
96
97  SourceViscosity { istep = 1 } (Mu_liq/(Rho_liq*Lbox*V0))*mu(TF) {
98    tolerance = 1e-07
99    nrelax    = 7
100   erelax    = 2
101   minlevel  = 0
102   nitermax  = 4000
103   nitermin  = 1
104   weighted  = 0
105   beta      = 0.5
106 }
107 PhysicalParams { alpha = 1./rho(TF) }
108 EventBalance { istep = 1 } 0.1 # Load balancing
109 RemoveDroplets { istep = 1 } T 30 (1 - T) 1 # Remove small bubbles
110 RemoveDroplets { istep = 1 } T 30 # Remove small droplets
111
112 GfsAdvectionParams {
113   cfl       = 0.5
114   gradient = gfs_center_gradient
115   flux      = gfs_face_velocity_advection_flux
116   average  = 1
117   scheme    = godunov
118 }
119 GfsApproxProjectionParams {
120   tolerance = 1e-07
121   nrelax    = 7
122   erelax    = 2
123   minlevel  = 0
124   nitermax  = 4000
125   nitermin  = 1
```

```
126   weighted  = 0
127   beta      = 0.5
128 }
129 GfsProjectionParams {
130   tolerance = 1e-07
131   nrelax    = 7
132   erelax    = 2
133   minlevel  = 0
134   nitermax  = 4000
135   nitermin  = 1
136   weighted  = 0
137   beta      = 0.5
138 }
139
140 # Output parameters
141 GfsOutputTime                { step = 0.001 } stdout
142 GfsOutputProjectionStats     { step = 0.001 } stdout
143 GfsOutputSimulation { step = 0.001 } gouttes-bin-%5.3f.gfs { binary = 1 format = gfs }
144 GfsOutputSimulation { step = 0.0001 start = 0.02 end = 0.03 } gouttes-bin-%6.4f.gfs { binary = 1 format
        = gfs }
145 }
146
147 # Boundary conditions
148 GfsBox { id = 1 pid = 0
149 left = Boundary { BcDirichlet U 0 BcDirichlet V 0 }
150 right = GfsBoundaryOutflow
151 top = Boundary { BcDirichlet U 0 BcDirichlet V 0 }
152 bottom = Boundary
153 }
```

Appendix B

Publications and conferences

All publications are freely available for download on my Mendeley profile, and from arXiv or directly from the publisher for Open Access articles.

B.1 Journal publications

- **Thoraval et al. (2013a)** [Open Access]:

Thoraval, M. J., Takehara, K., Etoh, T. G., and Thoroddsen, S. T. (2013). Drop impact entrapment of bubble rings. *Journal of Fluid Mechanics*, **724**: 234–258, arXiv:1211.3076.

One image from this paper has been selected as the cover of the journal volume: Thoraval et al. (2013b): Thoraval, M. J., Takehara, K., Etoh, T. G., and Thoroddsen, S. T. (2013). FLM volume 724 issue 1 Cover and Front matter. *Journal of Fluid Mechanics*, **724**:f1–f4.

- **Thoroddsen et al. (2012e)** [Open Access]:

Thoroddsen, S. T., Thoraval, M.-J., Takehara, K., and Etoh, T. G. (2012). Microbubble morphologies following drop impacts onto a pool surface. *Journal of Fluid Mechanics*, **708**: 469–479.

Images from this paper have been selected as the cover of the journal volume: Thoroddsen et al. (2012d): Thoroddsen, S. T., Thoraval, M.-J., Takehara, K., and

Etoh, T. G. (2012). FLM volume 708 issue 1 Cover and Front matter. *Journal of Fluid Mechanics*, **708**:f1–f2.

- **Thoraval et al. (2012b)** [Open Access]:

Thoraval, M.-J., Takehara, K., Etoh, T. G., Popinet, S., Ray, P., Josserand, C., Zaleski, S., and Thoroddsen, S. T. (2012). von Kármán Vortex Street within an Impacting Drop. *Physical Review Letters*, **108** (26): 264506, arXiv:1202.6569. This paper has been selected as the Physics Focus of the journal issue: Ball (2012): Ball, P. (2012). Focus: Unexpected Turbulence in a Splash. *Physics*, **5**:72.

- **Thoroddsen et al. (2011)**:

Thoroddsen, S. T., Thoraval, M.-J., Takehara, K., and Etoh, T. G. (2011). Droplet Splashing by a Slingshot Mechanism. *Physical Review Letters*, **106** (3): 034501.

B.2 Conferences and other meetings

B.2.1 Conference abstracts and presentations

- **Thoraval et al. (2012a)**:

Thoraval, M.-J., Takehara, K., Etoh, T. G., Popinet, S., Ray, P., Josserand, C., Zaleski, S., and Thoroddsen, S. T. (2012). Drop impact: From bumping to irregular splashing. In *9th European Fluid Mechanics Conference (EFMC9)*, talk 0431, Rome, Italy. Euromech.

- **Thoroddsen et al. (2012f)**:

Thoroddsen, S. T., Thoraval, M.-J., Takehara, K., and Etoh, T. G. (2012). Microbubbles caught under impacting drops. In *9th European Fluid Mechanics Conference (EFMC9)*, talk 0432, Rome, Italy. Euromech.

- **Thoraval et al. (2012d)**:

Thoraval, M.-J., Thoroddsen, S. T., Takehara, K., and Etoh, T. G. (2012). Toroidal

bubble entrapment under an impacting drop. In *65th Annual Meeting of the APS Division of Fluid Dynamics*, **57** (17): talk G4.00002, San Diego, California, USA. APS.

- **Thoroddsen et al. (2012a)**:

Thoroddsen, S., Thoraval, M.-J., Takehara, K., and Etoh, T. G. (2012). The breakup of thin air films caught under impacting drops. In *65th Annual Meeting of the APS Division of Fluid Dynamics*, **57** (17): talk G4.00001, San Diego, California, USA. APS.

- **Thoraval et al. (2011)**:

Thoraval, M.-J., Thoroddsen, S. T., Takehara, K., Etoh, T. G., Ray, P., Josserand, C., and Zaleski, S. (2011). Drop interaction with the ejecta sheet. In *64th Annual Meeting of the APS Division of Fluid Dynamics*, **56** (18): talk S5.00008, Baltimore, Maryland, USA. APS.

- **Thoraval and Thoroddsen (2010)**:

Thoraval, M.-J. and Thoroddsen, S. T. (2010). Dynamics of the ejecta sheets generated by a drop impact. In *63rd Annual Meeting of the APS Division of Fluid Dynamics*, **55** (16): talk HR.00009, Long Beach, California, USA. APS.

B.2.2 Posters and videos

- **Thoraval et al. (2012c)**:

Thoraval, M.-J., Thoroddsen, S. T., Takehara, K., and Etoh, T. G. (2012). Bubble Rings Entrapment. In *Video submission to the Gallery of Fluid Motion APS DFD 2012*, arXiv:1210.3836.

- **Thoroddsen et al. (2012c)**:

Thoroddsen, S. T., Thoraval, M.-J., Takehara, K., and Etoh, T. G. (2012). Bubble

Chandeliers. In *Video submission to the Gallery of Fluid Motion APS DFD 2012*, arXiv:1210.3837.

- **Thoraval et al. (2011)**:

Thoraval, M.-J., Thoroddsen, S. T., Takehara, K., Etoh, T. G., Popinet, S., Ray, P., Josserand, C., and Zaleski, S. (2011). Drop bumping of the ejecta sheet. In *Poster submission to the Gallery of Fluid Motion APS DFD 2011*.

- **Thoraval and Thoroddsen (2011)**:

Thoraval, M.-J. and Thoroddsen, S. T. (2011). Ejecta sheet dynamics. In *KAUST Graduate Research Symposium*, poster. KAUST, Thuwal, Saudi Arabia.

B.2.3 Workshops

- **Noor for Research (2013)**:

Thoraval, M.-J. and Thoroddsen, S. T. (2013). von Kármán Vortex Street within an Impacting Drop. KAUST, Thuwal, Saudi Arabia.

- **KAUST days in OCCAM (2012)**.

OCCAM, University of Oxford, UK.

- **KAUST Event in OCCAM (2011)**:

Thoraval, M.-J. and Thoroddsen, S. T. (2011). High speed imaging of a drop impacting on a deep pool: ejecta sheet dynamics. OCCAM, University of Oxford, UK.

- **Gerris users' meeting (2011)**:

Thoraval, M.-J. and Thoroddsen, S. T. (2011). Axisymmetric drop impact on a deep pool. Université Pierre et Marie Curie, Paris, France.

B.2.4 Popular article

- **Fontez (2012)**:

Fontez, M., with the contribution of Thoraval, M.-J. and Thoroddsen, S. T. (2012). Caméras ultra-rapides: La violence du monde prise sur le vif. *Science & Vie*, **1143**: 82-91.